



HAL
open science

Mechanical analysis and life prediction of unidirectional composites

Elias Dib

► **To cite this version:**

Elias Dib. Mechanical analysis and life prediction of unidirectional composites. Materials. Université Paris-Est, 2016. English. NNT : 2016PESC1107 . tel-01562964

HAL Id: tel-01562964

<https://pastel.hal.science/tel-01562964>

Submitted on 17 Jul 2017

HAL is a multi-disciplinary open access archive for the deposit and dissemination of scientific research documents, whether they are published or not. The documents may come from teaching and research institutions in France or abroad, or from public or private research centers.

L'archive ouverte pluridisciplinaire **HAL**, est destinée au dépôt et à la diffusion de documents scientifiques de niveau recherche, publiés ou non, émanant des établissements d'enseignement et de recherche français ou étrangers, des laboratoires publics ou privés.



UNIVERSITÉ
— PARIS-EST



Thèse présentée pour l'obtention du grade de
Docteur de l'Université Paris-Est

Spécialité: Structures et Matériaux

**Analyse numérique du comportement mécanique en
temps long des composites unidirectionnels**

*Numerical analysis and long-term mechanical behavior of unidirectional
composites*

Elias Dib

Thèse soutenue à l'École des Ponts ParisTech le 09 décembre 2016 devant:

Rapporteurs: Alaa Chateaufneuf
Jacques Lamon

Examineurs: Fouad Kaddah
Karam Sab

Directeurs de thèse: Jean-François Caron
Wassim Raphael

Co-encadrant de thèse: Ioannis Stefanou

Remerciement

Je souhaite remercier tout d'abord tous les membres du jury et en particulier les rapporteurs Jacques Lamon et Alaa Chateaufort pour l'honneur qu'ils m'ont fait de lire et juger cette thèse. Vos remarques ont été précieuses et constructives.

Je tiens à remercier mon directeur de thèse, Jean-François Caron, Professeur de l'École des Ponts ParisTech qui m'a dirigé durant ce travail. Je lui suis reconnaissant pour ses encouragements, son enthousiasme et sa confiance.

Je souhaite adresser également mes remerciements à mon directeur de thèse, Wassim Raphael, professeur de l'École supérieure d'ingénieurs de Beyrouth pour ses conseils et ses aides durant tout ce travail de thèse.

Je voudrais également remercier Ioannis Stefanou, Enseignant – Chercheur de l'École des Ponts ParisTech pour m'avoir encadré, conseillé, surtout dans le domaine de la mécanique des matériaux ainsi que la simulation numérique et la statistique. Son aide m'a été très précieuse.

Un sincère remerciement à Fouad Kaddah Enseignant – Chercheur de l'École supérieure d'ingénieurs de Beyrouth qui m'a consacré beaucoup de son temps et qui m'a guidé, encouragé et soutenu dans mon travail.

Je remercie cordialement Monsieur Raymond Najjar pour avoir financé mon travail de thèse. Je le remercie également pour sa grande disponibilité et son humanisme.

J'adresse mes remerciements à toute l'équipe du Laboratoire Navier : les enseignants - chercheurs, les techniciens et mes collègues doctorants pour tous les échanges techniques, scientifiques et pour leur sympathie, leur accueil chaleureux pendant mon travail de thèse.

Enfin, je remercie toutes les personnes qui m'ont soutenus spécialement mon père, ma mère, mon frère et tous mes amis. Quelles soient remerciée de tout mon cœur.

Résumé

Les matériaux composites jouent un rôle de plus en plus important dans notre société et dans de très nombreux domaines (aéronautique, naval, génie civil...), grâce à leurs avantages en terme de légèreté, d'inaltérabilité et de rigidité. Cependant, ils présentent des faiblesses qui peuvent poser des problèmes au niveau de leur utilisation pour les ouvrages de génie civil. Ces faiblesses concernent notamment leur durabilité. A cause des phénomènes viscoélastiques, les propriétés mécaniques des structures en composites évoluent dans le temps. Le fluage et/ou la relaxation sont des facteurs importants qui peuvent considérablement affecter l'application des composites aux structures. Dans ce travail de doctorat, on effectue une analyse sur le comportement à court et à long terme des composites unidirectionnels renforcés par des fibres de verre/carbone. Afin d'obtenir des résultats quantitatifs sur le comportement mécanique de ces composites, différents types des sollicitations mécaniques seront considérés (ex. compression, cisaillement, tension, flexion). Les analyses sont basées sur deux modèles micromécaniques développés par l'équipe MSA. Le premier modèle est de type shear-lag viscoélastique et le deuxième utilise le logiciel éléments finis Abaqus. Ces deux modèles prennent en compte les différents micro-mécanismes de rupture comme la rupture des fibres, la décohésion des fibres/matrice et le fluage de la résine. Plusieurs analyses numériques sont faites afin de valider les différentes hypothèses de la théorie shear-lag. A partir des analyses menées, des améliorations sont apportées sur le modèle type shear-lag. Une étude comparative avec les éléments finis a permis de bien valider les résultats obtenus par la méthode shear-lag. Ayant calibré nos modèles type shear-lag et éléments finis, des simulations types court et long terme sont faites sur des composites unidirectionnels renforcées par des fibres de verre et de carbone. Les analyses sont réalisées sur plusieurs échantillons pour chaque type de fibre (Simulations de MonteCarlo). Les calculs ont montré un fluage accéléré pour les composites renforcés par des fibres de verres par rapport aux composites renforcés par des fibres de carbone.

Mots-Clés : Composites, Durabilité, Shear-lag, Éléments finis, Fluage, MonteCarlo

Summary

Fiber Reinforced Plastic materials (FRP) find more and more applications in civil engineering. Besides the use of FRPs for the reinforcement of existing structures, these materials are also used quite often today for the construction of bridges and new buildings made partially or entirely of FRPs. Due to their light weight FRPs have a considerable advantage compared to conventional materials such as steel or concrete. Another advantage is that they have outstanding fatigue and durability potential and that they are in general very tolerant to environmental effects such as UV radiations, moisture, chemical attack and extreme temperature variations. However, the lack of a comprehensive, validated, and easily accessible database for the durability of fiber-reinforced polymer composites as related to civil infrastructure applications is a critical barrier to their efficient usage as main load bearing systems. The creep behavior of these materials and their failure under sustained loads remains an open research topic. This study gives a detailed analysis on the mechanical behavior of unidirectional fiber reinforced composites (UD FRP) subjected to different loading patterns (compression, shear, tension and bending). We develop two micromechanical models that allow to analyze the instantaneous and the long-term response of UD composites subjected to different load patterns. The first model is based on the shear-lag theory and the Beyerlein et al.[1998] developments while the second one is established using the Finite Element software Abaqus. A Comparative study between the two models allowed to validate the fundamental assumptions of the shear-lag theory (first model) as well as several numerical issues related to time integration and spatial discretization. The MonteCarlo method is used in order to account for the stochastic fiber strength and its impact on the ultimate tensile strength (short term) and creep (long-term). A parametric investigation on the effect of fiber type and load level/type on the short/long-term behavior of UD composites is also presented. The calculations performed showed an accelerating creep effect for fibers of inferior quality such as glass fibers compared to carbon fibers.

Keywords: Composites, Durability, Shear lag, Finite Element, Creep, MonteCarlo

Content

Motivation	1
Chapter 1: Introduction to composite materials	5
1.1 Introduction	8
1.2 Definition of composite materials	9
1.3 Durability of composites.....	11
1.3.1 Moisture	12
1.3.2 Temperature	12
1.3.3 Fatigue.....	13
1.3.4 Ultraviolet	13
1.3.5 Alkali solutions	13
1.3.6 Fire.....	14
1.4 Creep of composites	14
1.5 Conclusion.....	29
Chapter 2: Modeling of short- and long-term behavior of FRPs under tension loads.	
Shear-lag vs. Finite Element models	30
2.1 Introduction	33
2.2 Theoretical basis of the shear-lag model	35
2.2.1 Equilibrium equations.....	36
2.2.2 Superposition technique and the auxiliary problem of an isolated fiber break.	39
2.2.3 Multiple fiber breaks simulation.....	49
2.2.4 Computer simulations	58
2.2.5 Parameters of interest	63
2.2.6 Parametric analysis and validation	64
2.3 Finite Element Analysis	69
2.4 Comparison of shear-lag and Finite Element modeling results	71

2.4.1 Ultimate tensile strength	71
2.4.2 Creep tests.....	81
2.5 Conclusion.....	83
Chapter 3: Statistical variability of fibers strength and its influence on creep rupture of FRPs under tension loads	85
3.1 Introduction	88
3.2 Short/Long term behavior of GFRPs/CFRPs	88
3.2.1 Simulation procedure	89
3.2.2 Ultimate tensile strength	90
3.2.3 Creep tests.....	92
3.3 Conclusion.....	101
Chapter 4: Creep rupture of FRPs to bending and shear loads.....	102
4.1 Introduction	105
4.2 Response of FRPs to bending loads	113
4.3 Combined shear and tension	116
4.4 Conclusion.....	120
Conclusion	121
Appendix A.....	124

List of Figures

Figure 1.1: Construction of a pedestrian bridge NørreAaby, Denmark 2007 extracted from FRP structures scientific and technical report 2014

Figure 1.2: Construction of Ephemeral cathedral. Peloux et al. [2015]

Figure 1.3: Classification of composites according to fibers topology

Figure 1.4: Different stages of creep

Figure 1.5: Maxwell model

Figure 1.6: Voigt model

Figure 1.7: Creep and creep recovery response of the Voigt model. Osswald n.d. [2010]

Figure 1.8: Boltzmann superposition principle. Osswald n.d. [2010]

Figure 1.9: Relaxation modulus curves for polyisobutylene and corresponding master curve at 25 °C, extracted from Osswald n.d. [2010]

Figure 1.10: Shift factor as a function of temperature used to generate the master curve plotted in Figure 1.9, extracted from Osswald n.d. [2010]

Figure 1.11: Tensile failure surfaces of E-glass/polyurethane composite. Abdel-Magid et al. [2003]

Figure 1.12: Smooth surface of fiber glass in the E-glass/polyurethane composite. Abdel-Magid et al. [2003]

Figure 1.13: Tensile failure surfaces of E-glass/epoxy composite. Abdel-Magid et al. [2003]

Figure 1.14: Surface of fiberglass in the E-glass/epoxy composite. Abdel-Magid et al. [2003]

Figure 1.15: Static rupture modes for GFRPs in traction and bending. Kotelnikova-Weiler [2012]

Figure 1.16: Creep rupture under bending load for GFRPs. Kotelnikova-Weiler [2012]

Figure 1.17: Static rupture modes for a) compression, b) combined torsion-compression, c) combined torsion-traction. Kotelnikova-Weiler [2012]

Figure 1.18: Creep rupture when combining traction with torsion. Kotelnikova-Weiler [2012]

Figure 1.19: Volume fracture for SiC fibers. Lamon et al. [1997]

Figure 1.20: Surface fracture for SiC fibers. Lamon et al. [1997]

Figure 1.21: Evolution of the deformation with time for different temperatures for GFRPs. Kouadri-boudjelthia et al. [2009]

Figure 2.1: Shear-lag model discretization

Figure 2.2: General problem P1 as a superposition of SP1 and SP2

Figure 2.3: Subproblem SP1

Figure 2.4: Superposition technique adopted in order to solve the problem P1'

Figure 2.5: Superposition technique adopted in order to solve the problem SP1'

Figure 2.6: Auxiliary problem A2

Figure 2.6a: Fiber/matrix debonding

Figure 2.7: Fibers strengths for a given specimen composed by 19 fibers

Figure 2.7a: Calculation algorithm (shear-lag method)

Figure 2.8: Periodicity effect

Figure 2.9: Normalized axial stress in the neighboring intact fibers due to the fiber breakage of fiber $n=0$. The first 8 (4+4) neighboring fibers take almost the total load (88%) of the broken fiber.

Figure 2.10: Normalized fiber axial stress (a): without periodic boundary conditions; (b): with periodic boundary conditions

Figure 2.11: Time discretization effect. Average apparent modulus versus normalized time

Figure 2.12: Effect of the spatial discretization Δx . Apparent modulus versus normalized time

Figure 2.13: Effect of fibers number. Apparent modulus versus normalized time

Figure 2.14: Length effect. Average apparent modulus versus normalized time

Figure 2.15: Finite Element model description

Figure 2.16: Calculation algorithm in the Finite Element model

Figure 2.17: Position of the imposed defect/fiber break

Figure 2.18: Normalized fiber axial stress map

Figure 2.19: Normalized fiber axial stress diagram

Figure 2.20: Normalized matrix shear stress around break site

Figure 2.21: Comparison between Finite Element and shear-lag models for the applied fiber stress versus strain curve

Figure 2.22: Comparison between Finite Element and shear-lag models for the evolution of the number of fiber breaks with the applied fiber stress

Figure 2.23: Comparison between Finite Element and shear-lag models for the fiber breaks sites at $P=1900$ MPa

Figure 2.24a: Normalized fiber axial stress for $P=2050$ MPa

Figure 2.24b: Fiber breaks sites and matrix debonded region for $P=2050$ MPa

Figure 2.25: Fiber stress versus strain curve (fiber/matrix debonding taken into account)

Figure 2.26: Fiber stress versus strain curve (fiber/matrix debonding neglected)

Figure 2.27: Normalized fiber stress state at $P=3500$ MPa (fiber/matrix debonding neglected)

Figure 2.28: Matrix shear stress state at $P=3500$ MPa (fiber/matrix debonding neglected)

Figure 2.29: Evolution of the number of matrix debonded elements with the applied fiber stress

Figure 2.30: Comparison between Finite Element and shear-lag models for the evolution of the apparent modulus with time

Figure 2.31: Comparison between Finite Element and shear-lag models for the evolution of the deformation with time

Figure 2.32: Comparison between Finite Element and shear-lag models for the evolution of the number of fiber breaks with time

Figure 2.33: Comparison between Finite Element and shear-lag models for the fiber break sites at the fourth time step

Figure 3.1: Probability density functions for the three types of fibers

Figure 3.2: Fibers strengths for a given specimen composed by 19 fibers

Figure 3.3: Average stress/strain curve: Finite Element method (P122 glass fibers)

Figure 3.4: Average stress/strain curve: Finite Element method (PU glass fibers)

Figure 3.5: Average stress/strain curve: Finite Element method (T300 carbon fibers)

Figure 3.6: Average apparent modulus versus time for $P=0.7xPu$ and $P=0.8xPu$ for P122 glass fibers

Figure 3.7: Average deformation versus time for $P=0.7xPu$ and $P=0.8xPu$ for P122 glass fibers

Figure 3.8: Evolution of the number of fiber breaks versus time for $P=0.7xPu$ and $P=0.8xPu$ for P122 glass fibers

Figure 3.9: Normalized fibers axial stress after 50 years for P122 glass fibers at $P=0.8xPu$

Figure 3.10: Average apparent modulus versus time for $P=0.7xPu$ and $P=0.8xPu$ for PU glass fibers

Figure 3.11: Average deformation versus time for $P=0.7xPu$ and $P=0.8xPu$ for PU glass fibers

Figure 3.12: Evolution of the number of fiber breaks versus time for $P=0.7xPu$ and $P=0.8xPu$ for PU glass fibers

Figure 3.13: Normalized axial stress after 50 years for PU glass fibers at $P=0.8xPu$

Figure 3.14: Average apparent modulus versus time for $P=0.7xPu$ and $P=0.8xPu$ for T300 carbon fibers

Figure 3.15: Average deformation versus time for $P=0.7xPu$ and $P=0.8xPu$ for T300 carbon fibers

Figure 3.16: Evolution of the number of fiber breaks versus time for $P=0.7xPu$ and $P=0.8xPu$ for T300 carbon fibers

Figure 3.17: Normalized axial stress after 50 years for T300 carbon fibers at $P=0.8xPu$

Figure 3.18: Evolution with time of the average position of rupture sites (P122/PU glass fibers)

Figure 3.19: Fitting of the deformation evolution given by shear-lag model with the Findley law for P122 glass fibers

Figure 4.1: Micro buckling failure mode

Figure 4.2: Kinking failure mode

Figure 4.3: Comparison of different models for compressive strength estimation for E-glass fibers. Naik and Kumar [1999]

Figure 4.4: Comparison of different models for compressive strength estimation for T300 carbon fibers. Naik and Kumar [1999]

Figure 4.5: Theoretical basis of the model for bending analysis

Figure 4.6: Fibers tensile strengths for a given specimen composed of 19 fibers

Figure 4.7: Number of fiber breaks versus maximum applied fiber stress for P122 glass fibers

Figure 4.8: Number of fiber breaks versus maximum applied fiber stress for T300 carbon fibers

Figure 4.9: Combining tension and shear

Figure 4.10: Stress/Strain curve for combined tension and 20% of shear stress (P122 glass fibers)

Figure 4.11: Stress/Strain curve for combined tension and 50% of shear stress (P122 glass fibers)

Figure 4.12: Stress/Strain curve for combined tension and 70% of shear stress (P122 glass fibers)

Figure 4.13: Deformation evolution with time, with and without shear stress

Figure 4.14: Apparent modulus evolution with time, with and without shear stress

Figure A.1: Model discretization for compression analysis (shear-lag method)

Figure A.2: Superposition principle

Figure A.3: Auxiliary problem A1 of a central fiber break under tension load

Figure A.4: Normalized compressive fiber axial stress calculated with the shear-lag model

Figure A.5: Normalized fibers compressive axial stress in the first intact fiber. Beyerlein et al.[2001]

List of Tables

Table 1.1: Different types of composite materials

Table 1.2: Mechanical properties of fiber materials

Table 1.3: Mechanical properties of matrix materials

Table 2.1: Average values and standard deviation values for the apparent modulus at the final time step

Table 2.2: Simulation parameters for P122 glass fibers. Zinck [2011]

Table 2.3: Comparison between overstress factors shear-lag vs. Finite Element

Table 2.4: Overstress factors with fiber/matrix debonding shear-lag vs. Finite Element

Table 3.1: Simulation parameters for T300 carbon fibers and PU glass fibers. Zinck [2011]/ Baxevanakis et al. [1998]

Table 3.2: Ultimate tensile strength for the three fiber types

Table 3.3: Stress limits of FRPs according to ACI code

Table 4.1: Compressive strength for UD composites reinforced with E-glass fibers. Naik and Kumar [1999]

Table 4.2: Compressive strength for UD composites reinforced with T300 carbon fibers. Naik and Kumar [1999]

Table A.1: Overstress factors (in compression) shear-lag vs. Finite Element

Motivation

Context:

Over the last forty years, composite materials, plastics, and ceramics have been the dominant emerging materials. The volume and number of applications of composite materials has grown steadily, penetrating and conquering new markets relentlessly. Fiberglass boats and graphite sporting goods are typical examples.

A composite material is fabricated by the combination of two or more distinct materials to form a new material with enhanced properties. For example, rocks granulates are combined with cement to make concrete. The most common composites are those made with strong fibers held together in a binder. The role of binder or matrix is to transfer the load between fibers (mostly in shear). The matrix also protects the fibers from environmental effects such as moisture, leading to corrosion resistance for instance.

Although having major advantages, composites are frequently used in civil engineering as secondary load bearing elements. This may be owed to many economical and technical reasons, but also to the lack of a comprehensive, validated, and easily accessible database for their durability and in particular for their creep behavior. Experimental results show that some of the empirical equations for creep estimation describe quite well secondary creep. However the transition from secondary to tertiary creep (rupture) is less understood, though critical for applications. Therefore studying the long term behavior of composites under various conditions remains an open, challenging topic, with important impact on their use in civil engineering.

Research goals/Originality

The importance of understanding the mechanical behavior of composites led us to develop and enhance two micromechanical models that allow assessing the short- and long-term response of unidirectional composites under any given load. The first model is based on the shear-lag theory (Cox [1952], Beyerlein et al.[1998]) taking into account the recent developments of Kotelnikova-Weiler[2012] that considered fiber/matrix debonding in the calculations, while the second one is established using the Finite Element software Abaqus. The aim of this research work was to enhance and validate the existing shear-lag numerical tool (Kotelnikova-Weiler[2012]) that simulates only tension loads and to develop a second numerical tool (based on Finite Element) that can model

different load patterns (such as compression, tension, bending and shear). The enhancements of the existing shear-lag model relies in the introduction of proper boundary conditions (such as periodic boundary conditions) that were neglected in the previous shear-lag models and in the verification of the main calculation assumptions such as the time step, the mesh size, the number of fibers taken into account and the length of the specimen. We note that the approach of analyzing the response (short- and long-term) of composites to tension loads obtained from the shear-lag model is different from what was presented in previous research works (Beyerlein et al.[1998]). At the matter of fact, each result obtained from the shear-lag equations (fiber stress, fiber deformation, fiber break site, fiber/matrix debonded region, number of fiber breaks, etc...) is analyzed and compared to the one obtained from the Finite Element model in order to verify its validity. Due to the stochastic behavior of the reinforcing fibers, we perform MonteCarlo simulations by considering several generated specimens in the calculations. It is to be noted that one generated specimen is not sufficient to represent the actual behavior of the composite. It is worth emphasizing that the capacity of the Finite Element model to simulate progressive fiber breakage and fiber/matrix debonding is also an important originality of the current research work since in most studies the fiber break sites and the fiber/matrix debonded regions were priory imposed (Nedele and Wisnom [1994], Blassiau et al. [2007]). The calibrated models (shear-lag and Finite Element) are also used to perform short- and long-term simulations on composites reinforced with different types of fibers (such as glass and carbon) and subjected to different loading patterns (such as compression, tension, bending and shear).

Outline of the thesis

The material covered in this current research is divided into four chapters. Its content is organized as follows:

- Chapter 1 presents a literature review on the durability of composite materials showing the influence of moisture/alkali solutions, thermal condition, creep and relaxation, fatigue, ultraviolet and fire on the life span of any structure build with composites. The creep of composites is thoroughly described in this chapter showing its different stages (primary, secondary and tertiary) and the factors that accelerate it. A literature review of the existing creep models is also presented.

The main role of this chapter is to highlight all the factors that triggered this research regarding the durability of composites and especially their creep behavior.

- Chapter 2 presents the shear-lag equations and the existing numerical tool which are used for the analysis of the behavior of unidirectional composites under tension loads (Beyerlein et al. [1998], Kotelnikova-Weiler[2012]). The parametric analysis that was performed herein on the shear-lag model is detailed along with the different enhancements. Furthermore, the results obtained from the enhanced shear-lag model were validated through a comparative study with the Finite Element method.
- Chapter 3 exposes the effect of the strength and statistical variability of fibers on the creep behavior of composites subjected to sustained tension loads. Different kinds of fibers, i.e. glass and carbon, were considered in the analysis and their influence on the long-term behavior of the composite and its ultimate tensile strength was explored. MonteCarlo simulations were performed using the shear-lag and the Finite Element models. The simulations showed accelerating creep effect for fibers of inferior quality, such as glass fibers compared to higher quality fibers such as carbon fibers
- Chapter 4 describes the behavior of composites under compression, bending and shearing. A literature review of the existing models used to assess the compressive strength of a unidirectional composite is presented, because unlike tension, there is no clear criterion for the fibers resistance in compression. Moreover, simulations for composites subjected to bending and shear loading are presented for different types of fibers (glass and carbon). The simulations showed accelerating creep effect under combined shear and tension loads.
- Appendix A presents a comparative study between the results obtained from the developed (shear-lag and Finite Element) numerical models and the Beyerlein et al.[2001] work on the compression behavior of unidirectional composites.

Chapter 1: Introduction to composite materials

This chapter presents an overview on FRP materials highlighting the advantages that encourage their use in many domains and especially in civil engineering. It also emphasizes that the durability of these materials remains a barrier to their efficient usage as main load bearing elements in civil engineering. A description on the influence of several environmental factors on the durability of composites is briefly presented. The creep of these materials under sustained load is thoroughly described showing its different stages and its influence on the life span of any structure constructed using FRPs. The main empirical formulas that exist in the literature for creep evolution are also presented.

Content

1.1 Introduction	8
1.2 Definition of composite materials	9
1.3 Durability of composites.....	11
1.3.1 Moisture	12
1.3.2 Temperature	12
1.3.3 Fatigue.....	13
1.3.4 Ultraviolet	13
1.3.5 Alkali solutions	13
1.3.6 Fire.....	14
1.4 Creep of composites	14
1.5 Conclusion.....	29

1.1 Introduction

Fiber Reinforced Plastic materials (FRP) are beginning to find more and more applications in the civil engineering domain. Besides the use of FRPs for the reinforcement of existing structures, these materials are utilized quite often today for the construction of bridges and even for new buildings made entirely of composites. For instance, a 23 m long pedestrian and cycle bridge was constructed in NørreAaby, Denmark in 2007 with 100% GFRPs (Glass Fibre Reinforced Polymers or Plastics) profiles (see Figure 1.1). The Ephemeral cathedral of Creteil in France (see Figure 1.2) was built in 2013 with a GFRP gridshell structure (Peloux et al. [2015]). Another application of FRPs in civil engineering, among others, is the construction of a 41.4 m long pedestrian bridge in a Train station at Kosino, Chertanovo in Moscow in 2004. It consists of three spans - two of 15.0 m and one of 13 m length prefabricated and assembled on site. The bridge was installed in just 49 minutes.



Figure 1.1: Construction of a pedestrian bridge NørreAaby, Denmark 2007 extracted from FRP structures scientific and technical report 2014

Composites offer several advantages compared to conventional materials (such as light weight and acceptable stiffness), however their creep behavior is still not well understood. This is clearly reflected in the civil engineering design codes (ACI, Eurocomp) that impose high safety factors on structures built with composite in order to avoid creep rupture. The durability of these materials is therefore a main drawback for their use in the civil engineering domain.



Figure 1.2: Construction of Ephemeral cathedral. Peloux et al. [2015]

The aim of this chapter is to present a brief description on composite materials highlighting the factors that influence their durability and in particular their creep behavior. A summary on the models that exists in the literature allowing the estimation of the creep of composites is also presented. In the following chapters, the shear-lag and the Finite Element techniques used for creep predictions of composite materials will be thoroughly discussed.

1.2 Definition of composite materials

A composite material is defined as a combination of two or more materials, in general a matrix combined with reinforcement. Combining these materials gives properties superior to the properties of the individual components. In the case of a composite, the reinforcement is the fibers and is used to fortify the matrix in terms of strength and stiffness. Typical reinforcing fibers are glass, carbon and aramid. The fibers diameter usually ranges from 5 to 15 μm . The structural role of the matrix is to connect the load bearing elements (the fibers) via shear forces. The matrix also protects the fibers from abrasion and from environmental factors causing its degradation. Composites are conventionally divided into groups according to the material used for the matrix element (see to Table 1.1). In this work we are interested in analyzing the behavior of glass/carbon fiber reinforced polymers (GFRPs/CFRPs). The mechanical proprieties of some of the fiber/matrix elements are presented in Tables 1.2 and 1.3.

Composite type	Fiber	Matrix
Polymer matrix composites (PMCs)	E-glass	Epoxy
	S-glass	Polyimide
	Carbon (graphite)	Polyester
	Aramid (Kevlar)	Thermoplastics
	Boron	PEEK, polysulfone, etc.
Metal matrix composites (MMCs)	Boron	Aluminum
	Borsic	Magnesium
	Carbon (graphite)	Titanium
	Silicon carbide	Cooper
Ceramic matrix composites (CMCs)	Silicon carbide	Silicon carbide
	Alumina	Alumina
	Silicon nitride	Glass ceramic
Carbon matrix composites (CCCs)	Carbon	Carbon

Table 1.1: Different types of composite materials

Fiber type	Diameter [μm]	Density [kg/m^3]	Young's modulus [MPa]	Poisson's ratio
E-Glass	16	2600	74000	0.25
S-Glass	10	2500	86000	0.2
Carbon T300	7	1750	230000	0.2
Kevlar 49	12	1450	130000	0.4
Boron	100	2600	400000	0.2

Table 1.2: Mechanical properties of fiber materials

Matrix type	Density [kg/m ³]	Young's modulus [MPa]	Poisson's ratio
Epoxy	1200	4500	0.4
Polyimide	1400	4000-19000	0.35
Polyester	1200	4000	0.4
PEEK	1320	3200	0.4
Polysulfone	1350	3000	

Table 1.3: Mechanical properties of matrix materials

Another classification of the composite materials is based on the fibers length and distribution. Figure 1.3 shows the classification of composites according to fibers topology.

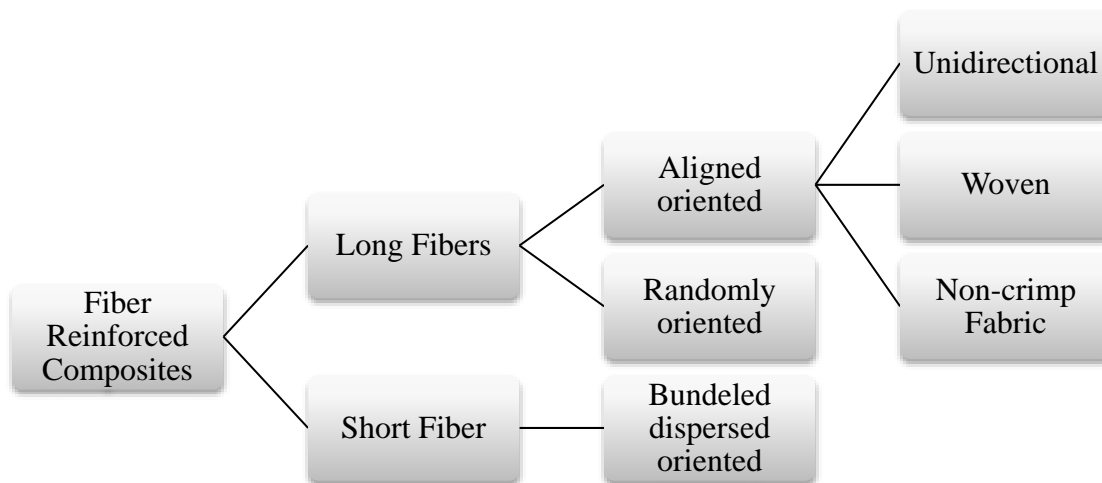


Figure 1.3: Classification of composites according to fibers topology

Although the short-term mechanical properties of these materials are well documented, the long-term mechanical behavior (durability) is less studied. In the following section, the durability of composites will be discussed.

1.3 Durability of composites

The understanding of the long-term behavior of FRPs under sustained load is vitally important in their use for structural applications. In the work of Karbhari et al. [2003] moisture/alkali solutions, thermal condition, creep and relaxation, fatigue, ultraviolet and fire were identified as crucial factors that highly influence the life span of any structure build with FRPs. The

influence of each environmental factor will be briefly discussed below and the creep behavior will be thoroughly detailed in section 1.4.

1.3.1 Moisture

Water molecules can diffuse into the network of composites to affect the mechanical properties of its constituents. The fibers are degraded by moisture and alkali due to etching and leaching actions. However, the degradation of matrices occurs due to hydrolysis, plasticization, and swelling in the presence of water. Furthermore, high moisture content weakens the interface between the fibers and the matrix which decreases the tensile properties of the composite. Shen and Springer [1977] reported that for 90 degree laminates, the ultimate tensile strength and elastic module decreased with increasing moisture content. The decrease may be as high as 50-90 percent. Bradley [1995] studied the degradation of graphite / epoxy composites due to sea water immersion. Through observation by scanning electron microscopy (SEM), they found that the measured 17% decrease in transverse tension strength was associated with the degradation of the interface, which changed the mechanism of fracture from matrix cracking to interfacial failure. The ability to predict the diffusion of water and its influences on the resin properties are necessary to predict long term behavior of composites. The uptake of moisture usually is measured by weight gain and the mechanism of water diffusion is characterized by Fick's law. Based on Fick's law, the study of Shen et al. [1976] presented expressions for the moisture distribution and moisture content as a function of time for one-dimensional composite materials. Many experimental data support the analytical solution determined by Shen et al. [1976] and this expression has been widely accepted to describe the water diffusion behavior in composites.

1.3.2 Temperature

The temperature effect on the mechanical properties of composites derives partly from the internal stresses introduced by the differential thermal coefficients of composite components. Such internal stresses change magnitude with temperature change, in some cases producing matrix cracking at very low temperatures. In practical applications, each polymer has its own operating temperature range. Usually a polymer has a maximum use temperature slightly below its glass transition temperature (T_g), at which the polymer transfers from rigid state to rubbery state and suffers substantial mechanical property loss. Elevated temperatures combined with humid environments have been found to magnify the problem by further reducing T_g , among other factors. The work of Marom [1989] showed that interlaminar fracture energy decreased

25-30% as the temperature increased from 50 to 100°C. The interlaminar fracture surface characteristics of graphite/epoxy were also investigated in the same paper and pronounced differences were observed in the amounts of fiber/matrix separation and resin-matrix fracture with increasing temperature.

1.3.3 Fatigue

Fatigue causes extensive damage throughout the composite, leading to failure from general degradation of the material instead of a predominant single crack. There are three basic failure mechanisms in composite materials as a result of fatigue: matrix cracking, fiber breakage and interfacial debonding. Karbhari et al. [2003] in their study on GFRPs noted a reduction in the Young's modulus of the tested specimens after many cycles of loading and unloading at 45% of their ultimate tensile strength. There are many existing theories that are used to describe fatigue of composite materials. However, fatigue testing of laminates in an experimental test program is probably the best method of determining the fatigue properties of a candidate laminate.

1.3.4 Ultraviolet

The UV components of solar radiation incident on the earth surface are in the 290– 400 nm band. The energy of these UV photons is comparable to the dissociation energies of polymer covalent bonds, which are typically 290–460 kJ/mol. Thus, UV photons absorbed by polymers result in photo-oxidative reactions that alter the chemical structure resulting in material deterioration. In literature (Brook [2002] for instance), there are few investigations that focus on the effects of UV radiation on the degradation of mechanical properties of FRPs. Brook [2002] reported that for relatively short periods of exposure, only changes in surface morphology are observed. However, for extended exposure to UV radiation, matrix properties can suffer severe deterioration, e.g. interlaminar shear strength and flexural strength and flexural stiffness can all decrease. The fiber properties, such as tensile modulus and tensile strength, are usually not affected significantly, especially for carbon fiber-reinforced materials.

1.3.5 Alkali solutions

The effect of alkaline and acid solutions on the FRPs mechanical properties is widely analyzed by many researchers. Even though, the studies that exist in the literature are not sufficient to establish a full knowledge of this subject. Rakin et al.[2011] studied the effect of alkaline and acid solutions on the tensile properties of glass-polyester composites. They concluded that the alkaline solution decreases the tensile properties (ultimate tensile strength and Young's modulus) and this tendency increases with the pH value. According to the study of Kawada et

al. [2001], stress-corrosion cracking in GFRPs occurs as a result of a combination of loads and exposure to a corrosive environment. Sharp cracks initiate and propagate through the material as a direct consequence of the weakening of the glass fibers by the acid. The strength of the fibre reduces dramatically as a result of diffusion of acid and chemical attack which causes a highly planar fracture with a much reduced failure stress.

1.3.6 Fire

Heat causes the polymer to melt which induces degradation of mechanical properties of the composite. Polymer transforms from solid phase to rubbery or semi-liquid phase once the matrix resin temperature goes above the glass transition temperature T_g . T_g is often well below the decomposition temperature of the polymer, which is the temperature at which enough heat energy has entered into the polymer to cause bonds to begin to break and the polymer to fragment. This leads to the loss of the mechanical properties of the composite as the matrix resin vaporizes. One notable example for the influence of heat on composites is the Norwegian minesweeper Orkla, which was an all composite vessel that caught fire and rapidly sank in November 2002.

1.4 Creep of composites

Another crucial factor that highly influences composites durability is creep. By definition, the creep is the ability of a material to deform under sustained load (see Figure 1.4). Its initial stress-strain behavior can be considered as linear elastic. Under sustained loading the material creeps with a steady strain-rate until tertiary creep takes place. Tertiary creep is related to an increase in deformation rate under, again, constant loading, and eventually failure. The behavior of the glass or carbon fibers is brittle and cannot justify rate effects at the observed time scale of transition from secondary to tertiary creep. However, the viscoelastic behavior of the matrix elements can. Many theoretical and empirical relations exist in the literature allowing the calculation of the evolution with time of the deformation of a material under sustained load. We will briefly cite below some of the models that exists in the literature for creep calculations.

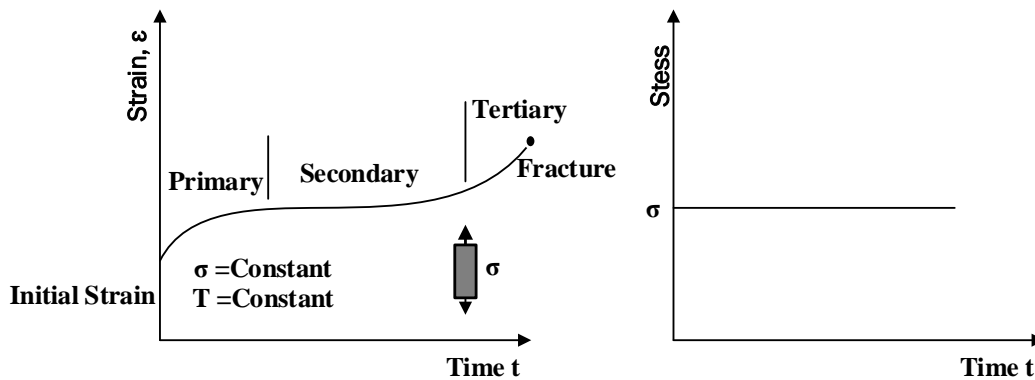


Figure 1.4: Different stages of creep

Creep Models

One of the first models that were used for creep evaluation is the Maxwell model. The Maxwell model can be represented by a spring and a viscous damper connected in series (see Figure 1.5). Maxwell calculated the elastic component of the strain that occurs instantaneously, corresponding to the spring, and relaxes immediately upon release of the stress and allows the estimation of a second component of the strain which is a viscous component that grows with time as long as the stress is applied (viscous damper effect). The model predicts that stress decays exponentially with time, which is accurate for most polymers.

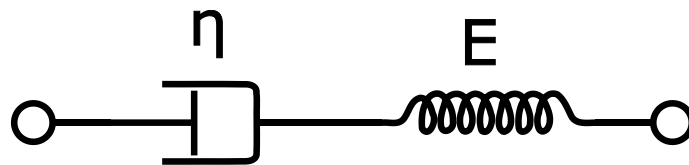


Figure 1.5: Maxwell model

We present briefly the equations of the Maxwell model:

If we consider the Hook's law for the spring:

$$\sigma = E\varepsilon \quad (1.1)$$

where σ is the applied stress, ε is the specimen deformation and E is the elastic stiffness of the spring.

The viscous damper behavior is governed by the Newton viscosity law (equation 1.2)

$$\sigma = \eta \frac{d\varepsilon}{dt} \quad (1.2)$$

where η is the viscosity modulus and t is the time.

Combining equations (1.1) and (1.2) leads to:

$$\frac{d\varepsilon}{dt} = \frac{1}{E} \frac{d\sigma}{dt} + \frac{\sigma}{\eta} \quad (1.3)$$

The Maxwell model for creep or constant-stress conditions postulates that strain rate will increase linearly with time. However, polymers for the most part show a strain rate decreasing with time.

Another model for creep predicting was presented by Voigt. The model of Voigt consists of a spring and a viscous damper connected in parallel (see Figure 1.6). The spring models the elastic response while the dashpot models the viscous/time dependent response to the applied load.

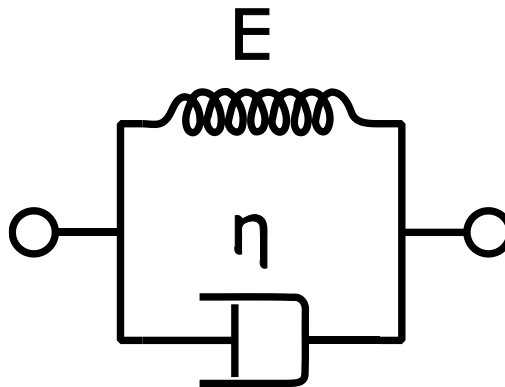


Figure 1.6: Voigt model

The governing equation for the Voigt model is:

$$\sigma = E\varepsilon + \eta \frac{d\varepsilon}{dt} \quad (1.4)$$

where η and E are the viscosity and Young's modulus respectively. Using the above equation, the strain in a creep test (constant stress) in the Voigt model can be solved with:

$$\varepsilon = \frac{\sigma}{E} (1 - \exp^{-t/\tau}) \quad (1.5)$$

$$\tau = \eta/E \quad (1.6)$$

Figure 1.7 shows the creep and recovery curve for the Voigt model.

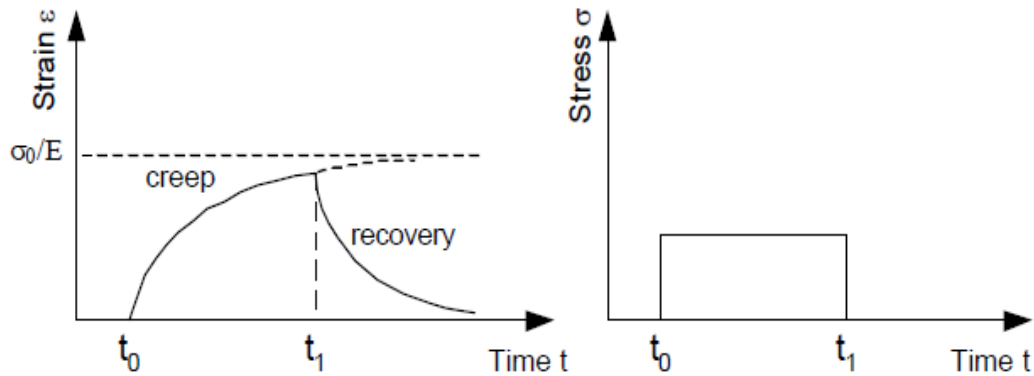


Figure 1.7: Creep and creep recovery response of the Voigt model. Osswald n.d. [2010]

The Voigt model predicts creep more realistically than the Maxwell model. However, the Voigt model is not good at describing the relaxation behavior after the stress/load is removed.

Superposition techniques are also introduced in the literature in order to model creep. The Boltzmann superposition technique is one of the methods. It describes the response of a material to different loading histories. The Boltzmann superposition technique (see Figure 1.8) is based on the hypothesis that the response of the material to a given load is independent of the response of the material to any load which is already applied on the material. Therefore at a given temperature, the deformation of the material is proportional to the applied stress. The total strain may be expressed by equations 1.7 and 1.8.

$$\varepsilon(t) = D(t - \tau_1) + D(t - \tau_2)(\sigma_2 - \sigma_1) + \dots + D(t - \tau_i)(\sigma_i - \sigma_{i-1}) \quad (1.7)$$

Or

$$\varepsilon(t) = \int_0^t D(t - \tau) d\sigma(\tau) \quad (1.8)$$

where

$$D(t) = \frac{1}{E(t)} \quad (1.9)$$

where $D(t)$ is the creep compliance function which is a characteristic of the polymer at a given temperature. Figure 1.8 shows the response of a material to applied stress according to the Boltzmann superposition technique.

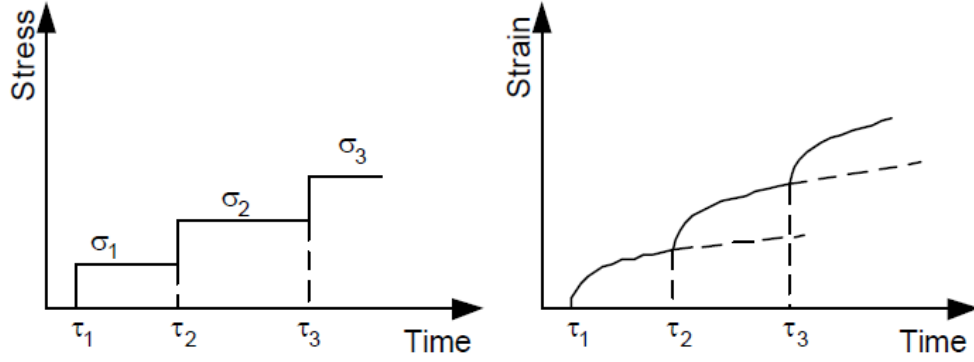


Figure 1.8: Boltzmann superposition principle. Osswald n.d. [2010]

At a given time t_1 , the strain ε_1 induced by an applied stress σ_1 is:

$$\varepsilon_1(t) = \sigma_1 D(t) \quad (1.10)$$

According to linear viscoelasticity, the compliance $D(t)$ is independent of the stress. Therefore if a stress increment $\sigma_2 - \sigma_1$ is applied at a time τ_2 , the strain increase due to the stress increment can be expressed with equation 1.11:

$$\varepsilon_2(t) = D(t - \tau_2)(\sigma_2 - \sigma_1) \quad (1.11)$$

Likewise the strain increase due to $\sigma_3 - \sigma_2$ can be written with equation 1.12:

$$\varepsilon_3(t) = D(t - \tau_3)(\sigma_3 - \sigma_2) \quad (1.12)$$

A generalized form of the Boltzmann superposition technique can be written with equation 1.13:

$$\varepsilon(t) = D_0 \sigma + \int_0^t \Delta D(t - \tau) \frac{d\sigma}{d\tau} d\tau \quad (1.13)$$

In a similar way the relaxation of the material can be determined with equation 1.14:

$$\sigma(t) = E_0 \varepsilon + \int_0^t \Delta E(t - \tau) \frac{d\varepsilon}{d\tau} d\tau \quad (1.14)$$

Another superposition technique which is well used is the time temperature superposition principle (TTSP). It describes the equivalence of time and temperature. The time temperature superposition technique is used in order to obtain the creep behavior of a material at a given temperature using creep curves at different temperature levels which can be shifted along the

time axis. Figure 1.9 shows an example of relaxation modulus curves for time temperature superposition extracted from Osswald.n.d.[2010]. Relaxation curves made at different temperatures are superposed by horizontal shifts along a logarithmic time scale to give a single master curve covering a large range of times.

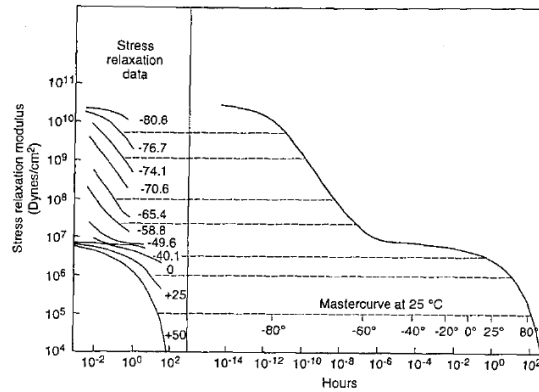


Figure 1.9: Relaxation modulus curves for polyisobutylene and corresponding master curve at 25 °C, extracted from Osswald n.d. [2010]

The amount that each curve was shifted can be plotted with respect to the temperature difference taken from the reference temperature (see Figure 1.10).

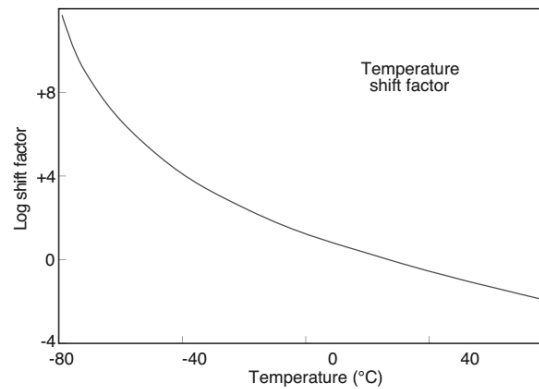


Figure 1.10: Shift factor as a function of temperature used to generate the master curve plotted in Figure 1.9, extracted from Osswald n.d.[2010]

Williams, Landel and Ferry (Ferry [1955]) established the WLF equation that determines the shifting factors a_T .

$$a_T = -\frac{C_1(T - T_{ref})}{C_2 + (T - T_{ref})} \quad (1.15)$$

where C_1 and C_2 are material dependent constants.

It has been shown that for most polymers $C_1 = 17.44$ and $C_2 = 51.6$ if the reference temperature T_{ref} is chosen as glass transition temperature. Often, the WLF equation must be adjusted until it fits the experimental data. Master curves of stress relaxation tests are important because the polymer's behavior can be traced over much longer periods than those that can be determined experimentally.

In summary, the application of the TTSP typically involves the following steps:

- Experimental determination of frequency-dependent curves of isothermal viscoelastic mechanical properties at several temperatures and for a small range of frequencies.
- Computation of a translation factor to correlate these properties for the temperature and frequency range.
- Experimental determination of a master curve showing the effect of frequency for a wide range of frequencies.
- Application of the translation factor to determine temperature-dependent module over the whole range of frequencies in the master curve.

The application of the time temperature superposition principle is proven to be adequate by multiple studies. Alwis and Burgoyne [2006] demonstrated that creep curves for composites reinforced with aramid fibers can be obtained by using the TTSP. The authors discussed the methods to be used in order to obtain smooth master curves and confirmed the validity of the resulting curves and the corresponding stress-rupture lifetime. Miyano et al.[2008] validated in their study the TTSP and they also demonstrated the applicability of their accelerated testing methodology (ATM). The ATM method is based on the time temperature superposition technique. Using this method the authors predicted the long-term fatigue life of polymer matrix composites.

In the studies cited above, among others, the Boltzmann superposition technique as well as of the TTSP are generally used only in the case of linear viscoelasticity. Several models have been developed in order to describe the nonlinear viscoelasticity. In fact, Findley [1956] developed a nonlinear form of a power law in order to predict the creep behavior of laminated clothed reinforced plastics. At a later stage Findley and Peterson [1958] showed that the existing model accurately predicted the creep behavior of four types of plastic materials for 10 years of experimental data. The basic form of the Findley power law is:

$$\varepsilon(t) = \varepsilon_0 + mt^n \tag{1.16}$$

where

$$\varepsilon_0 = \varepsilon_0' \sinh \frac{\sigma}{\sigma_\varepsilon} \quad (1.17)$$

$$m = m' \sinh \frac{\sigma}{\sigma_m} \quad (1.18)$$

ε_0' , σ_ε , m' , σ_m and n are all material dependant parameters which may be functions of temperature, absorbed moisture content, etc..., but are assumed not to be functions of time or the applied stress level. Boller [1965] proposed a simple method for evaluating the power law parameters. A more accurate least square approach was introduced at later stage in order to properly evaluate these parameters. Multiple applications and verifications to the power law proposed by Findley exist in the literature. Dillard et al. [1987] study led to the conclusion that the nonlinear procedure proposed by Findley could be used to accurately fit the experimental data of creep test for T300/934 graphite/epoxy composites. Furthermore, Yen et al.[1990] validated the Findley power law expression in his study on chopped fiber composites. Bank and Mosallam [1992] analyzed the short and the long term behavior of a frame structure build with pultruded beams and columns. Creep test were performed at sustained flexural load. The authors reported good agreement between the experimental data and the results obtained using the Findley law.

Schapery's [1969] also contributed in the development of models for nonlinear viscoelasticity. Schapery's [1969] model is based on irreversible thermodynamics. For uniaxiale loading under isothermal conditions, this approach takes the form:

$$\varepsilon(t) = g_0 D_0 \sigma + g_1 \int_0^t \Delta D(\psi - \psi') \frac{dg_2 \sigma}{d\tau} d\tau \quad (1.19)$$

where D_0 and $\Delta D(\psi)$ are the initial and the transient component of the linear viscoelastic creep compliance, respectively.

$$\psi = \psi(t) = \int_0^t \frac{dt'}{a_\sigma} \quad (1.20)$$

$$\psi' = \psi'(\tau) = \int_0^\tau \frac{dt'}{a_\sigma} \quad (1.21)$$

The parameter g_0 is related to the nonlinear instantaneous compliance, g_1 is associated with the nonlinear transient compliance, and g_2 is related to the loading rate effect on nonlinear response. The parameter a_σ is the horizontal shift factor for stress and it is used in the same manner as the temperature shift factor a_T . Lou and Schapery [1971] extended the Schapery's [1969] integral model to characterize the nonlinear time-dependent behavior of glass fiber reinforced epoxy. The Schapery single integral approach has been shown to be accurate and adaptable by many studies (Dillard et al. [1987], among others).

Experimental work was also performed in the aim of understanding the failure mechanism of composites subjected to sustained loads. For instance, Abdel-Magid et al. [2003] investigated the creep rupture of two systems of E-glass reinforced polymer composites (E-glass/polyurethane and E-glass/epoxy) subjected to sustained bending load. The two composite systems showed similar short-term mechanical behaviors, however their long term creep behaviors were quite different. The E-glass/polyurethane system exhibited tertiary creep leading to rupture within a few hours when subjected to about 60% of its flexural strength while the E-glass/epoxy endured months of loading at 60% of its flexural strength before rupture. Scanning electron microscopy (SEM) was used to study the failure surface of the specimens. Figure 1.11 shows SEM photomicrograph of the tensile failure surface of E-glass/polyurethane composites. The fibers in Figure 1.11 are shown pulled out of the resin before failure. The fibers on the tension failure surface of this material seem clean and smooth with no traces of resin on their surface.

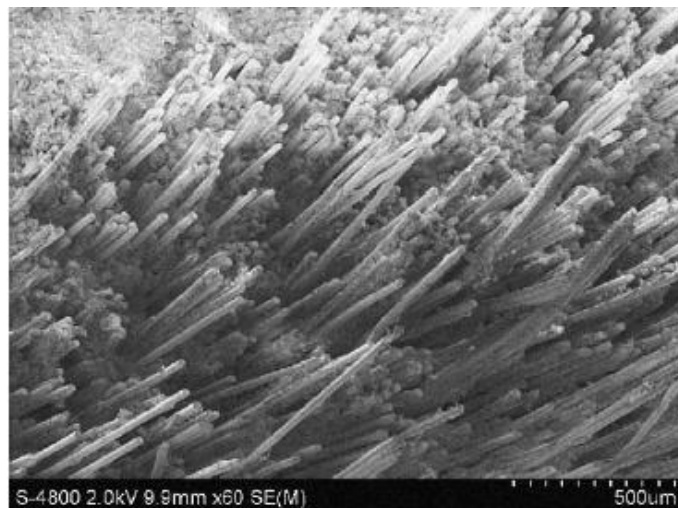


Figure 1.11: Tensile failure surfaces of E-glass/polyurethane composite. Abdel-Magid et al. [2003]

A closer look on the fiber surface (see Figure 1.12) reveals the absence of matrix around the fiber. This indicates poor interfacial bonding between the polyurethane and the E-glass fibers.

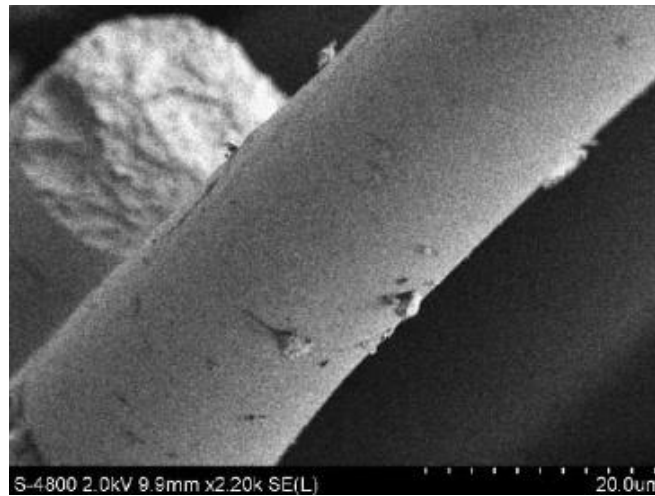


Figure 1.12: Smooth surface of fiber glass in the E-glass/polyurethane composite. Abdel-Magid et al. [2003]

Moreover, Figure 1.13 shows that the matrix in the E-glass/epoxy composite surrounds the fibers, indicating better interfacial bond between fiber and matrix.

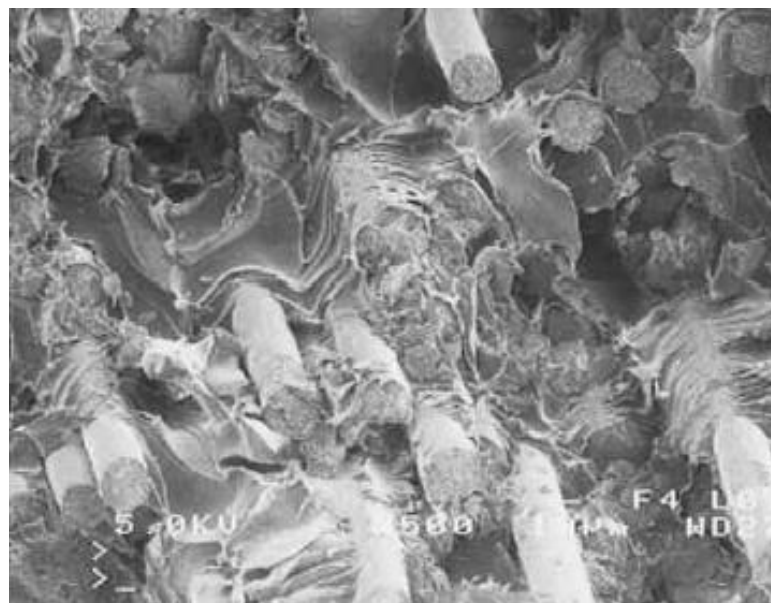


Figure 1.13: Tensile failure surfaces of E-glass/epoxy composite. Abdel-Magid et al. [2003]

This is further indicated by the rough surface of the fiberglass shown in the enlarged image in Figure 1.14.

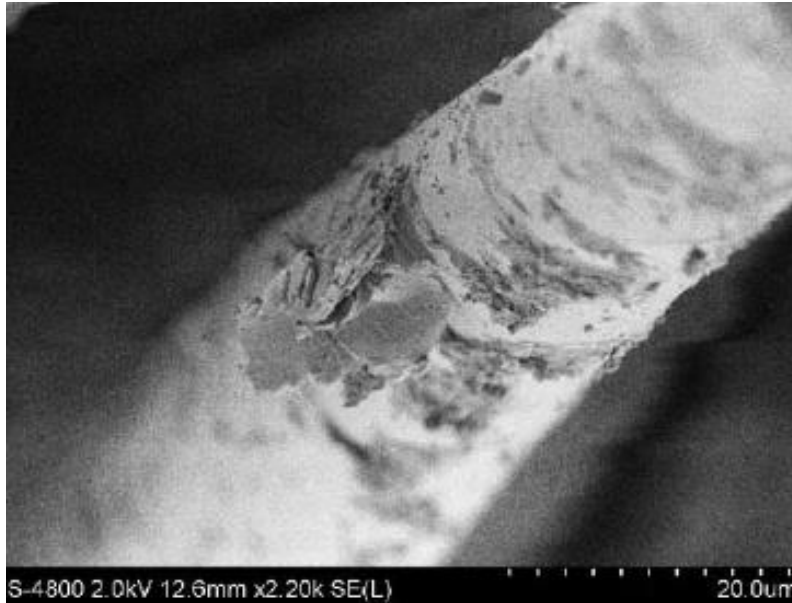


Figure 1.14: Surface of fiberglass in the E-glass/epoxy composite. Abdel-Magid et al. [2003]

The authors reported that the interfacial bonding is most likely responsible for the difference in the creep-rupture behavior of the two materials.

Furthermore, the experimental work performed by Kotelnikova-Weiler[2012] during her PhD thesis, highlighted the role of the matrix in the creep rupture of composites. Creep tests for different FRP specimens were performed by Kotelnikova-Weiler[2012] under various types of loading (bending, traction, compression and torsion) and at various load levels. At first, the static strength of the specimens under tension and bending loads was estimated and the failure modes of the specimens to bending and traction were presented (see Figure 1.15).



(a) *Traction*



(b) *Bending*

Figure 1.15: Static rupture modes for GFRPs in traction and bending. Kotelnikova-Weiler [2012]

When creep tests were performed, Kotelnikova-Weiler[2012] reported that the GFRP specimens attained creep rupture at load levels lower than their initial strength (see Figure 1.16).

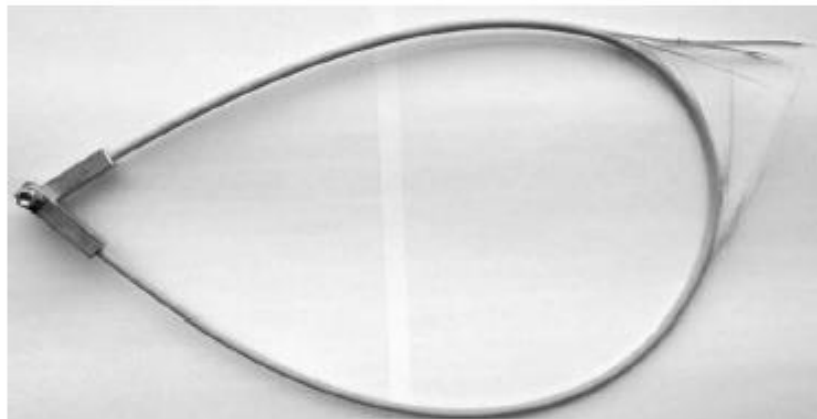


Figure 1.16: Creep rupture under bending load for GFRPs. Kotelnikova-Weiler [2012]

In order to stimulate the matrix element, Kotelnikova-Weiler[2012] combined torsion to the tension or compression loads. Instantaneous failure modes due to pure compression, to combined compression and torsion and combined traction and torsion were also presented by Kotelnikova-Weiler[2012] (see Figure 1.17).



Figure 1.17: Static rupture modes for a) compression, b) combined torsion-compression, c) combined torsion-traction. Kotelnikova-Weiler [2012]

The author reported that when pure compression load was applied to the specimen, kink band mode was observed (Figure 1.17a). The application of a torsional load combined with the compression induced an instantaneous crush of the sample leaving an almost clean surface (Figure 1.17b). Longitudinal cracking was observed for specimens where torsion and traction were combined (Figure 1.17c). In parallel to short term tests, creep tests were also performed with the combined loads configuration. Combined tension and torsion loads were applied to the specimens at different loading levels. Kotelnikova-Weiler[2012] proclaimed that; when torsion was combined with tension, the creep rupture of the specimens was accelerated (see Figure 1.18 for the creep rupture mode under combined tension and torsion).



Figure 1.18: Creep rupture when combining traction with torsion. Kotelnikova-Weiler [2012]

The experimental work of Lamon et al. [1997] showed that the failure of composites reinforced with SiC fibers is related to the presence of two partially concurrent flaw populations at the fibers level (extrinsic, intrinsic). The extrinsic flaws are located in the surface and the intrinsic flaws are located both in the surface and in the volume of SiC fibers. SEM examination of

fracture surfaces revealed the presence of fracture-inducing flaws located in the surface or in the interior of fibers (see Figures 1.19 and 1.20).

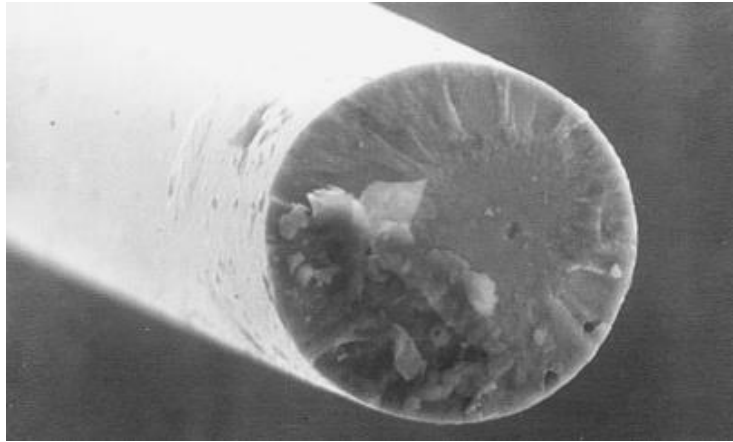


Figure 1.19: Volume fracture for SiC fibers. Lamon et al. [1997]

Surface-located fracture origins dominated failure at the low strengths or strains, whereas volume-located fracture origins were essentially identified in those fibers that failed at higher stresses or strains. It is worth mentioning that the Weibull's [1951] model is the most widely used for the description of the statistical distribution of failure strengths of fibers under uniaxial stress states. This model will be thoroughly explained in the following chapters.

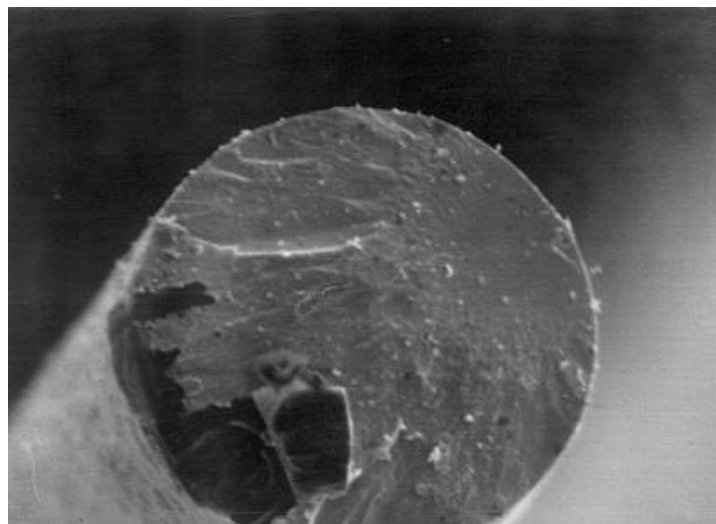


Figure 1.20: Surface fracture for SiC fibers. Lamon et al. [1997]

In addition to the role of the constituents (fibers, matrix, fiber/matrix interface), other factors may accelerate the creep of composites such as temperature and solicitation time. Figure 1.21 for example shows the evolution of the deformation with time curves at different temperatures

for GFRP specimens according to Kouadri-boudjelthia et al. [2009]. Figure 1.21 shows that the creep rupture is accelerated with the increase of temperature.

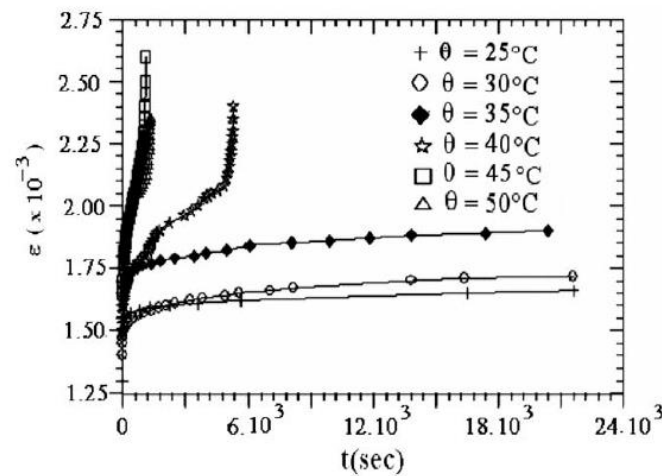


Figure 1.21: Evolution of the deformation with time for different temperatures for GFRPs.

Kouadri-boudjelthia et al. [2009]

Based on the role played by each of the composite constituents (fiber, matrix and fiber/matrix interface) in the creep rupture phenomena, Cox [1952] has introduced a method called shear-lag that allows estimating the stresses and strains in the microstructure of a unidirectional composite subjected to tension load. The author proposed an analytical model for determining the stresses around a single fiber break in a linear elastic matrix. Several enhancements were performed on the Cox's model by many researchers (Hedgepeth [1961], Hedgepeth and Dyke [1967], Lagoudas et al. [1989], Ochiai [1991], Sastry and Phoenix [1993], among others). Their work will be thoroughly detailed in chapter 2. An alternative approach to shear-lag theory for creep modeling of composites was the Finite Element method. Several researcher used this technique to compute the time dependent behavior of UD composites (Nedele and Wisnom [1994], Blassiau et al. [2007], Thionnet and Renard [1998], among others). A detailed literature review on the use of the Finite Element method for analyzing the creep of composite will also be presented in chapter 2. In this research work, we take benefit from the shear-lag and Finite Element modeling techniques to develop numerical models that allow us to analyze the behavior of unidirectional composite subjected to different loading patterns such as tension, compression, bending and shear. The analysis will be thoroughly detailed in chapters 2, 3 and 4.

1.5 Conclusion

The durability of composite materials was thoroughly discussed in this chapter. The effect of moisture/alkali solutions, thermal condition, creep and relaxation, fatigue, ultraviolet and fire on the life span of any structure constructed with FRPs was also highlighted. A literature review on the theoretical models that exists for creep prediction was also exposed. The advantage and the disadvantage of each model were explained showing that the creep of composites is still an open research topic. Several experimental works that led to identifying the influence of each of the composite constituents (fibers, matrix, and fiber/matrix interface) on creep rupture were presented. The aim of the literature review on creep was to understand its different stages and to know all the factors that accelerate it. All the above led us to choosing modeling techniques that accurately predicts the creep of composites. The shear-lag method based on the development of Beyerlein et al. [1998] and enhanced during the thesis Kotelnikova-Weiler[2012] was chosen to do such task. Since the proposed technique can model fiber breakage, fiber/matrix debonding and matrix viscoelasticity. However, several simplifications/assumptions were identified in the existing shear-lag model. The periodic boundary conditions for instance were neglected and representative volume element parameters were not properly justified. The enhancements and validation of the existing shear-lag model are thoroughly detailed in the following chapter.

Chapter 2: Modeling of short- and long-term behavior of FRPs under tension loads. Shear-lag vs. Finite Element models

In this chapter the mechanical behavior of unidirectional composites subjected to sustained tension load is analyzed. In order to perform this task, two modeling techniques are used. The first technique is based on the shear-lag theory (Beyerlein et al.[1998], Kotelnikova-Weiler [2012]). The second one is based on the Finite Element method. The shear-lag equations along with all the assumptions that were considered in the calculations are detailed in this chapter. A parametric analysis of the shear-lag model is also presented together with some enhancements to the existing technique. A comparative study between the developed shear-lag and Finite Element models is then presented.

Content

2.1 Introduction	33
2.2 Theoretical basis of the shear-lag model	35
2.2.1 Equilibrium equations.....	36
2.2.2 Superposition technique and the auxiliary problem of an isolated fiber break.	39
2.2.3 Multiple fiber breaks simulation.....	49
2.2.4 Computer simulations	58
2.2.5 Parameters of interest	63
2.2.6 Parametric analysis and validation	64
2.3 Finite Element Analysis	69
2.4 Comparison of shear-lag and Finite Element modeling results	71
2.4.1 Ultimate tensile strength	71
2.4.2 Creep tests.....	81
2.5 Conclusion.....	83

2.1 Introduction

As previously discussed in chapter 1, composites are subjected to degradation problems when exposed to heat, light, weathering, high energy radiation, chemicals, and microorganism. In addition to these environmental factors, and as consequence to the viscoelastic properties of the matrix part, composites deform with time when subjected to constant stress. The deformation of these materials with time (named creep) may lead to rupture. The creep of composite is divided into three stages. The primary region is the early stage of loading when the strain rate of the material decreases with time. Then it reaches a steady state which is called the secondary creep stage followed by a rapid increase (tertiary stage) and fracture. Tertiary creep or creep rupture can occur at load levels lower than the ultimate strength of the composites. Therefore it is of high interest to properly evaluate the creep of composites under different loading patterns. In this part of the thesis, we are interested in analyzing the behavior of composite under sustained tension load.

In order to properly understand the composites behavior under tension load, one must understand the sequence of its failure mechanism. At the matter of fact, failure of unidirectional composites occurs after accumulation of many fiber breaks (cluster formation of broken fibers), which are finally localized at a fracture plane perpendicular to the direction of the principle tensile stress. The matrix role is to connect the fibers and to transfer the shear forces. The fibers are the main load bearing elements. However, the viscoelastic behavior of the matrix element is responsible for the creep behavior of the composite at the macro scale. Based on these facts, Cox [1952] has introduced a method called shear-lag that allows to estimate the stresses and strains in the microstructure of a unidirectional composite subjected to tension load. The author proposed an analytical model for determining the stresses around a single fiber break in a linear elastic matrix. However, Cox neglected the effect of the surrounding fibers and the effect of the matrix stiffness in parallel to the fiber direction. Hedgepeth [1961] removed this limitation and generalized Cox's model in two dimensions (2D shear-lag model). Hedgepeth numerical model allows to estimate the overstress factors induced by a single fiber break to its neighboring intact fibers in a two dimensional unidirectional composite. The author demonstrated that the broken fiber sheds its load to nearby intact fibers which causes stress concentration in the fibers near the break site. Later Hedgepeth and Dyke [1967] extended the above work in three dimensions, by considering both square and hexagonal spatial configurations for the fibers. The overstress factors induced by fiber breaks were estimated based on the nearest neighbor approximation, i.e. only the immediate fibers next to the broken one were affected by the break. The overstress

factors calculated by Hedgepeth and Dyke [1967] in their 3D analysis were smaller than the ones calculated when 2D configuration was considered (Hedgepeth [1961]). This fact proves that 2D calculations are conservative and can be considered for applications. Moreover, Lagoudas et al. [1989] introduced the viscoelastic behavior of the matrix to the modeling process. The authors calculated the evolution with time of fiber and matrix stresses around an arbitrary array of fiber breaks in a unidirectional composite subjected to tension load. Ochiai [1991] completed these models by taking into account the matrix stiffness parallel to the direction of the fibers.

In the aforementioned shear-lag models, the fiber breaks were a priori imposed as defects in the composite material and new fiber breaks were not possible. Beyerlein et al.[1998] developed a computational technique, called viscous break interaction, allowing to determine the evolution with time of fiber and matrix stresses around an arbitrary array of fiber breaks in a unidirectional composite. In their model, new fiber breaks are allowed. However, Beyerlein et al.[1998] neglected the effect of fiber/matrix debonding when viscoelastic matrix behavior is considered. This phenomena was taken into account by Kotelnikova-Weiler[2012] by considering a viscous behavior for the matrix element combined with fiber/matrix debonding. The aforementioned model that was developed in the work of Kotelnikova-Weiler[2012] is presented, enhanced and validated in this chapter. In particular, an extensive parametric study regarding the time integration and the spatial discretization is performed. This allowed to investigate the convergence of the numerical results of the shear-lag theory. The existing numerical model was also extended in order to take into account periodic boundary conditions that enable the derivation of the effective properties of the material.

In the aim of validating the shear-lag model, a Finite Element model was also developed in this thesis. It is worth mentioning that the Finite Element method was used by several researchers (Nedele and Wisnom [1994], Thionnet and Renard[1998], Xia, Chen, and Ellyin [2000]) as alternative to shear-lag theory for studying the creep of composites. However, these Finite Element models do not account for the graduate breakage of the fibers and the evolution of the mechanical behavior of UD composites in time (creep). Moreover, they do not perform stochastic analyses (MonteCarlo) which is important for determining the expected ultimate strength and time behavior of the material.

2.2 Theoretical basis of the shear-lag model

In this part of the chapter, we summarize the shear lag equations that are based on the study of Beyerlein et al.[1996], Beyerlein et al.[1998] and recently extended (by developing a software that simulates fiber/matrix debonding) by Kotelnikova-Weiler [2012]. The current model predicts the behavior of a 2D unidirectional fiber reinforced composite subjected to tension load. The statistical variability in fibers strength, the viscous behavior of the matrix and the fiber-matrix debonding are taken into account in the calculations. The fibers are considered as the load bearing elements. Their behavior is linear and elastic. However, the axial stiffness of the matrix is neglected. Its role is to transfer shear forces between the fiber elements. Moreover, the shear stresses transferred by the matrix are limited to a certain plafond in order to model fiber/matrix debonding.

The geometry of the model is illustrated in Figure 2.1. The fibers and matrix are represented in a 2D brick-like discretization. In fact, the model is reduced to one dimensional model along the direction of the fibers as the fields depend only on the abscissa (x dimension) of the fiber/matrix elements. We consider a UD composite made of $2N + 1$ fibers.

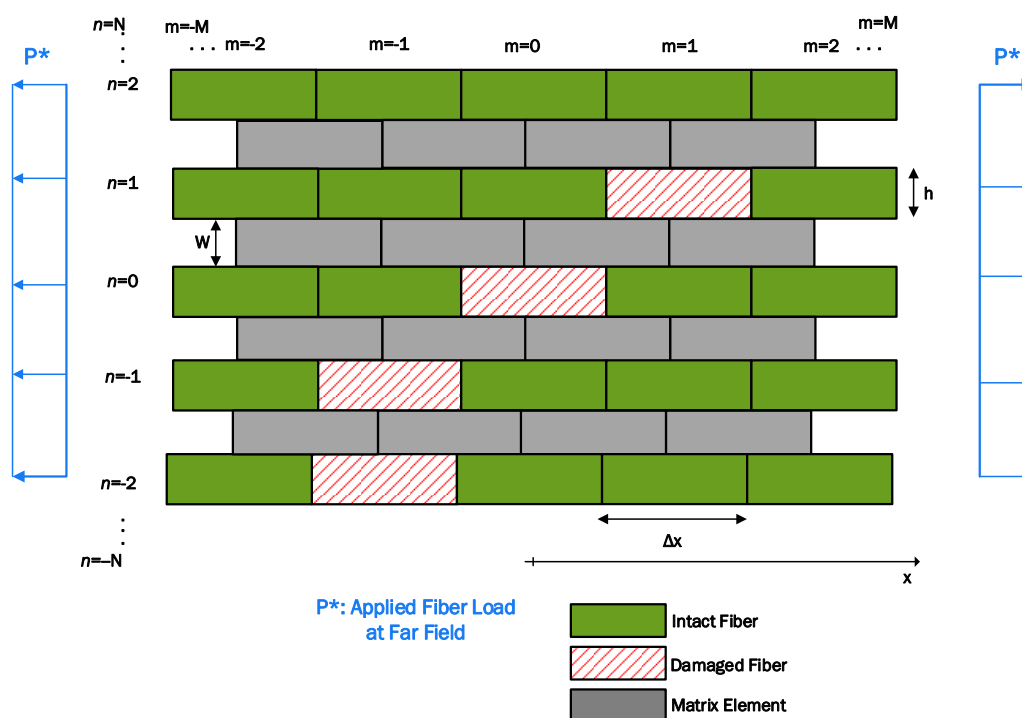


Figure 2.1: Shear-lag model discretization

2.2.1 Equilibrium equations

The following equations are used to model the tensile behavior of unidirectional composites. At first, we present the Beyerlein et al. [1998] shear-lag equations. Then, we describe the adjustments performed by Kotelnikova-Weiler [2012] in order to add the fiber/matrix debonding to the modeling process.

The central fiber number is $n=0$. The fibers above are numbered with a positive index while those below with negative. The matrix bay above the fiber n is matrix bay n . Each fiber is divided in the longitudinal direction into elements numbered from $m=-M$ to $m=+M$. Matrix bands are also divided longitudinally into elements. Fiber and matrix elements are positioned in staggered rows.

The local equilibrium equation of a fiber element is:

$$\frac{\partial \sigma_n(x, T)}{\partial x} + \frac{\tau_n(x, T) - \tau_{n-1}(x, T)}{h} = 0 \quad (2.1)$$

where $\sigma_n(x, T)$ is the axial stress in the fiber n at the longitudinal coordinate x at time T , $\tau_n(x, T)$ is the shear stress in the matrix band n and h is the fiber diameter.

Assuming firstly a perfect bonding between the matrix and fibers (Beyerlein et al. [1998]), then the matrix shear deformation, $\gamma_n(x, T)$, is related to the fiber nodes displacements by the following equation:

$$\gamma_n(x, T) = \frac{u_{n+1}(x, T) - u_n(x, T)}{w} \quad (2.2)$$

where u_n is the fiber nodes axial displacement and w is the matrix band width.

Assuming that the fibers are linear elastic until failure (fiber breakage) we have:

$$\sigma_n(x, T) = E_f \varepsilon_n(x, T) = E_f \frac{\partial u_n(x, T)}{\partial x} \quad (2.3)$$

where E_f is the fiber Young's modulus and $\varepsilon_n(x, T)$ is the fiber axial strain.

At first, the matrix is assumed to be linear viscoelastic and its shear stress $\tau_n(x, T)$ is related to the history of the shear strain $\gamma_n(x, T)$ by the following equation:

$$\tau_n(x, T) = \int_{-\infty}^T G(T - T') \frac{\partial \gamma_n(x, T')}{\partial T'} dT' \quad (2.4)$$

where $G(T)$ is the matrix relaxation function. The axial stiffness of the matrix is neglected as it is very small compared to the stiffness of the fibers.

The power law expression of the matrix's creep function $J(T)$ can be written with (see Lagoudas et al. [1989]):

$$J(T) = J_e (T/T_c)^\alpha \quad (2.5)$$

where α is the creep exponent (with $0 \leq \alpha \leq 1$), J_e is the elastic compliance of the matrix and T_c is the matrix relaxation characteristic time constant.

Combining equations (2.1) to (2.4), the following differential equation is obtained where u_n represents $u_n(x, T)$

$$E_f \frac{\partial^2 u_n}{\partial x^2} + \frac{1}{wh} \times \int_{-\infty}^T G(T - T') \frac{\partial}{\partial T'} (u_{n+1} - 2u_n + u_{n-1}) dT' = 0 \quad (2.6)$$

The next step is to introduce normalizations constants:

$$\xi = \frac{x}{\sqrt{\frac{wE_fAJ_e}{h}}} \quad (2.7)$$

$$t = \frac{T}{T_c} \quad (2.8)$$

where A is the fiber cross section.

Under a constant fiber tensile load p^* , applied at the far field $x = \pm\infty$, for $t > 0$, the normalized fiber displacement $U_n(\xi, t)$ and the normalized fiber load $P_n(\xi, t)$ can be expressed using equations 2.9 and 2.10.

$$U_n(\xi, t) = \frac{u_n(x, T)}{p^* \sqrt{\frac{wJ_e}{hE_fA}}} \quad (2.9)$$

$$P_n(\xi, t) = \frac{p_n(x, T)}{p^*} \quad (2.10)$$

The normalized, dimensionless version of the matrix shear stresses $T_n(\xi, t)$, strains $\Gamma_n(\xi, t)$ and the strain rate $\partial\Gamma_n(\xi, t)/\partial t$ can be written as:

$$T_n(\xi, t) = \frac{\tau_n(x, T)\sqrt{hwE_fAJ_e}}{p^*} \quad (2.11)$$

$$\Gamma_n(\xi, t) = \frac{\gamma_n(x, T)}{p^*} \sqrt{\frac{E_fAhw}{J_e}} = U_{n+1}(\xi, t) - U_n(\xi, t) \quad (2.12)$$

$$\frac{\partial\Gamma_n(\xi, t)}{\partial t} = \frac{\{\partial\gamma_n(x, T)/\partial T\}T_c}{p^*} \sqrt{\frac{E_fAhw}{J_e}} \quad (2.13)$$

The normalized relaxation modulus $G(t)$ is expressed with:

$$G(t) = \frac{G(T_c t)}{G_e} \quad (2.14)$$

And the normalized creep compliance $J(t)$ is:

$$J(t) = \frac{J(T_c t)}{J_e} \quad (2.15)$$

where G_e is the elastic matrix shear compliance and its is inverse of J_e .

In order to make the equation (2.6) dimensionless, we introduce the dimensionless variables in equations (2.7) to (2.15). We obtain the following equation:

$$\frac{\partial^2 U_n}{\partial \xi^2} + \int_{-\infty}^t G(t-t') \frac{\partial}{\partial t'} (U_{n+1} - 2U_n + U_{n-1}) dt' = 0 \quad (2.16)$$

where t' is a normalized integration variable.

Boundary conditions

In the problem at hand, a constant load p^* is applied at the far field and the fibers loads are null at fibers break sites. Therefore, the boundary conditions can be expressed with the following equations:

$$p_n(x, T) = p^* \forall n ; \text{At } x = \pm\infty \text{ for } t > 0 \quad (2.17)$$

$$P_{n_r}(x_r, T) = 0 \text{ with } (n_r, x_r) \text{ coordinates of rupture sites.} \quad (2.18)$$

If we write these equations in their dimensionless form we obtain:

$$P_n(\xi, t) = \frac{\partial U_n}{\partial \xi}(\xi, t) = 1 \quad \forall n ; \text{At } \xi = \pm\infty \text{ for } t > 0 \quad (2.19)$$

$$P_{n_r}(\xi_r, t) = \frac{\partial U_{n_r}}{\partial \xi}(\xi_r, t) = 0 \text{ With } (n_r, \xi_r) \text{ coordinates of rupture sites} \quad (2.20)$$

In order to solve equation (2.16) with the boundary conditions (2.19) and (2.20), the first step is to take the Laplace transform which leads to equation (2.21)

$$\frac{\partial^2 \underline{U}_n(\xi, s)}{\partial \xi^2} + s \underline{G}(s) \left(\underline{U}_{n+1}(\xi, s) - 2\underline{U}_n(\xi, s) + \underline{U}_{n-1}(\xi, s) \right) = 0 \quad (2.21)$$

Where s is the Laplace transform variable and $\underline{F}(s)$ is the Laplace transform of $F(t)$.

The second step, as per Beyerlein et al. [1998], is the superposition technique. We summarize the steps considered in the superposition technique in the following paragraph.

2.2.2 Superposition technique and the auxiliary problem of an isolated fiber break

According to Beyerlein et al. [1998], the general problem P1 in which a composite material with several staggered fiber breaks and subjected at the far field to a unit traction load can be seen as a superposition of two sub problems. The first one, SP1, is that of an unloaded material subjected to a unit compressive force applied at the tips of every broken fiber. The second sub problem SP2 considers an intact material subjected to a constant tension load at the far field (see Figure 2.2).

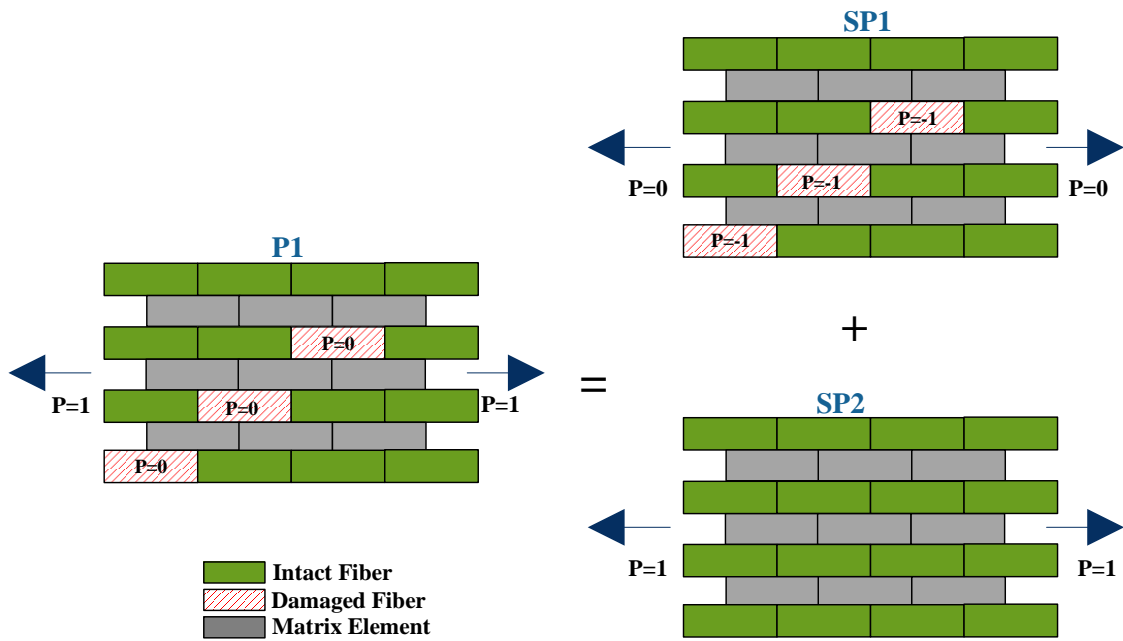


Figure 2.2: General problem $P1$ as a superposition of $SP1$ and $SP2$

Solution of the subproblem $SP1$

In the subproblem of the damaged material $SP1$, the stress in a fiber results from a weighted superposition of the stress fields of each one of the individual rupture sites. The next step is therefore to solve the stress distribution induced by an isolated fiber break localized at the center of the. Then, the weight function $K_i(t)$ must be evaluated in order to take into account the influence of each of the individual rupture sites on the stresses and strains of the composite as entity (see Figure 2.3). The isolated fiber break problem is named $A1$.

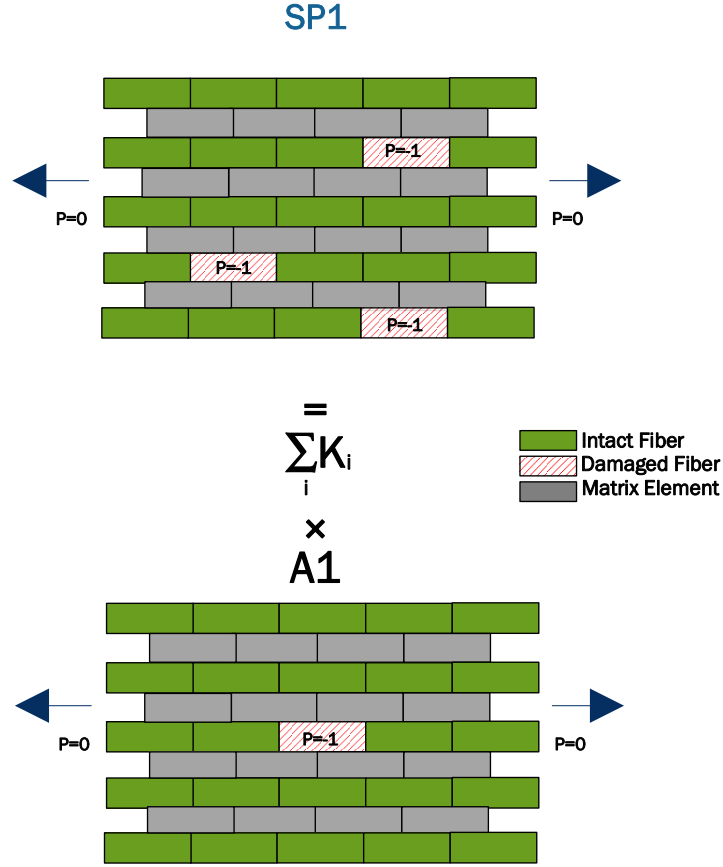


Figure 2.3: Subproblem SP1

Auxiliary problem A1:

We remind that the auxiliary problem A1 is that of an unloaded material subjected to a compression load at the central fiber element. The solution of the auxiliary problem A1 is obtained when calculating the fibers node displacements $V_n^u(\xi, t)$, the axial load in the fibers $L_n^u(\xi, t)$ and the shear stress in the matrix $T_n^u(\xi, t)$.

The boundary conditions for the auxiliary problem A1 are presented below:

$$L_n^u(\xi, t) = \frac{\partial V_n^u(\xi, t)}{\partial \xi} = 0 \quad \forall n \text{ and } \xi = \pm\infty \text{ for } t > 0 \quad (2.22)$$

$$L_{n,r}^u(\xi_r, t) = \frac{\partial V_{n,r}^u(\xi, t)}{\partial \xi} = -1 \quad (n_r, \xi_r) = (0, 0) \text{ for } t \geq 0 \quad (2.23)$$

We note that the displacement field is antisymmetric about the plane $\xi = 0$ therefore:

$$V_n^u(0, t) = 0 \forall |n| > 0 \text{ and } t \geq 0 \quad (2.24)$$

If we apply the Laplace transform to the previously mentioned conditions at equations (2.22), (2.23) and (2.24) we obtain the following:

$$\underline{L}_n^u(\xi, s) = \frac{\partial V_n^u(\xi, s)}{\partial \xi} = 0 \quad \forall n \text{ and } \xi = \pm\infty \text{ for } s > 0 \quad (2.25)$$

$$\underline{L}_{n,r}^u(\xi_r, s) = \frac{\partial V_{n,r}^u(\xi, s)}{\partial \xi} = \frac{-1}{s} \quad (n_r, \xi_r) = (0, 0) \text{ for } s \geq 0 \quad (2.26)$$

$$\underline{V}_n^u(0, s) = 0 \forall |n| > 0 \text{ and } s \geq 0 \quad (2.27)$$

And since the displacement field is antisymmetric $\underline{V}_n^u = \underline{V}_{-n}^u$.

An auxiliary function can be constructed from the V_n^u functions as follows:

$$\underline{V} = \frac{V_0^u}{\pi} + \frac{2}{\pi} \sum_{n=1}^{\infty} \underline{V}_n^u \cos(n\theta) \quad 0 < \theta < \pi \quad (2.28)$$

where $\underline{V} = \underline{V}(\xi, s, \theta)$ and $\underline{V}_n^u = \underline{V}_n^u(\xi, s)$. And the \underline{V}_n^u functions can be found through:

$$\underline{V}_n^u = \int_0^{\pi} \underline{V} \cos(n\theta) d\theta \quad (2.29)$$

Multiplying equation (21) by $\frac{\cos(n\theta)}{\pi}$ and summing from $n = -\infty$ to $n = +\infty$, we obtain:

$$\frac{\partial^2 \underline{V}}{\partial \xi^2} - 4s\underline{G} \sin^2\left(\frac{\theta}{2}\right) \underline{V} = 0 \quad (2.30)$$

Indeed while summing, one can notice the following arrangement from equations $n + 1$ and $n - 1$, regrouping members with V_n :

$$\begin{aligned} & V_n(\cos((n-1)\theta) - 2\cos(n\theta) + \cos((n+1)\theta)) \\ &= V_n(\cos(n\theta)\cos(\theta) + \sin(n\theta)\sin(\theta) - 2\cos(n\theta) \\ &+ \cos(n\theta)\cos(\theta) - \sin(n\theta)\sin(\theta)) \\ &= 2\cos(n\theta)V_n(\cos(\theta) - 1) = -4\cos(n\theta)\sin^2(\theta/2) \end{aligned}$$

In order to solve the equation (2.30) with boundary conditions (2.31), (2.32) and (2.33), Lagoudas et al. [1989] proposed the equation (2.34) for describing \underline{V} :

$$\frac{\partial \underline{V}}{\partial \xi} = 0 \quad \text{for } \xi = \pm\infty \quad (2.31)$$

$$\int_0^\pi \frac{\partial \underline{V}}{\partial \xi} \cos(n\theta) d\theta = -\frac{1}{s} \quad \text{where } (n_r, \xi_r) = (0,0) \quad (2.32)$$

$$\int_0^\pi \underline{V} \cos(n\theta) d\theta = 0 \quad \forall |n| > 0 \text{ and } \xi = 0 \quad (2.33)$$

$$\underline{V} = f(s, \theta) \exp\left(-2C_\theta \xi \sqrt{s\underline{G}(s)}\right) \quad (2.34)$$

where $C_\theta = \sin\left(\frac{\theta}{2}\right)$ and $f(s, \theta)$ is an unknown function to be determined using the remaining boundary conditions.

When combining equations (2.32) and (2.34), we obtain the following:

$$2s\sqrt{s\underline{G}(s)} \int_0^\pi f(s, \theta) C_\theta d\theta = 1 \quad \text{Where } (n_r, \xi_r) = (0,0) \quad (2.35)$$

Lagoudas suggested the following form for the function f :

$$f(s, \theta) = \frac{b_0}{2s\sqrt{s\underline{G}(s)}} \quad (2.36)$$

Combining equations (2.35) and (2.36) gives $b_0 = 1/2$

And the condition (2.33) is satisfied, therefore the solution of the equation (2.30) can be written by:

$$\underline{V}_n^u(\xi, s) = \int_0^\pi \frac{\exp(-2C_\theta \xi \sqrt{s\underline{G}(s)}) \cos(n\theta)}{4s\sqrt{s\underline{G}(s)}} d\theta \quad (2.37)$$

For symmetry reasons on the whole range of ξ from $-\infty$ to $+\infty$:

$$\underline{V}_n^u(\xi, s) = \frac{\text{sgn}(\xi)}{4s\sqrt{s\underline{G}(s)}} \int_0^\pi \exp\left(-2C_\theta |\xi| \sqrt{s\underline{G}(s)}\right) \cos(n\theta) \quad (2.38)$$

$$\text{where } \text{sgn}(z) := \begin{cases} -1 & \text{if } z < 0 \\ 0 & \text{if } z = 0 \\ 1 & \text{if } z > 0 \end{cases}$$

In equation (2.38) we present the solution in the Laplace domain of the auxiliary problem A1 of an isolated broken fiber in an infinite lamina with zero load applied at the far field and with a unite compressive load applied at the fracture tips. In order to obtain the solution in the time domain $V_n^u(\xi, t)$, one must apply the inverse Laplace transform to equation (2.38).

$$V_n^u(\xi, t) = L^{-1} \{ \underline{V}_n^u(\xi, s) \} \quad (2.39)$$

$$V_n^{u,s}(\xi, t) = \frac{\text{sgn}(z)}{4} \times \int_0^\pi \cos(n\theta) L^{-1} \left\{ \frac{\exp(-2C_\theta |\xi| \sqrt{s\underline{G}(s)})}{s \sqrt{s\underline{G}(s)}} \right\} d\theta \quad (2.40)$$

where ^s stands for the Schapery inversion technique.

Comparison between the direct Schapery's inversion technique and the Bromwich integral formula

In the study of Beyerlein et al. [1998], the direct Schapery's inversion technique was proven appropriate for this problem in the range of $\alpha < 0.5$. Good agreement was found between the Schapery's inversion technique and other methods such as the Bromwich integral formula for the whole range of α where axial fiber loads and displacements were compared.

First the expression of the fiber's axial stress and displacement as well as of the matrix shear stress are calculated using the Schapery's inversion technique, then a comparison with the expressions calculated using the Bromwich integral formula is performed.

When using the Schapery's inversion technique, the inversion of a given formula can be found through:

$$v(t) = sv(s) |_{s=\exp(-\gamma_E)/t} \quad (2.41)$$

where $\gamma_E \cong 0.5772$ is the Euler constant.

Considering the power law expression of the matrix's creep function (Eq 2.5) and the relationship between the Laplace transform of the matrix's creep compliance and the relaxation modulus (Eq 2.42), the following expression of the Laplace transform of the matrix's relaxation function can be written with (Eq. 2.43):

$$s\underline{G}(s) = \frac{1}{s\underline{J}(s)} \quad (2.42)$$

$$s\underline{G}(s) = \frac{1}{s\underline{J}(s)} = \frac{s^\alpha}{\Gamma(1+\alpha)} \quad (2.43)$$

Combining equations (2.40) and (2.43) we obtain the following expression:

$$V_n^{u,s}(\xi, t) = \frac{\text{sgn}(z)}{4} \times \int_0^\pi \cos(n\theta) L^{-1} \left\{ \frac{\exp\left(-2C_\theta |\xi| \sqrt{\frac{s^\alpha}{\Gamma(1+\alpha)}}\right)}{s \sqrt{\frac{s^\alpha}{\Gamma(1+\alpha)}}} \right\} d\theta \quad (2.44)$$

$g(s)$ is expressed with:

$$g(s) = \frac{\exp\left(-2C_\theta |\xi| \sqrt{\frac{s^\alpha}{\Gamma(1+\alpha)}}\right)}{s \sqrt{\frac{s^\alpha}{\Gamma(1+\alpha)}}} \quad (2.45)$$

Then:

$$L^{-1}\{g(s)\} = g(t) = sg(s)|_{s=\exp(-\gamma_E)/t} \quad (2.46)$$

$$sg(s)|_{s=\exp(-\gamma_E)/t} = \frac{\exp\left(-2C_\theta |\xi| \sqrt{\frac{s^\alpha}{\Gamma(1+\alpha)}}\right)}{s \sqrt{\frac{s^\alpha}{\Gamma(1+\alpha)}}} \Big|_{s=\exp(-\gamma_E)/t} \quad (2.47)$$

Replacing s by its expression leads to the following:

$$g(t) = \frac{\exp\left(-2C_\theta |\xi| \sqrt{\frac{\exp(-\alpha\gamma_E)}{t^\alpha \Gamma(1+\alpha)}}\right)}{\sqrt{\frac{\exp(-\alpha\gamma_E)}{t^\alpha \Gamma(1+\alpha)}}} = \frac{t^{\alpha/2} \exp\left(-2C_\theta |z| \sqrt{\frac{\exp(-\alpha\gamma_E)}{\Gamma(1+\alpha)}}\right)}{\sqrt{\frac{\exp(-\alpha\gamma_E)}{\Gamma(1+\alpha)}}} \quad (2.48)$$

where $z = \xi/t^{\alpha/2}$

And if we consider $\beta_s = \sqrt{\frac{\exp(-\alpha\gamma_E)}{\Gamma(1+\alpha)}}$ then $g(t)$ can be expressed with (2.49):

$$g(t) = \frac{t^{\alpha/2}}{\beta_s} \exp(-2C_\theta |z| \beta_s) \quad (2.49)$$

Which leads to the following expression for the fiber node displacement $V_n^{u,s}(\xi, t)$, where s stands for Schapery inversion technique:

$$V_n^{u,s}(\xi, t) = \frac{sgn(z)}{4} \frac{t^{\alpha/2}}{\beta_s} \times \int_0^\pi \cos(n\theta) \exp(-2C_\theta |z| \beta_s) d\theta \quad (2.50)$$

The fiber axial load $L_n^{u,s}(\xi, t)$ and the matrix shear stress $T_n^{u,s}(\xi, t)$ could be found in the same manner.

For the fiber axial load:

$$\underline{L}_n^u(\xi, s) = \frac{\partial V_n^u(\xi, s)}{\partial \xi} \quad (2.51)$$

$$L_n^{u,s}(\xi, t) = -\frac{1}{2} \times \int_0^\pi \cos(n\theta) C_\theta L^{-1} \left\{ \frac{1}{s} \exp\left(-2C_\theta |\xi| \sqrt{s\underline{G}(s)}\right) \right\} d\theta \quad (2.52)$$

$$L_n^{u,s}(\xi, t) = -\frac{1}{2} \times \int_0^\pi \cos(n\theta) C_\theta \exp(-2C_\theta |z| \beta_s) d\theta \quad (2.53)$$

And for the matrix shear stress:

$$\underline{T}_n^u(\xi, s) = s\underline{G}(s) \left(\underline{V}_{n+1}^u(\xi, s) - \underline{V}_n^u(\xi, s) \right) \quad (2.54)$$

$$\begin{aligned} T_n^{u,s}(\xi, t) &= \frac{sgn(z)}{4} \\ &\times \int_0^\pi (\cos((n+1)\theta) - \cos(n\theta)) L^{-1} \left\{ \frac{\sqrt{s\underline{G}(s)}}{s} \exp\left(-2C_\theta |\xi| \sqrt{s\underline{G}(s)}\right) \right\} d\theta \end{aligned} \quad (2.55)$$

$$T_n^{u,s}(\xi, t) = \frac{sgn(z)}{4} \frac{\beta_s}{t^{\alpha/2}} \times \int_0^\pi (\cos((n+1)\theta) - \cos(n\theta)) \exp(-2C_\theta |z| \beta_s) d\theta \quad (2.56)$$

Expressions (2.50), (2.53) and (2.56) allow estimating the displacement and the stress fields in a unloaded unidirectional composite subjected to a unique fiber break located at its center along with a unit compression load at the fiber break (see Figure 2.3).

It is worth mentioning that in the dimensionless form of the previously mentioned equations of displacement and stresses, the only mechanical parameter represented is the power of the power law expression of the matrix's behavior (α). Consequently, a change in the value of α can lead to a major modification in the composites behavior. The remaining mechanical or geometrical parameters (E_f, A, h, w, J_e) are included in the constant used for the abscissa normalization.

In the study of Beyerlein et al. [1998], the expressions of the fiber node displacement/axial load and the matrix shear stress calculated using the Bromwich integral formula are given with the below expressions:

$$\begin{aligned}
V_n^u(\xi, t) &= \frac{\operatorname{sgn}(z) t^{\alpha/2}}{4 \beta_0} \\
&\times \int_0^\pi \cos(n\theta) \exp(-2C_\theta |z| \beta_0) d\theta \\
&- \operatorname{sgn}(z) K_2(\alpha) t^{\alpha/2} |z|^2 \int_0^\pi \cos(n\theta) C_\theta^2 \exp(-2C_\theta |z| \beta_0) d\theta
\end{aligned} \tag{2.57}$$

$$\begin{aligned}
L_n^u(\xi, t) &= -\frac{1}{2} \\
&\times \int_0^\pi \cos(n\theta) C_\theta \exp(-2C_\theta |z| \beta_0) d\theta \\
&- K_1(\alpha) |z| \int_0^\pi \cos(n\theta) C_\theta^2 \exp(-2C_\theta |z| \beta_0) d\theta
\end{aligned} \tag{2.58}$$

$$\text{where } \beta_0 = \frac{\Gamma(1+\frac{\alpha}{2})}{\sqrt{\Gamma(1+\alpha)}} \tag{2.59}$$

$$K_1(\alpha) = \frac{\left(\frac{\pi\alpha}{2}\right)^2}{6} \beta_0 \tag{2.60}$$

$$K_2(\alpha) = \frac{\left(\frac{\pi\alpha}{2}\right)^2}{12} \beta_0 \tag{2.61}$$

For the local equilibrium to be satisfied, the following equation needs to be verified:

$$\frac{\partial L_n^u(\xi, t)}{\partial \xi} + T_n^u(\xi, t) - T_{n-1}^u(\xi, t) = 0 \tag{2.62}$$

We then propose an expression for the matrix shear stress, which verifies this equation:

$$\begin{aligned}
T_n^u(\xi, t) &= \frac{(\beta_0 - K_1)}{4t^{\alpha/2}} \int_0^\pi (\cos((n+1)\theta) - \cos n\theta) \exp(-2C_\theta |z|\beta_0) d\theta \\
&+ |z| \frac{\beta_0 K_1}{2t^{\alpha/2}} \int_0^\pi C_\theta (\cos((n+1)\theta) \\
&- \cos n\theta) \exp(-2C_\theta |z|\beta_0) d\theta
\end{aligned} \tag{2.63}$$

A comparison between Schapery's inversion technique and Bromwich integral formula was performed using the expressions (2.50), (2.53), (2.56), (2.57), (2.58) and (2.63) that lead to the following conclusion. For the instantaneous response of the specimen ($t=1$), axial stresses were calculated for the intact fibers near the break site and shear stresses in the neighboring matrix bands as well. For $\alpha = 0.5$, the difference between the two inversions techniques was estimated to be 1% in the fiber axial stress and 5.8% in the shear stress of the closest matrix band which confirms that Schapery's inversion technique could be used for calculation where $\alpha < 0.5$. However, for $\alpha = 1$, the difference in fiber axial stress remains lower than 6% but shear stress differs considerably with about a maximum difference of 38%. Therefore when debonding is investigated, the Schapery's inversion technique should not be used for $\alpha > 0.5$. Since the values of α are less than 0.5 in the calculations during this research work, the Schapery's inversion technique results remain satisfactory even when matrix shear stresses need to be computed.

As a conclusion of the above calculations, the solution of the auxiliary problem A1 showing displacement and axial load in the fibers as well as the shear stress in the matrix is given in equation below (Equations (2.50), (2.53) and (2.56)). The solution of this problem is marked with an exponent ^u; the exponent ^s in the formulas stands for Schapery's direct inversion technique.

$$V_n^{u,s}(\xi, t) = \frac{\text{sgn}(z) t^{\alpha/2}}{4 \beta_s} \times \int_0^\pi \cos(n\theta) \exp(-2C_\theta |z|\beta_s) d\theta \tag{2.50}$$

$$L_n^{u,s}(\xi, t) = -\frac{1}{2} \times \int_0^\pi \cos(n\theta) C_\theta \exp(-2C_\theta |z|\beta_s) d\theta \tag{2.53}$$

$$T_n^{u,s}(\xi, t) = \frac{\text{sgn}(z) \beta_s}{4 t^{\alpha/2}} \times \int_0^\pi (\cos((n+1)\theta) - \cos(n\theta)) \exp(-2C_\theta |z|\beta_s) d\theta \tag{2.56}$$

2.2.3 Multiple fiber breaks simulation

In order to obtain the solution of the general problem P1, one must calculate the weight functions $K_{ij}(t)$ (see Beyerlein et al. [1998]). The procedure to determine the weight functions is described further. At each time step we calculate the load transmission functions $\Lambda_{ij}(t)$ defined by the following expression:

$$\Lambda_{ij}(t) = L_{n_i - n_j}^{u,s}(\xi_i - \xi_j, t) = -\frac{1}{2} \times \int_0^\pi \cos(n_{ij}\theta) C_\theta \exp(-2C_\theta |z_{ij}| \beta_s) d\theta \quad (2.64)$$

where $n_{ij} = n_i - n_j$ and $z_{ij} = \frac{\xi_i - \xi_j}{t^{\alpha/2}}$

$\Lambda_{ij}(t)$ is the proportion of the load transmitted from fiber break j located at (n_j, ξ_j) to a fiber break i located at (n_i, ξ_i)

In order to calculate $K_{ij}(t)$, the following system of equations needs to be solved:

$$\{K_{ij}(t)\} = [\Lambda_{ij}(t)]^{-1} \{P\} \quad (2.65)$$

Therefore, the solution of the sub problem SP1 with r staggered fiber breaks can be written with:

$$L_n(\xi, t) = \sum_{j=1}^r L_{n-n_j}^u(\xi - \xi_j, t) K_j(t) \quad (2.66)$$

$$V_n(\xi, t) = \sum_{j=1}^r V_{n-n_j}^u(\xi - \xi_j, t) K_j(t) \quad (2.67)$$

$$\Gamma_n(\xi, t) = \sum_{j=1}^r \Gamma_{n-n_j}^u(\xi - \xi_j, t) K_j(t) \quad (2.68)$$

The trivial solution of the Sub problem SP2 must be added to equations (2.66), (2.67) in order to obtain the solution of the general problem P1:

$$P_n(\xi, t) = L_n(\xi, t) + 1 \quad (2.69)$$

$$U_n(\xi, t) = V_n(\xi, t) + \xi \quad (2.70)$$

In the previously mentioned equations, fiber/matrix debonding was neglected. In order to take into account the debonding that occurs between the fibers and the matrix, multiple adaptations need to be implemented in the previous equations. As in Kotelnikova-Weiler [2012], the general problem (P1') in which a composite material with several staggered fiber breaks and matrix debonded regions is subjected to a unit traction load at the far field, can be seen as a superposition of two sub problems. The first one (SP1') is that of an unloaded material for which a unit compressive force is applied at the tips of every broken fiber and a constant frictional stress is imposed at the matrix debonded regions. The second subproblem (SP2) considers an intact material with continuous fibers subjected to a constant tension load (see Figure 2.4). The solution of subproblem SP1' can be obtained through a weighted superposition of two auxiliary problems A1 and A2 (see Figure 2.5). The auxiliary problem A1 is that of an isolated fiber break localized at the center of an unloaded composite. The auxiliary problem A2 is that of a central matrix element subjected to shear force induced by axial loads applied to neighboring fiber elements.

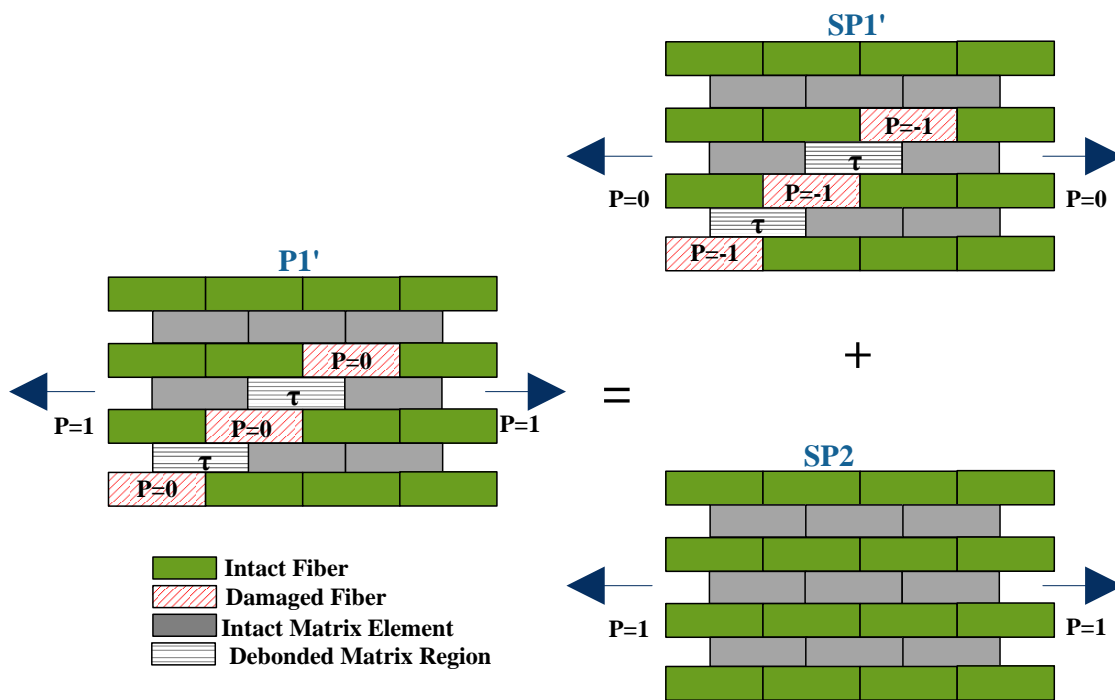


Figure 2.4: Superposition technique adopted in order to solve the problem P1'

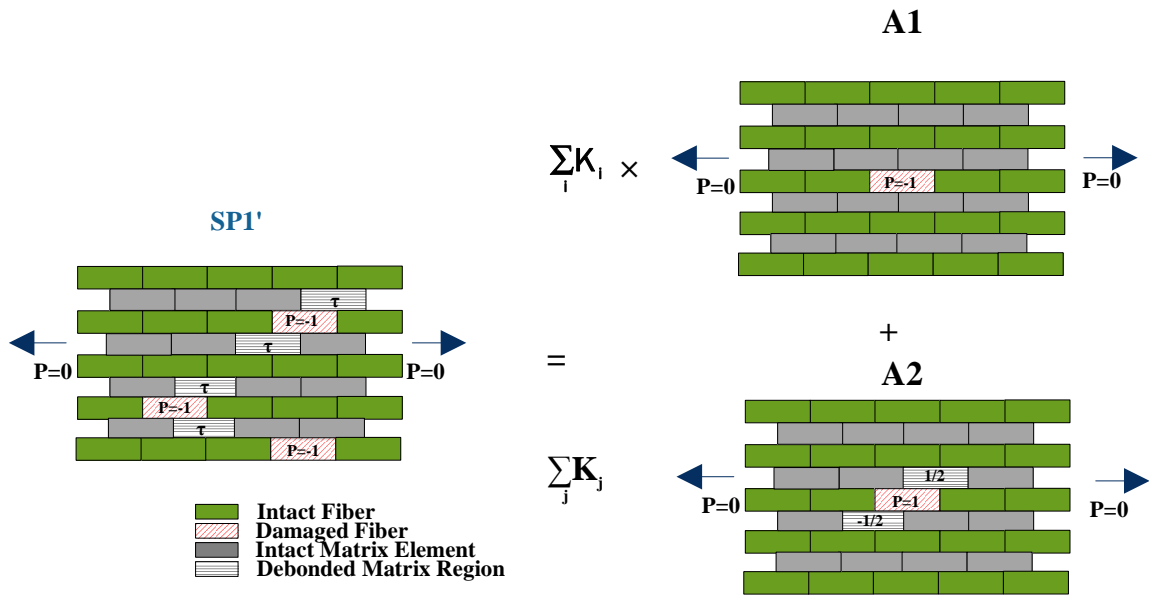


Figure 2.5: Superposition technique adopted in order to solve the problem SPI'

Auxiliary problem A2

In order to solve the Auxiliary problem A2, the equilibrium equations that were previously described need to be considered (see equations 2.1 to 2.16). Figure 2.6 presents a description to the auxiliary problem A2.

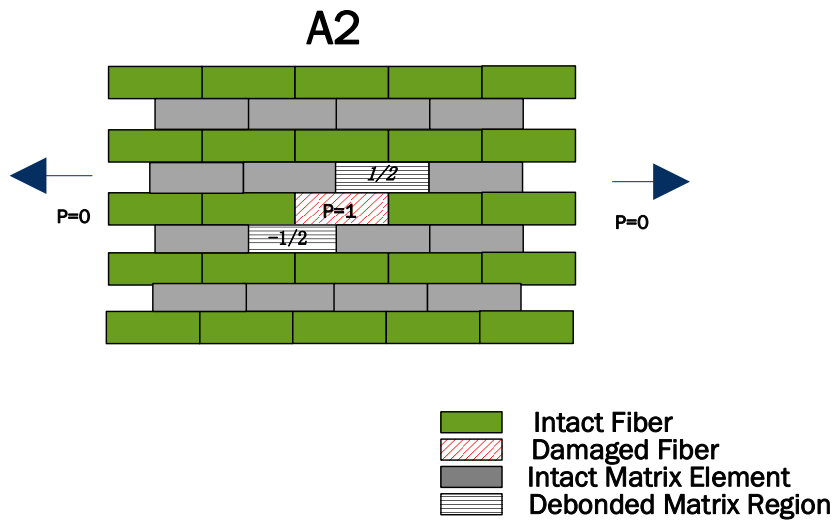


Figure 2.6: Auxiliary problem A2

The boundary conditions for the Auxiliary problem A2 are summarized below:

$$L_1^d(0^+, t) = \frac{\partial V_1^d(0^+, t)}{\partial \xi} = 1/2 \quad (2.71)$$

$$L_0^d(0^+, t) = \frac{\partial V_0^d(0^+, t)}{\partial \xi} = -1/2 \quad (2.72)$$

$$L_n^d(0^+, t) = \frac{\partial V_n^d(0^+, t)}{\partial \xi} = 0 \quad \forall n \geq 2, n \leq -1 \quad (2.73)$$

$$L_n^d(\infty, t) = \frac{\partial V_n^d(\infty, t)}{\partial \xi} = 0 \quad \forall n \quad (2.74)$$

Applying the Laplace transform to the equation (2.16) as well as for the boundary conditions in equations (2.71), (2.72), (2.73) and (2.74) leads to the following equations:

$$\frac{\partial^2 \underline{V}_n^d(\xi, s)}{\partial \xi^2} + s \underline{G}(s) \left(\underline{V}_{n+1}^d(\xi, s) - 2 \underline{V}_n^d(\xi, s) + \underline{V}_{n-1}^d(\xi, s) \right) = 0 \quad (2.75)$$

$$L_1^d(0^+, s) = \frac{\partial V_1^d(0^+, s)}{\partial \xi} = 1/2s \quad (2.76)$$

$$L_0^d(0^+, s) = \frac{\partial V_0^d(0^+, s)}{\partial \xi} = -1/2s \quad (2.77)$$

$$L_n^d(0^+, s) = \frac{\partial V_n^d(0^+, s)}{\partial \xi} = 0 \quad \forall n \geq 2, n \leq -1 \quad (2.78)$$

$$L_n^d(\infty, s) = \frac{\partial V_n^d(\infty, s)}{\partial \xi} = 0 \quad \forall n \quad (2.79)$$

If we define the auxiliary function: $V^d(\xi, s, \theta)$ by the following equation:

$$\underline{V}^d(\xi, s, \theta) = \frac{V_0^d}{\pi}(\xi, s) + \frac{2}{\pi} \sum_{n=1}^{\infty} \underline{V}_n^d(\xi, s) \cos(n\theta) \quad 0 < \theta < \pi \quad (2.80)$$

The equations (2.75) is transformed to equations (2.81)

$$\frac{\partial^2 \underline{V}^d(\xi, s, \theta)}{\partial \xi^2} - 4s \underline{G}(s) C_\theta^2 \underline{V}^d(\xi, s, \theta) = 0 \quad (2.81)$$

The boundary conditions are modified to be as per the equations (2.82) and (2.83)

$$\frac{\partial \underline{V}^d(0^+, s, \theta)}{\partial \xi} = \frac{1}{2s} \frac{e^{-i\theta} - 1}{\pi} \quad (2.82)$$

$$\frac{\partial V^d(\infty, s, \theta)}{\partial \xi} = 0 \quad (2.83)$$

where $C_\theta = \sin\left(\frac{\theta}{2}\right)$

If we suggest the following form of $\underline{V}^d(\xi, s, \theta)$:

$$\underline{V}^d(\xi, s, \theta) = f(s, \theta) \exp\left(-2C_\theta \xi \sqrt{s\underline{G}(s)}\right) \quad (2.84)$$

When replacing the equation (2.83) in the equation (2.81) we obtain:

$$\frac{\partial \underline{V}^d(\xi, s, \theta)}{\partial \xi} = f(s, \theta) \left(-2C_\theta \sqrt{s\underline{G}(s)}\right) \exp\left(-2C_\theta \xi \sqrt{s\underline{G}(s)}\right) \quad (2.85)$$

$$\frac{\partial \underline{V}^d(0^+, s, \theta)}{\partial \xi} = \frac{1}{2s} \frac{e^{-i\theta} - 1}{\pi} = -2C_\theta \sqrt{s\underline{G}(s)} f(s, \theta) \quad (2.86)$$

A form of $f(s, \theta)$ can therefore be suggested:

$$f(s, \theta) = -\frac{e^{-i\theta} - 1}{4s\pi C_\theta \sqrt{s\underline{G}(s)}} \quad (2.87)$$

This leads to:

$$\underline{V}^d(\xi, s, \theta) = -\frac{e^{-i\theta} - 1}{4s\pi C_\theta \sqrt{s\underline{G}(s)}} \exp\left(-2C_\theta \xi \sqrt{s\underline{G}(s)}\right) \quad (2.88)$$

$$\underline{V}_n^d(\xi, s, \theta) = \int_0^\pi \underline{V}^d(\xi, s, \theta) e^{in\theta} d\theta = \int_0^\pi \frac{e^{in\theta} - e^{i(n-1)\theta}}{4s\pi C_\theta \sqrt{s\underline{G}(s)}} \exp\left(-2C_\theta \xi \sqrt{s\underline{G}(s)}\right) d\theta \quad (2.89)$$

$$Re\left(\underline{V}_n^d(\xi, s, \theta)\right) = \int_0^\pi \frac{\cos(n\theta) - \cos((n-1)\theta)}{4s\pi C_\theta \sqrt{s\underline{G}(s)}} \exp\left(-2C_\theta \xi \sqrt{s\underline{G}(s)}\right) d\theta \quad (2.90)$$

Therefore:

$$\begin{aligned} & \underline{V}_n^d(\xi, s) \\ &= \int_0^\pi \frac{\cos(n\theta) - \cos((n-1)\theta)}{4s\pi C_\theta \sqrt{s\underline{G}(s)}} \exp\left(-2C_\theta \xi \sqrt{s\underline{G}(s)}\right) d\theta \end{aligned} \quad (2.91)$$

And the matrix's shear strain is obtained with the following equation:

$$\underline{\Gamma}_n^d(\xi, s) = \underline{V}_{n+1}^d(\xi, s) - \underline{V}_n^d(\xi, s) = - \int_0^\pi \frac{\cos(n\theta) C_\theta}{s\pi\sqrt{s\underline{G}(s)}} \exp\left(-2C_\theta\xi\sqrt{s\underline{G}(s)}\right) d\theta \quad (2.92)$$

The matrix's shear stress is related to the shear strain with equation (2.93)

$$\underline{T}_n^d(\xi, s) = \underline{\Gamma}_n^d(\xi, s) \times s\underline{G}(s) = \int_0^\pi \frac{\cos(n\theta) C_\theta \sqrt{s\underline{G}(s)}}{\pi s} \exp\left(-2C_\theta\xi\sqrt{s\underline{G}(s)}\right) d\theta \quad (2.93)$$

To obtain the solution in the time domain, we must perform the Laplace transform inverse.

The fiber's axial displacement is $V_n^d(\xi, t)$:

$$V_n^d(\xi, t) = \int_0^\pi \frac{\cos(n\theta) - \cos((n-1)\theta)}{4s\pi C_\theta} \times L^{-1} \left\{ \frac{\exp(-2C_\theta\xi\sqrt{s\underline{G}(s)})}{s\sqrt{s\underline{G}(s)}} \right\} d\theta \quad (2.94)$$

Having the expression of the fiber's axial displacement we can obtain the expression of the fiber's axial load by deriving equation (2.94)

$$\begin{aligned} L_n^d(\xi, t) &= \frac{\partial V_n^d(\xi, t)}{\partial \xi} \\ &= - \int_0^\pi \frac{\cos(n\theta) - \cos((n-1)\theta)}{2\pi} \times L^{-1} \left\{ \frac{\exp(-2C_\theta\xi\sqrt{s\underline{G}(s)})}{s} \right\} d\theta \end{aligned} \quad (2.95)$$

The matrix's shear strain is also deducted from the fiber axial displacement.

$$T_n^d(\xi, t) = - \int_0^\pi \frac{\cos(n\theta)C_\theta}{\pi} \times L^{-1} \left\{ \frac{\sqrt{s\underline{G}(s)} \times \exp(-2C_\theta\xi\sqrt{s\underline{G}(s)})}{s} \right\} d\theta \quad (2.96)$$

Using Schapery's direct inversion technique with $v(t) = sv(s)|_{s=\exp(-\gamma E)/t}$

In the Laplace domain, matrix's creep and relaxation functions are related through:

$$s\underline{G}(s) = \frac{1}{s\underline{J}(s)} = \frac{s^\alpha}{\Gamma(1+\alpha)} \quad (2.97)$$

The solutions the Auxiliary problem A2 in the time domain is given by the equations (2.98) to (2.101):

$$V_n^d(\xi, t) = \frac{t^{\alpha/2}}{\beta_s} \times \int_0^\pi \frac{\cos(n\theta) - \cos((n-1)\theta)}{4\pi C_\theta} \exp(-2C_\theta z \beta_s) \times d\theta \quad (2.98)$$

$$L_n^d(\xi, t) = - \int_0^\pi \frac{\cos(n\theta) - \cos((n-1)\theta)}{2\pi} \exp(-2C_\theta z \beta_s) \times d\theta \quad (2.99)$$

$$\Gamma_n^d(\xi, t) = - \frac{t^{\alpha/2}}{\beta_s} \times \int_0^\pi \frac{\cos(n\theta) C_\theta}{\pi} \exp(-2C_\theta z \beta_s) \times d\theta \quad (2.100)$$

$$T_n^d(\xi, t) = - \frac{\beta_s}{t^{\alpha/2}} \times \int_0^\pi \frac{\cos(n\theta) C_\theta}{\pi} \exp(-2C_\theta z \beta_s) \times d\theta \quad (2.101)$$

With $\beta_s = \sqrt{\frac{\exp(-\alpha\gamma)}{\Gamma(1+\alpha)}}$ and $z = \frac{\xi}{t^{\alpha/2}}$

Solution of problem P1'

In order to obtain the solution of the subproblem SP1' one must calculate the superposition weight functions $K_{ij}^b(t)$ and $K_{ij}^d(t)$. The weight functions ($K_{ij}^b(t)$ and ($K_{ij}^d(t)$) denotes the influence of the breakage (debonding) of fiber (matrix) i at point ξ_i to a fiber (matrix) j at point ξ_j . To determine the weight functions $K_{ij}^b(t)$ and $K_{ij}^d(t)$, the following system of equations needs to be solved:

$$\begin{bmatrix} K_{ij}^b(t) \\ K_{ij}^d(t) \end{bmatrix} = \begin{bmatrix} \Lambda_{ij}(t) & \varphi_{ij}(t) \\ \Omega_{ij}(t) & \psi_{ij}(t) \end{bmatrix}^{-1} \begin{bmatrix} -1 \\ \tau_{fr}(t)\Delta x \end{bmatrix} \quad (2.102)$$

where $\Lambda_{ij} = L_{n_i-n_j}^b(\xi_i - \xi_j, t)$ and $\varphi_{ij} = L_{n_i-n_j}^d(\xi_i - \xi_j, t)$ are the axial load transmission factors due to fiber breakage and fiber-matrix debonding respectively, $\Omega_{ij} = \Delta x T_{n_i-n_j}^b(\xi_i - \xi_j, t)$ and $\psi_{ij} = \Delta x \times T_{n_i-n_j}^d(\xi_i - \xi_j, t) + I_{n_i-n_j}(\xi_i - \xi_j, t)$ are the shear force transmission factors due to fiber breakage and fiber-matrix debonding respectively. $\tau_{fr}(t)$ is the imposed shear stress at the debonded regions that will be introduced in the next paragraph. Δx is the spatial discretization of the specimen.

When obtaining the weight functions, the solution of the subproblem SP1' can be obtained with the following expressions:

$$L_n(\xi, t) = \sum_{J=1}^{nb} L_{n-n_j}^b(\xi - \xi_j, t) K_j^b(t) + \sum_{J=nb+1}^{nb+nd} L_{n-n_j}^d(\xi - \xi_j, t) K_j^d(t) \quad (2.103)$$

$$V_n(\xi, t) = \sum_{J=1}^{nb} V_{n-n_j}^b(\xi - \xi_j, t) K_j^b(t) + \sum_{J=nb+1}^{nb+nd} V_{n-n_j}^d(\xi - \xi_j, t) K_j^d(t) \quad (2.104)$$

$$\Gamma_n(\xi, t) = \sum_{J=1}^{nb} \Gamma_{n-n_j}^b(\xi - \xi_j, t) K_j^b(t) + \sum_{J=nb+1}^{nb+nd} \Gamma_{n-n_j}^d(\xi - \xi_j, t) K_j^d(t) \quad (2.105)$$

$$T_n(\xi, t) = \sum_{J=1}^{nb} T_{n-n_j}^b(\xi - \xi_j, t) K_j^b(t) + \sum_{J=nb+1}^{nb+nd} T_{n-n_j}^d(\xi - \xi_j, t) K_j^d(t) \\ + \sum_{J=nb+1}^{nb+nd} \frac{I_{n-n_j}(\xi - \xi_j, t)}{\Delta x} K_j^d(t) \quad (2.106)$$

where V_n is the fiber axial displacement, L_n is the fiber axial load, $\Gamma_n(\xi, t)$ is the matrix shear strain, $T_n(\xi, t)$ is the matrix shear stress, nb is the number of fiber breaks and nd is the number of debonded matrix elements.

The solution of the general problem P1' can be written with equations (2.107) and (2.108). We note that matrix shear stress and strain remain unchanged.

$$P_n(\xi, t) = L_n(\xi, t) + 1 \quad \text{The fiber's axial stress} \quad (2.107)$$

$$U_n(\xi, t) = V_n(\xi, t) + \xi \quad \text{The fiber's axial displacement} \quad (2.108)$$

Fiber/matrix debonding criterion

When an initially undamaged UD composite is subjected to sustained far field axial stress, fiber breaks occur. Around these fiber breaks matrix is subjected to shear. As matrix shear stress relaxes in time, the corresponding shear strain increases. In the present model, when this shear strain reaches a limit value γ_{lim} (Fiedler et al. [2001]), constant in time, debonding occurs. When debonding occurs in a matrix element, the shear stress is limited by τ_{fr} (see Figure 2.6a). A coulomb-type law is proposed and verified experimentally in the work of Koyanagi et al. [2007].

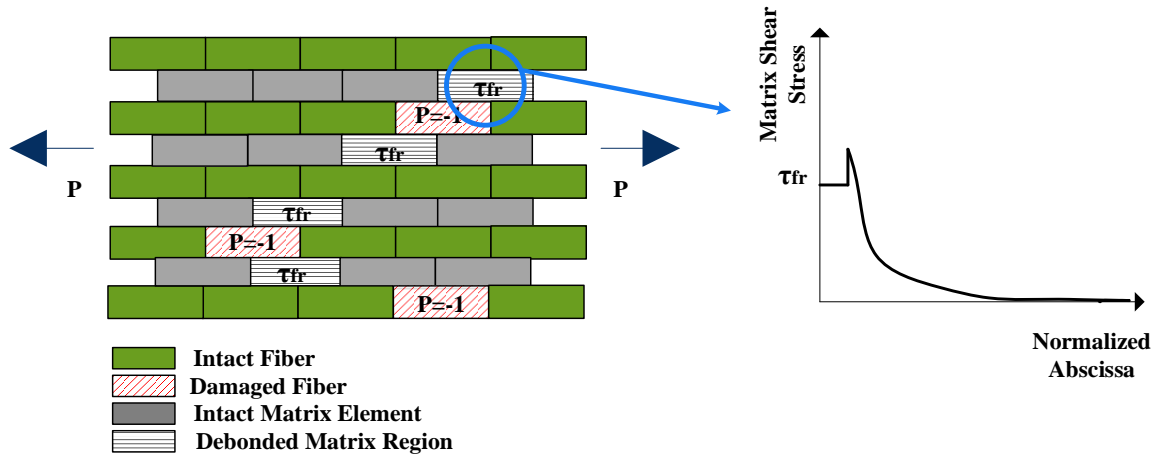


Figure 2.6a: Fiber/matrix debonding

Following Koyanagi et al. [2007], a frictional coefficient μ links the radial compressive stress σ_r and the frictional stress in the debonded region as follows:

$$\tau_{fr}(t) = \mu \sigma_r(t) \quad (2.109)$$

Since we consider that the specimen will not deform in the perpendicular direction to the applied stress, the radial deformation ε_r is null at the far field

$$\varepsilon_r = 0 \quad (2.110)$$

$$\varepsilon_r = \frac{\sigma_r}{E_m} - \frac{\nu}{E_m} \sigma_m = 0 \quad (2.111)$$

where E_m is the matrix Young's modulus, ν is the matrix Poisson's ratio, σ_m is the matrix's far field longitudinal stress and σ_r is the matrix's radial compressive stress

The radial compressive stress is related to the matrix's far field longitudinal stress σ_m by the following equation:

$$\sigma_r(t) = \nu \sigma_m(t) \quad (2.112)$$

Since the fibers and the matrix have the same axial strain ε at the far field

$$\sigma_m(t) = E_m(t) \varepsilon \quad (2.113)$$

$$\varepsilon = \frac{\sigma_f}{E_f} \quad (2.114)$$

A power law will be used for matrix's axial viscoelastic behavior:

$$E_m(t) = \frac{E_{0m}}{(t/T_c)^\alpha} \quad (2.115)$$

When combining equations (2.109) to (2.115) we obtain the equation (2.116) which will represent the residual shear stress at the fiber/matrix debonded regions:

$$\tau_{fr}(t) = \mu\nu \frac{\sigma_f}{E_f} \frac{E_{0m}}{(t/T_c)^\alpha} \quad (2.116)$$

2.2.4 Computer simulations

A tension load is applied to the extreme fiber bay and the evolution of fiber stresses around arbitrary array of fiber breaks is calculated. Each fiber element is assigned a strength value from a Weibull probability distribution. The well-known Weibull's [1951] distribution is the most widely used for the evaluation of the statistical distribution of fiber strengths. For the probability of failure of a chain consisting of n links $P(\sigma)$, Weibull [1951] proposed the following equation:

$$P(\sigma) = 1 - \exp(-n \varphi(\sigma)) \quad (2.117)$$

The function $\varphi(\sigma)$ is positive and none decreasing.

In his study, Weibull [1951] approximated the function $\varphi(\sigma)$ with:

$$\varphi(\sigma) = \left[- \left(\frac{\sigma - \sigma_l}{\sigma_a} \right) \right]^\beta \quad (2.118)$$

The parameters σ_l , σ_a and β are the location, scale and shape parameters, respectively.

Weibull's [1951] theory was based on the weakest link hypothesis, i.e. the specimen fails, if its weakest volume element fails. Using some empirical arguments necessary to obtain a simple and good fitting to his experimental data, he derived the so-called Weibull distribution function:

$$P(\sigma) = 1 - \exp\left(-\frac{V}{V_0} \left(\frac{\sigma}{\sigma_0}\right)^m\right) \quad (2.119)$$

The Weibull modulus m is a measure for the scatter of strength data: the wider the distribution is the smaller m is. σ_0 is the characteristic strength value and V_0 is the chosen normalizing volume. V represents the volume of the specimen and σ is the stress state.

The utility of the Weibull distribution has been traditionally justified by its capability to fit a wide range of failure data. The theoretical justification of the Weibull distribution is the extreme value theory performed by Ullmann et al.[1958]. However, several experimental studies showed the limitations for the use of Weibull distribution to model flaws and defects. Bonora [2000] experimental work showed that the Weibull modulus m depends on the specimen geometry (the notch radius). This was also confirmed by experiments involving failure of notched ceramic specimens conducted by Gerguri et al.[2004]. Moreover, Danzer et al.[2007] demonstrated in their study that the Weibull distribution is not an appropriate model for brittle materials containing bi-or multi-modal flaw size distributions or materials having a high defect density. In addition, the authors noted that published data, claimed to be Weibull distributed, that are based on small samples may not necessarily come from a Weibull population. Todinov [2009] reported that the Weibull distribution is incapable of correctly predicting the probability of failure in the simple cases of identical flaws; two flaw size groups, each of which contains identical flaws; failure controlled by the orientation of two different types of flaws; and also beyond a stress level where no new critical flaws are created by increasing the applied stress. Based on experimental results, the author also concluded that in the case of non-interacting flaws that are randomly distributed in a stressed volume, the Weibull distribution predicts correctly the probability of failure if and only if the stress dependence of the probability that a flaw will be critical is a power law or can be approximated well by a power law. An equation (Eq. 2.120) that does not require any assumptions concerning the physical nature of the flaws and the physical mechanism of failure and can be applied in any situation of a locally initiated failure by non-interacting entities was suggested by Todinov [2009].

$$P(\sigma) = 1 - \exp(-\bar{\lambda}VF_c(\sigma)) \quad (2.120)$$

Equation 2.120 is applicable for non-interacting flaws characterized by a strength distribution $F_c(\sigma)$, whose locations in a volume V follow a Poisson process with average number density $\bar{\lambda}$.

The work of Lamon et al. [1997] showed that the distributions of failure data including strains-to-failure or strength for SiC fibers may not be described solely in terms of the two-parameter Weibull function, owing to the presence of bimodal populations of fracture-inducing flaws. The authors attributed this effect to the presence of two partially concurrent flaw populations

including extrinsic flaws located in the surface and intrinsic flaws located both in the surface and in the volume.

According to Lamon et al. [1997] , in the presence of concurrent surface- and volume-located flaw populations, the failure probability function can be written with:

$$P(\sigma) = 1 - \exp\left[-V_E \left(\frac{\sigma_{max}}{\sigma_{0V}}\right)^{m_V} - S_E \left(\frac{\sigma_{max}}{\sigma_{0S}}\right)^{m_S}\right] \quad (2.121)$$

where σ_{0S} and m_S are the statistical parameters for surface-located failure origins. S_E is the effective surface. S_E coincides with the fiber external surface in the presence of a uniform stress state. σ_{0V} and m_V are the statistical parameters for volume-located failure origins. V_E is the equivalent volume. However, the author noted that it is more appropriate to consider a bimodal partially concurrent populations that include one family of flaws pre-existing within all the samples (intrinsic flaws), whereas flaws of the second family are present only within certain specimens (extrinsic flaws). The failure probability function can be written with:

$$P(\sigma) = 1 - (1 - \pi_2) \exp\left[-V_{E1} \left(\frac{\sigma_{max}}{\sigma_{01}}\right)^{m_1}\right] - \pi_2 \exp\left[-V_{E1} \left(\frac{\sigma_{max}}{\sigma_{01}}\right)^{m_1} - V_{E2} \left(\frac{\sigma}{\sigma_{02}}\right)^{m_2}\right] \quad (2.122)$$

where V_{E1} and V_{E2} are the effective volumes respective to intrinsic and extrinsic flaws and π_2 is the fraction of specimen containing the extrinsic flaws.

In addition to what was said, several experimental works showed that for the glass fibers, three flaws categories control the fiber rupture for various specimen lengths. The first category is the surface flaws that are induced by fabrication and handling. This type of flaws is distant about 2cm and control the fibers strength at low range of applied stress. The second category consists of the moderate surface flaws that are usually due to fabrication imperfections and corrosion. They are distant of approximately 0.1 mm and control fiber strength at medium range of applied stress. The third category is the internal structural defects of glass causing local stress concentration. These flaws are usually distant of 0.01 to 0.001 mm and control the fiber strength at high ranges of applied stress. As for the Carbone fibers, multiple studies considered Unimodal Weibull laws for the modeling of flaws (Blassiau et al. [2007], Peterlik and Loidl [2001], Thomas et al. [2011]). However, in the work Loidl et al. [2007], tension tests were performed to unidirectional composites reinforced with carbon fibers. The authors concluded that bimodal Weibull laws describe accurately the distribution of the fracture strength for carbon fibers. According to Loidl et al. [2007], (σ_{01}, m_1) are responsible for the failure due to

'intrinsic defects' and (σ_{02}, m_2) are responsible for the failure due to 'extrinsic defects'. The authors also observed that the bimodality increases with the length of the tested fiber.

In this research work, and as per Zinck [2011], when the behavior of GFRPs is analyzed, each fiber element is assigned a strength value from a bimodal Weibull probability distribution (equation 2.123).

$$P(\sigma) = 1 - q \exp\left(-\left(\frac{\sigma}{\sigma_{01}}\right)^{m_1}\right) + (1 - q) \exp\left(-\left(\frac{\sigma}{\sigma_{02}}\right)^{m_2}\right) \quad (2.123)$$

where $P(\sigma)$ is the probability of an element to break at the stress is level σ and q is the weight of each failure mode or category of flaw. In order to take into account the variation of the parameter q with respect to the element length, Zinck [2011] proposed a linear form:

$$q = q_0 \frac{l}{l_0} \quad (2.124)$$

where l_0 is the characteristic gauge length and l is the element length which is equal to the spatial discretization Δx . σ_{01}, σ_{02} are the scale parameters, m_1, m_2 are the shape parameters and q_0 is a parameter determined experimentally. As per the work of Baxevanakis et al. [1998], when analyzing the behavior of CFRPs in this current thesis, each fiber element is assigned a strength value from a unimodal Weibull probability distribution (equation 2.125).

$$P(\sigma) = 1 - \exp\left[-\left(\frac{\sigma}{\sigma_0}\right)^m\right] \quad (2.125)$$

The parameters m and σ_0 are extracted from the study of Baxevanakis et al. [1998] on T300 carbon fibers. Figure 2.7 gives example on the fiber strength distribution for a generated specimen reinforced with glass fiber.

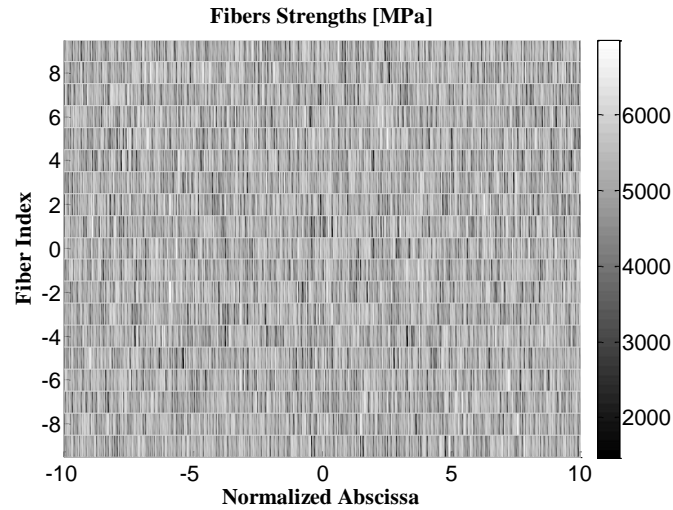


Figure 2.7: Fibers strengths for a given specimen composed by 19 fibers

Using the shear lag equations we can estimate the stress in each fiber element. At time t , the axial stress at each fiber element is examined and compared to the stochastic resistance determined as previously described. If the resistance is smaller than the axial stress then the fiber is considered as broken and a shear stress is imposed to the adjacent matrix elements in order to equilibrate the axial stress drop. In this way, the load carried before by the broken fiber element is transferred to the adjacent intact fibers. This is an iterative process until the final stress distribution in the whole specimen at time t is calculated. Then a new time increment is made $t' = t + \Delta t$ and the same procedure is followed. The procedure is summarized in Figure.2.7a

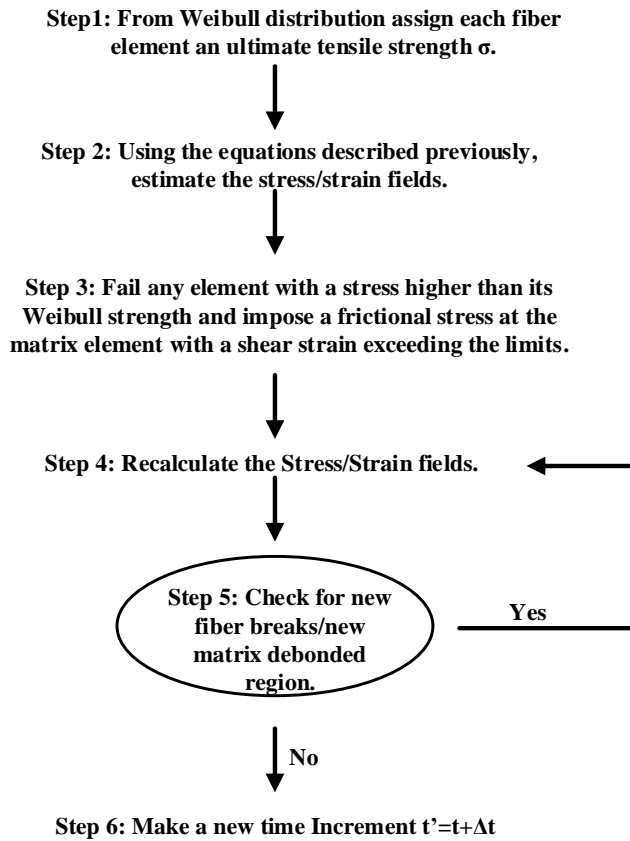


Figure 2.7a: Calculation algorithm (shear-lag method)

For static tests, where we want to calculate the ultimate tensile strength of the specimens, the load is incremented ($P' = P + \Delta P$) and no viscous effects are considered for the matrix. For creep tests, the applied load at the extremity of the specimen (far field) is constant in time and the behavior of the matrix is viscous.

2.2.5 Parameters of interest

The average axial deformation $\varepsilon(t)$ and the apparent elastic modulus of the composite $E_{app}(t)$ are monitored during the numerical analysis.

In the case of a unidirectional composite material subjected to tension load at the extremities, the average stress in the specimen σ_a can be described by the following equation:

$$\sigma_a = V_f \sigma_f + V_m \sigma_m \approx V_f \sigma_f \quad (2.126)$$

V_f is the fiber volume fraction and V_m is the matrix volume fraction. The contribution of the matrix axial stress is neglected in the shear lag model as it is several orders of magnitudes lower given the important contrast of the Young modulus between the fibers and matrix.

Therefore, the apparent modulus expression can be written with:

$$E_{app}(t) = V_f \frac{\sigma_{\infty}}{\varepsilon(t)} \quad (2.127)$$

The average longitudinal deformation can also be written with:

$$\varepsilon(t) = \frac{U_{mean}\left(\frac{L}{2}\right) - U_{mean}\left(-\frac{L}{2}\right)}{L} \quad (2.128)$$

where σ_{∞} is the average stress at fibers end. $U_{mean}\left(\frac{L}{2}\right)$; $U_{mean}\left(-\frac{L}{2}\right)$ are the average displacements at fibers end; and L is the length of the specimen.

2.2.6 Parametric analysis and validation

A parametric analysis is necessary in order to obtain the adequate dimensions of the specimen considered in the calculations as well as to verify some of the assumptions taken in the model. In this section, we also introduce the periodicity effect that was neglected in the model proposed by Beyerlein et al. [1998]. The parameters of interest in this analysis are the mesh size Δx , the time interval Δt , the number of fibers, and the length of the specimen.

2.2.6.1 Periodicity effect and boundary conditions

In the model presented by Beyerlein et al. [1998] boundary conditions were applied at the tip of each fiber. However, the fiber located at the upper (or lower) edge of the specimen did not have any neighbor above (or below) of it. This creates an unphysical boundary layer, which can be avoided by considering periodic boundary conditions (see Figure 2.8). The study of Cox [1952] showed that a fiber break overstress practically only the first two or three adjacent fibers. In accordance to Cox [1952], Figure 2.9 shows the calculated (by solving Eq. 2.107) overstress diagrams induced by the rupture of a central fiber on its intact neighboring fibers. It is worth mentioning that the overstress factor for the first intact fiber is equal to 1.33 and it is reduced to 1.016 at the intact fiber number 4. Inspired by this fact, fictitious specimens are generated near the upper and lower edge of the specimen at hand. The fictitious specimens interact with only three fibers of the lower and upper edge. In this way the repetition of the considered specimen in the vertical direction is simulated.

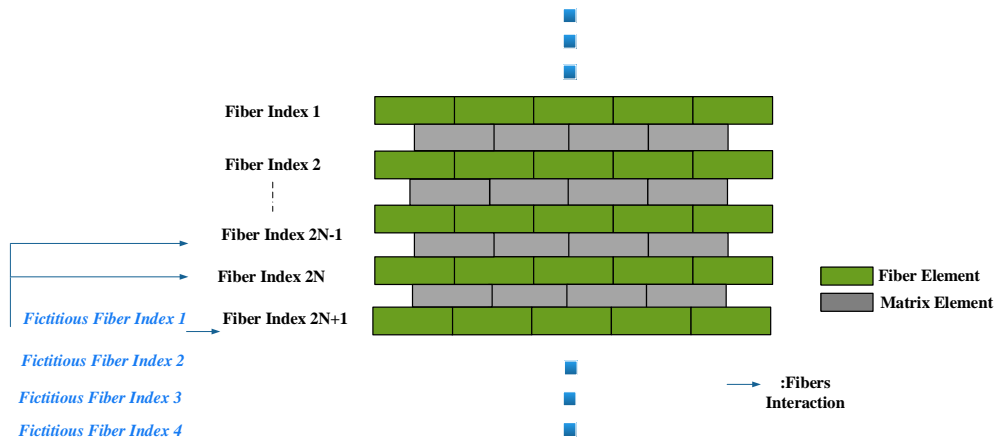
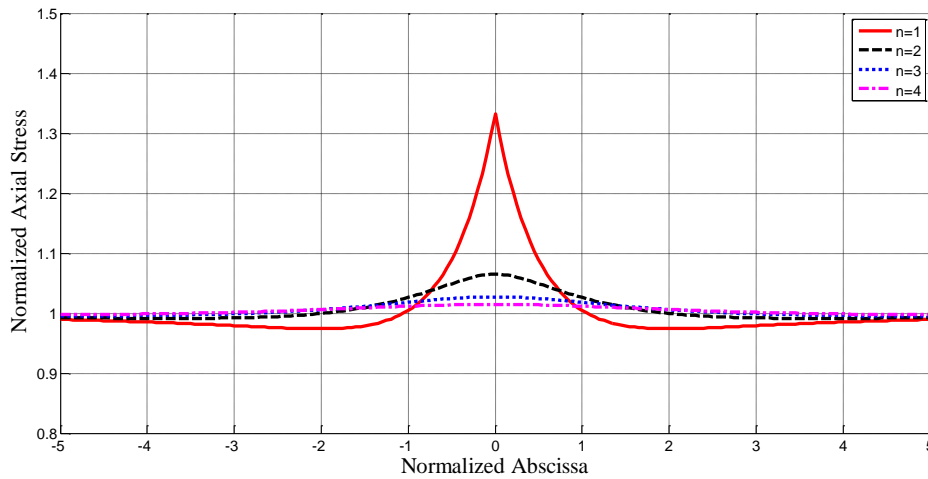


Figure 2.8: Periodicity effect



Intact Fiber's Number	1	2	3	4
Overstress Factor	1.33	1.067	1.029	1.016

Figure 2.9: Normalized axial stress in the neighboring intact fibers due to the fiber breakage of fiber $n=0$. The first 8 ($4+4$) neighboring fibers take almost the total load (88%) of the broken fiber.

The effect of the periodic boundary conditions on the fibers axial stress state is illustrated in Figure 2.10. In these simulations, the position of the fiber break sites are imposed (rectangles perpendicular to the load direction located at the middle of the specimen). The developed fiber axial stresses were calculated using the shear-lag model. Notice that if periodic boundary conditions are not used, the stresses at the upper/lower fibers are not uniform which is not physical.

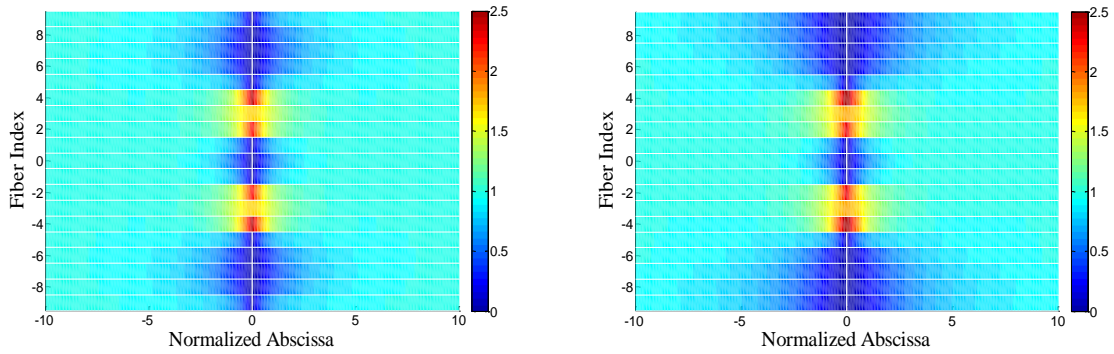


Figure 2.10: Normalized fiber axial stress (a): without periodic boundary conditions; (b): with periodic boundary conditions

2.2.6.2 Effect of the time increment Δt

When creep tests are performed using the shear lag theory, time intervals including specific discretized time values need to be incorporated to the model. A logarithmic scale in the time interval was adopted in such a way that a constant variation of the matrix creep compliance J between two time steps is obtained. Using Eq. 2.5 and the numerical values of α and T_c , the initial and final values of $J(t)$ can be determined. The range of the matrix compliance J is then divided by the number of the time steps and time points corresponding to each dJ step are calculated by inverting Eq. 2.5. A parametric analysis was conducted in order to obtain the minimum value for the assumed number of time steps.

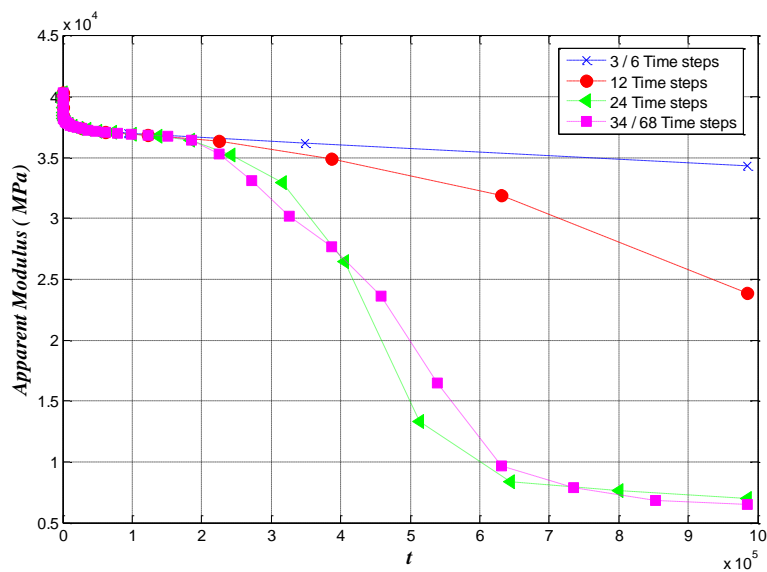


Figure 2.11: Time discretization effect. Average apparent modulus versus normalized time

Figure 2.11 shows the evolution of the apparent modulus (Eq. 2.127) with the normalized time in a creep test for various values of the number of time steps (the total time is constant). Convergence is assured for 24 time steps.

2.2.6.3 Effect of the spatial discretization of the composite Δx

Several simulations are conducted in order to verify the adequate mesh size Δx . The evolution of the apparent modulus (Eq. 2.127) values with the normalized time for various mesh sizes for a creep test are shown in Figure 2.12. For the parameters used, convergence is reported for a Δx equal to 0.025 which is much smaller than the one recommended by Beyerlein et al. [1998] ($\Delta x = 0.1$).

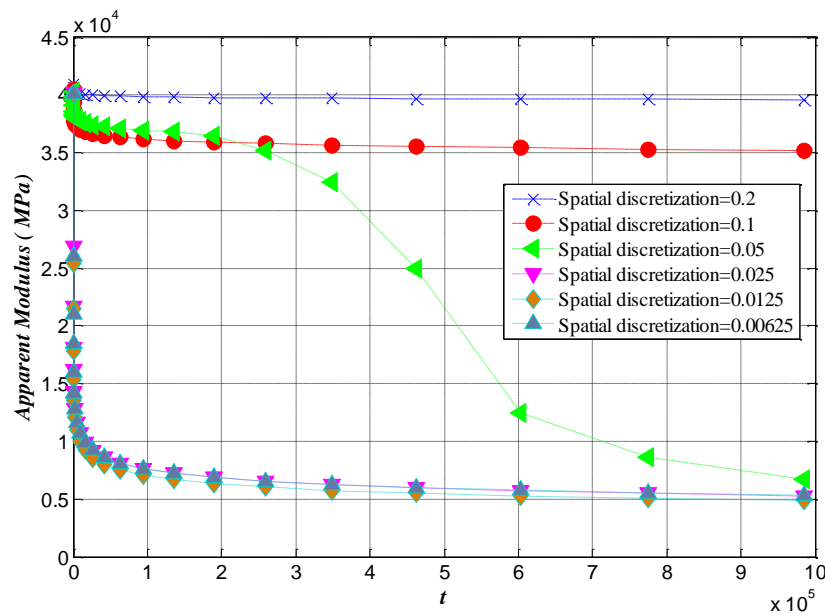


Figure 2.12: Effect of the spatial discretization Δx . Apparent modulus versus normalized time

2.2.6.4 Effect of the total number of fibers

In the search of the representative volume element, the minimum value of number of fibers considered in the discretization of the specimen is important. We note that in all simulations the fiber volume fraction V_f is kept constant. Figure 2.13 shows that the apparent modulus values (Eq. 2.127) for a creep test converge for a specimen that contains a minimum number of fibers equal to 19.

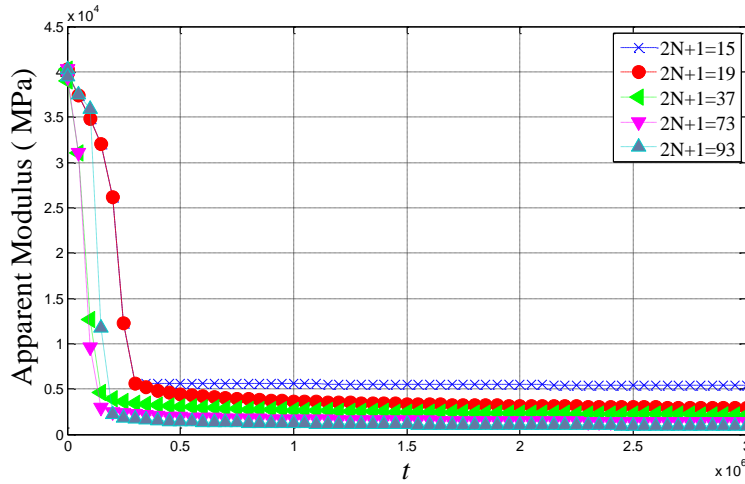


Figure 2.13: Effect of fibers number. Apparent modulus versus normalized time

2.2.6.5 Effect of the specimen's length

The minimum number of fibers in the discretization as well as the mesh size and the number of time steps for creep test was determined in the previous paragraphs. The minimum length of the specimen is also to be specified. In order to take into account the randomness of the fibers resistance, MonteCarlo simulation was performed and 50 specimens of different random sequence of fiber strength were modeled. For each length value, 50 specimens were considered and the following curves are obtained by calculating average values of apparent modulus for each specimen. The length of the specimen is $L = (2M + 1)\Delta x$. Determining the minimum value of length will allow the reduction of the size of the specimen and consequently of the calculation cost. Figure 2.14 shows that convergence as for it concern the average apparent modulus (Eq. 2.127) versus the normalized time for a creep test is obtained for $2M + 1 = 201$, corresponding to a length of 0.37 mm.

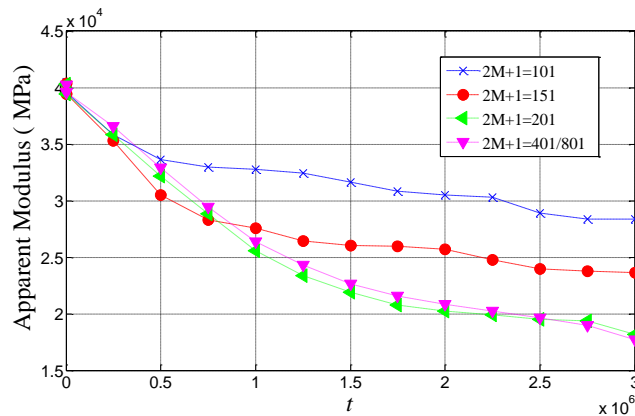


Figure 2.14: Length effect. Average apparent modulus versus normalized time

Table 2.1 shows the average values and the standard deviation values for the apparent modulus at the final time step for different specimen length.

Specimen Length (mm)	0.186	0.278	0.370	0.738	1.470
Average value for apparent modulus (MPa)	28,760	24,356	18,514	18,130	18,130
Standard deviation for apparent modulus (MPa)	16,191	17,176	16,614	13,125	13,125

Table 2.1: Average values and standard deviation values for the apparent modulus at the final time step

2.3 Finite Element Analysis

In this part of the study, a Finite Element model is developed in order to simulate the progressive damage of unidirectional composite materials. The main objective of this analysis is to compare the response of the composite determined according to shear-lag theory with the Finite Element method. Although the two modeling strategies are different, the same main modeling assumptions are taken into account in the finite element analysis regarding the mechanical behavior of the composite. In other words, the analysis is two dimensional (Plane Stress); the fiber's strength follows the Weibull distribution presented in section 2.2.4. The fibers are modeled as rod elements. In the Finite Element model the matrix is modeled as a 2D membrane element whose properties are such to transfer the shear stresses in the same way as in the shear lag model. Therefore a linear Drucker-Prager model with associated flow rule was considered for the matrix elements when static tests were performed. The parameter μ of the Drucker-Prager model was considered equal to 0.5 in the same manner as in the shear-lag model (see debonding criterion in section 2.2.3). The tensile and shear data for the matrix elements are based on the same experimental data as considered in the shear-lag model (Fiedler et al. [2001]). When creep tests were performed, the viscoelastic behavior of the matrix was considered in the same manner as in the shear-lag model. Figure 2.15 gives clear description on the Finite Element model. The software Abaqus is used for Finite Element simulations. Periodic boundary conditions were used in the same way as in the shear lag approach. However, the analysis can be either displacement or stress controlled, contrary to the previous shear lag model where only stresses could be applied to the extreme fiber row.

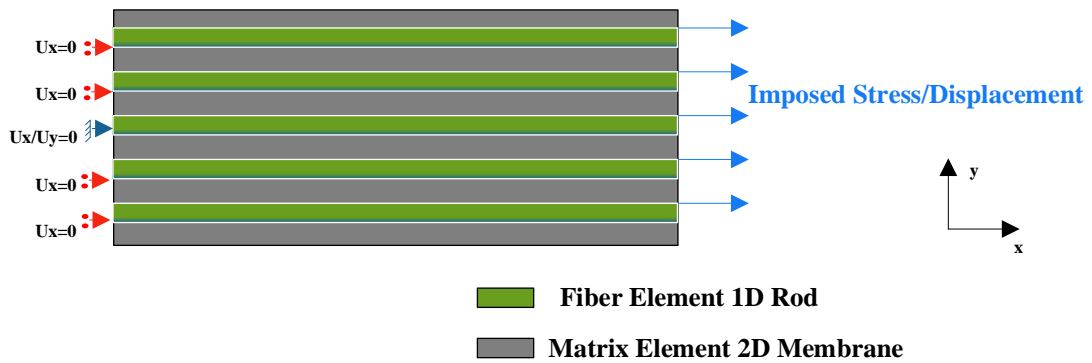


Figure 2.15: Finite Element model description

In principle both modeling strategies should give the same results as the underlying mechanical problem is the same. This is the target of the Finite Element model, i.e. to validate the shear-lag approach. For static tests, where we want to calculate the ultimate tensile strength of the specimens, the load/displacement is incremented ($P' = P + \Delta P / U' = U + \Delta U$) and no viscous effects are considered for the matrix. For creep tests, the applied load at the extremity of the specimen (far field) is constant in time and the behavior of the matrix is viscous.

Simulation procedure

A tension load or a displacement is applied at the extreme fiber row and the instantaneous response as well as the long term response of the specimen is monitored. Each fiber element is assigned a strength value from a Weibull probability distribution as previously described. The same geometry discretization considered in the shear lag model was also adopted in the finite element model. The fiber elements of the discretization whose ultimate tensile strength is exceeded are assigned a very small, negligible value for the Young modulus compared to the intact fiber. In this way, after a fiber break, the load is redistributed via matrix elements to the adjacent intact fibers. The matrix elements elastoplastic behavior simulates the fiber/matrix debonding. This process is repeated until the number of fiber breaks stabilizes in the same way as in the shear lag model. As soon as the number of fiber breaks stabilizes, the time marches forward $t' \rightarrow t + \Delta t$ for creep test (i.e. $U' \rightarrow U + \Delta U$ for strain controlled test, or $P' \rightarrow P + \Delta P$ for a load controlled test). The main algorithm of the tests is summarized in Figure 2.16:

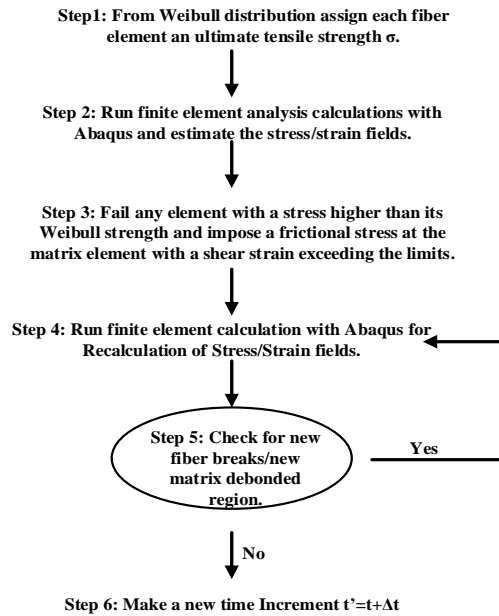


Figure 2.16: Calculation algorithm in the Finite Element model

2.4 Comparison of shear-lag and Finite Element modeling results

2.4.1 Ultimate tensile strength

In this section we estimate the ultimate tensile strength of one generated specimen of a GFRP with both modeling strategies. This will allow to juxtapose the results and to validate the approaches. The representative volume element considered consists of 19 fibers; each fiber is divided into 201 elements, the total length of the specimen is 0.37 mm (See Section 2.2.6). A random strength is generated to each fiber according to Weibull bimodal law (Eq. 2.123). An incremental stress load is applied at the tip of the fibers located on the right edge of the specimen (Figure 2.15). The response of the specimen is monitored with the increasing load. The aim of this analysis is to compare the two models for one specimen i.e. compare fiber breaks, stresses, strains etc. First we consider a simple case analysis where the position of the fiber break site is imposed. In the simple case study, overstress factors induced by the break site to the neighboring intact fibers are estimated with the developed shear-lag model and with the Finite Element model. A Comparison with the results proposed by Beyerlein et al. [1998] is also presented. Moreover, the matrix shear stresses around the break site are estimated. The simulation parameters are summarized in Table 2.2. Fiber and matrix characteristics are described as well as representative volume element (RVE) parameters.

RVE characteristics		Fiber characteristics Glass fiber		Matrix characteristics	
2N + 1(Total number of fibers)	19	σ_{01} (MPa)	3200	G_e (MPa)	1900
Length of the specimen(mm)	0.37	σ_{02} (MPa)	5110	α	0.2
Δx	0.025	m_1	5.79	γ_{lim}	6%
V_f %	54.5	m_2	7.65	T_c (s)	1600
Load increment ΔP (MPa)	50	E_f (MPa)	74000		
		r_f (μm)	13.5		

Table 2.2: Simulation parameters for P122 glass fibers. Zinck [2011]

Simple case study (isolated fiber break)

In this part of the study, we impose the position of the fiber break site at the center of the specimen. The objective of this analysis is to calculate the overstress factors induced by the breakage of a central fiber to its neighboring intact fibers. A comparison between shear-lag and Finite Element models is presented. Figure 2.17 describes the current problem at hand; the fiber break site is indicated by a small rectangle in grey. It is worth mentioning that in order to do a comparison with the Beyerlein et al. [1998] work, fiber/matrix debonding was neglected at first since this phenomena was not modeled by Beyerlein et al. [1998].

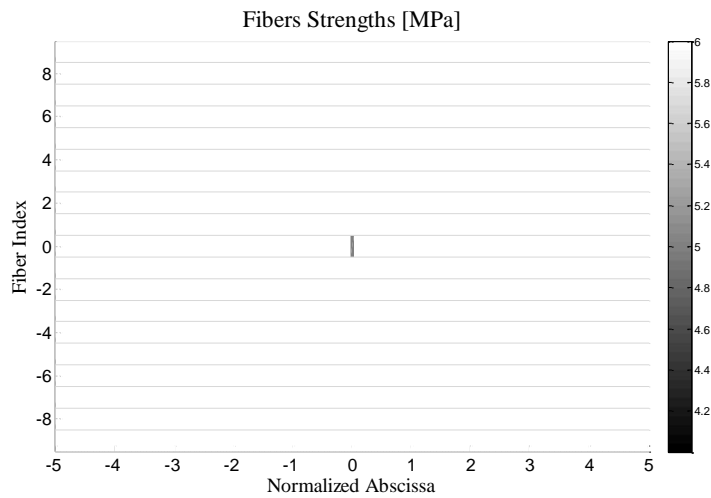


Figure 2.17: Position of the imposed defect/fiber break

Figure 2.18 shows the normalized fiber stresses around the break site calculated with the shear-lag method.

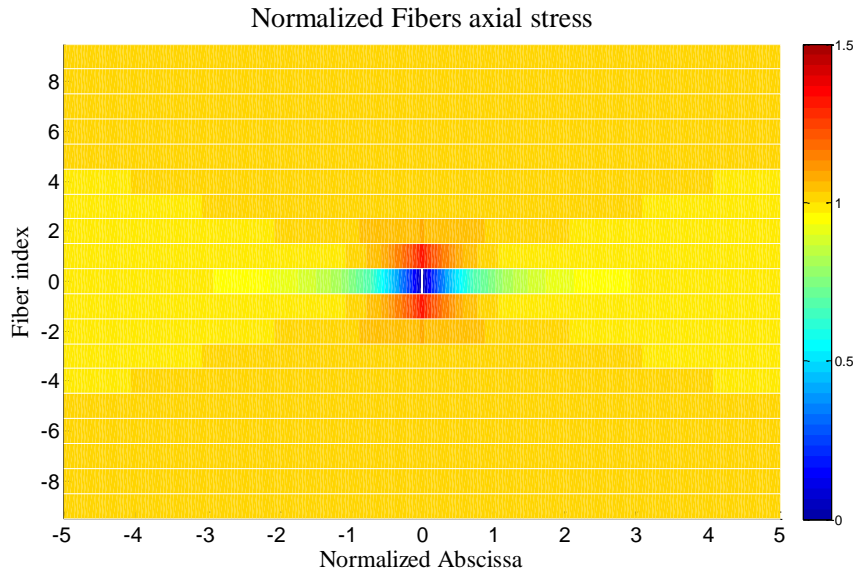


Figure 2.18: Normalized fiber axial stress map

The overstress factors induced to the four fibers neighboring the break site calculated with the shear-lag model were in good agreement with the ones calculated by Beyerlein et al. [1998]. Table 2.3 also shows that these values were in good agreement with the Finite Element model.

Intact fiber's number	1	2	3	4
Overstress factor (Shear-lag model)	1.33	1.067	1.029	1.016
Overstress factor (Finite Element)	1.36	1.062	1.031	1.02
Overstress factor (Beyerlein et al. [1998])	1.33	1.067	1.029	1.016

Table 2.3: Comparison between overstress factors shear-lag vs. Finite Element

A maximum difference of 2% was noticed between the overstress values calculated with the shear-lag model and the ones calculated with the Finite Element model.

Figure 2.19 shows the normalized axial stress in the four fibers near the break site. Figure 2.20 shows the matrix shear stress in the matrix band near the break site.

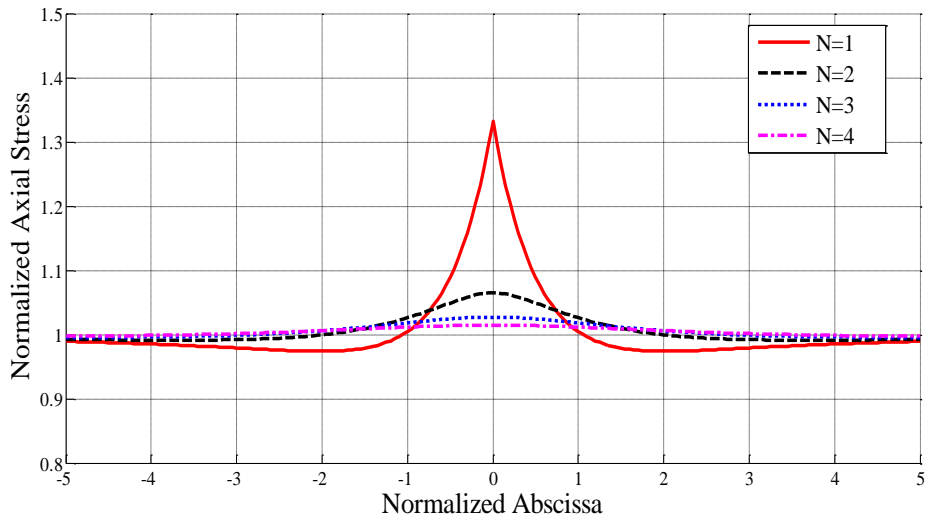


Figure 2.19: Normalized fiber axial stress diagram

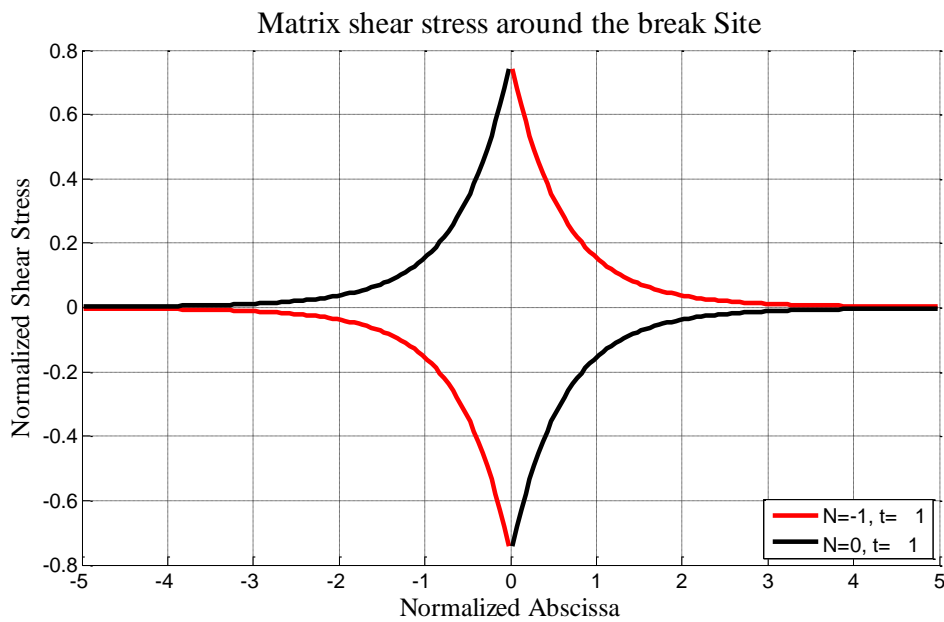


Figure 2.20: Normalized matrix shear stress around break site

The matrix shear stresses around break site were also found in good agreement with the results presented in the study of Beyerlein et al. [1998].

In the developments of Kotelnikova-Weiler[2012], fiber/matrix debonding was introduced in the shear lag model. Table 2.4 shows the influence of introducing the fiber/matrix debonding on the overstress factors calculated with the shear-lag model and with Finite Element method.

Intact fiber number	1	2	3	4
Overstress factor (Shear-lag) with debonding	1.282	1.085	1.038	1.021
Overstress factor (Finite Element) with debonding	1.283	1.085	1.039	1.022

Table 2.4: Overstress factors with fiber/matrix debonding shear-lag vs. Finite Element

Good agreement was found between the two modeling techniques (shear-lag and Finite Element).

Progressive damage with multiple fiber break

In this section we estimate the ultimate tensile strength of a GFRP with both modeling strategies (shear-lag and Finite Element). An incremental stress load is applied at the tip of the fibers located on the right edge of the specimen (Figure 2.15). The analysis will allow us to compare the two models i.e. to compare the number/location of fiber breaks, the developed stresses/strains, etc. Figure 2.21 shows the stress strain curves obtained by shear-lag theory and by the Finite Element approach taking debonding into consideration. The curves obtained from the two models (Finite Element/shear-lag) show a plateau at $P=2050$ MPa. This load is the maximum load supported by the specimen in the shear-lag model since the test performed is stress-controlled and we cannot go further. However, as we will see in the next chapters, this is not the case for the Finite Element model which can also be displacement-controlled allowing us to model the post-peak behavior.

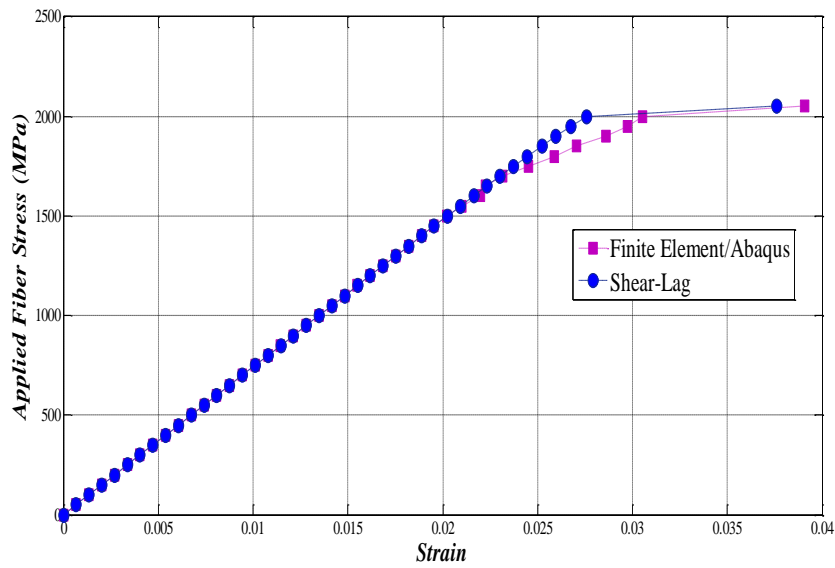


Figure 2.21: Comparison between Finite Element and shear-lag models for the applied fiber stress versus strain curve

In Figure 2.22 we present the evolution of the number of fiber breaks in function of the applied load for both models. Good agreement is observed.

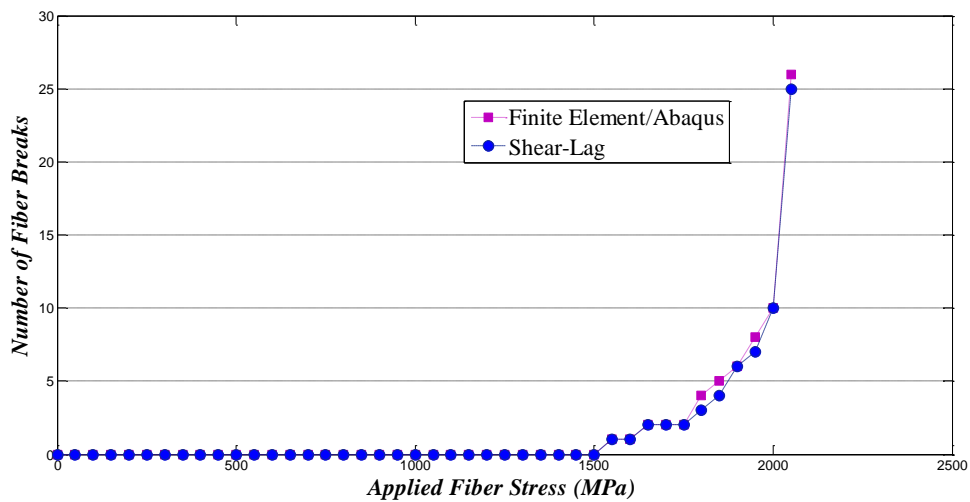


Figure 2.22: Comparison between Finite Element and shear-lag models for the evolution of the number of fiber breaks with the applied fiber stress

The position of the fiber break sites is also of great interest. Figure 2.23 shows the position of fiber breaks at P=1900 MPa given by the two models. The positions coincide.

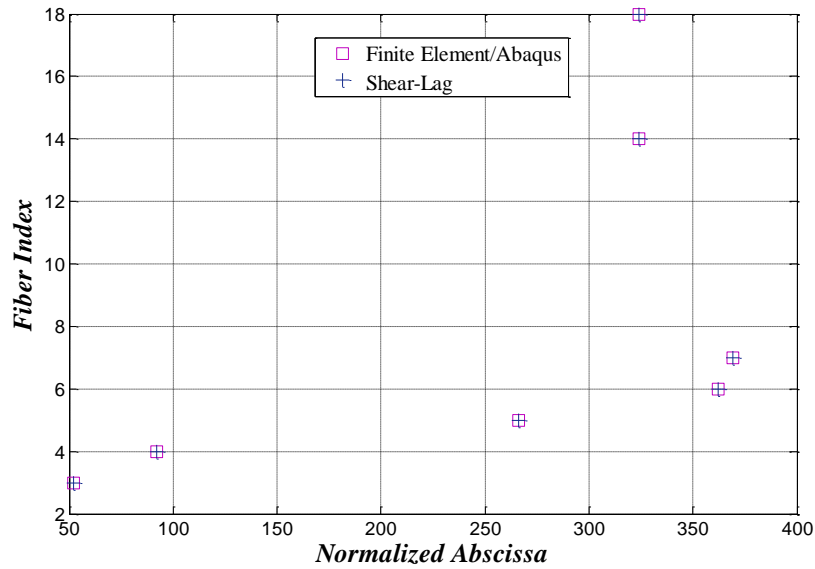


Figure 2.23: Comparison between Finite Element and shear-lag models for the fiber breaks sites at $P=1900$ MPa

In Figure 2.24a we present the normalized fiber stress state for a specimen at $P=2050$ MPa, while Figure 2.24b shows the position of the matrix debonded region together with fiber rupture sites. The fiber rupture sites are indicated with vertical rectangles and the matrix debonded regions with horizontal lines.

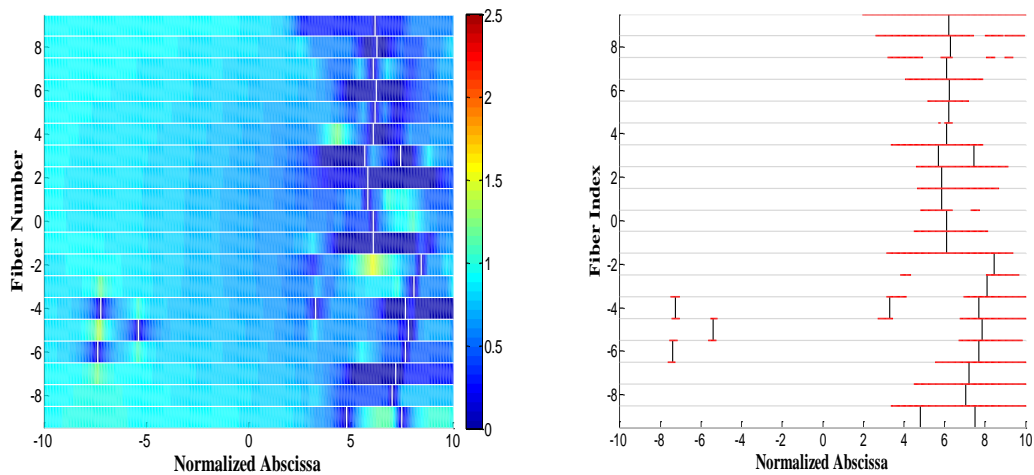


Figure 2.24: (a): Normalized fiber axial stress for $P=2050$ MPa; (b): Fiber break sites and matrix debonded regions for $P=2050$ MPa

The locations of fiber rupture sites as well as the debonded matrix elements indicate the formation of a failure plane. The rupture of the composite is due to fiber breakage accompanied by fiber/matrix debonding. Figure 2.25 shows the stress strain curve when fiber/matrix debonding is taken into account, while Figure 2.26 shows the stress strain curve obtained from the shear-lag model when fiber/matrix debonding is neglected.

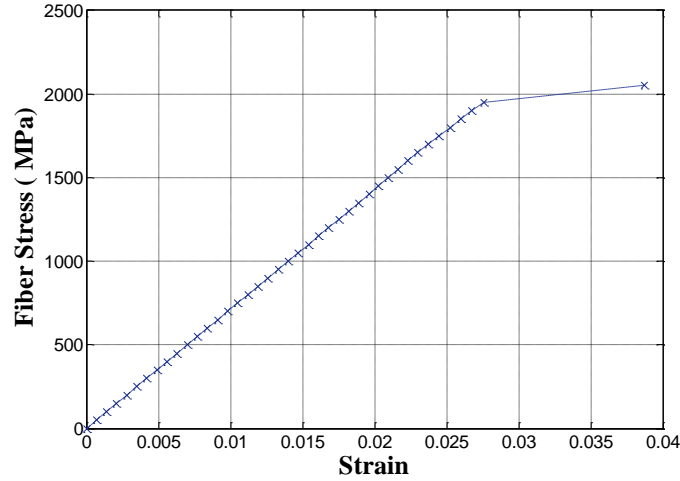


Figure 2.25: Fiber stress versus strain curve (fiber/matrix debonding taken into account)

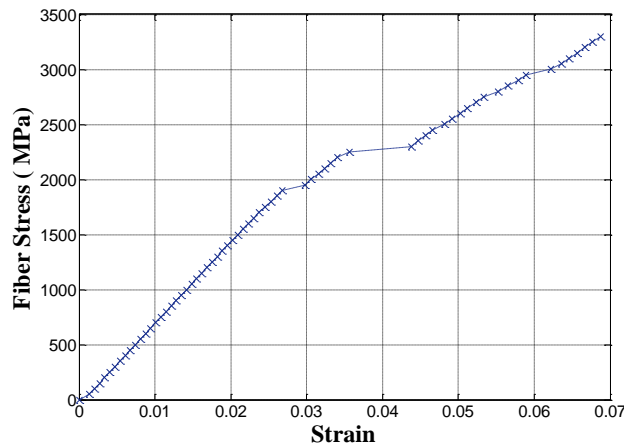


Figure 2.26: Fiber stress versus strain curve (fiber/matrix debonding neglected)

Figure 2.25 shows a clear plateau at $P=2050$ MPa while Figure 2.26 shows a curve with 2 slight plateaus on $P=1950$ MPa and $P= 2200$ MPa. The curve shows bilinear response. When debonding was neglected, the specimen shows high resistance even if the applied load exceeds 2050 MPa. This is due to the fact that no limitations are considered on the

matrix capacity of transmitting shear forces. Moreover, Figure 2.27 shows the normalized fiber stress state at a load level of 3500 MPa when fiber/matrix debonding is neglected. The fiber rupture sites are plotted with vertical rectangles. The specimen shows the presence of multiple cracks aligned at two or three sections which could not physically occur. Furthermore, Figure 2.28 shows in red and blue the position of the matrix shear stresses that exceeds the maximum shear stress value supported by matrix elements. Therefore, when fiber/matrix debonding is neglected, the response of the specimen obtained from the shear-lag model is not physical and cannot represent the actual behavior of the composite.

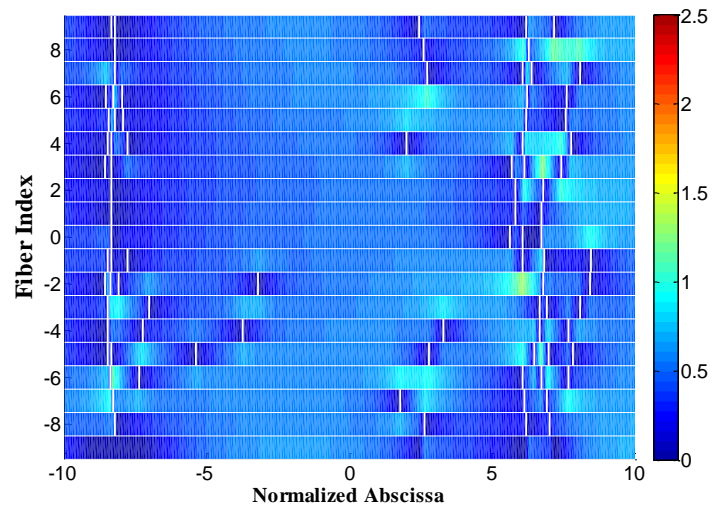


Figure 2.27: Normalized fiber stress state at $P=3500$ MPa (fiber/matrix debonding neglected)

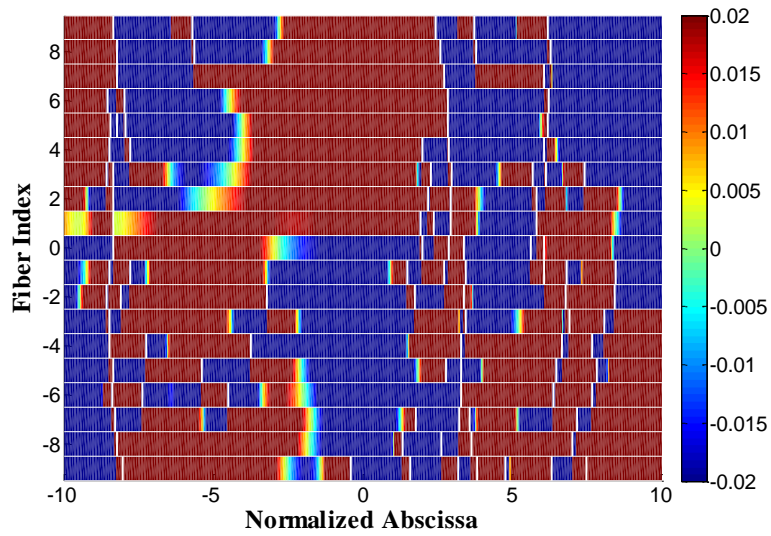


Figure 2.28: Matrix shear stress state at $P=3500$ MPa (fiber/matrix debonding neglected)

At the other hand, Figure 2.29 shows the evolution of the number of debonded region with the applied stress when fiber/matrix debonding was considered in the calculations. The number of matrix debonded elements varies rapidly from 188 to 1645 when the applied fiber stress reaches 2050 Mpa, this phenomenon combined with fiber breakage lead to the rupture of the specimen.

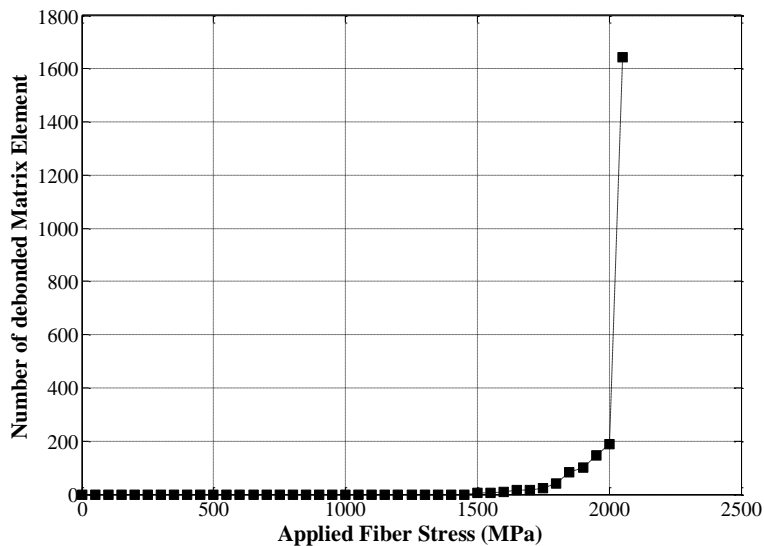


Figure 2.29: Evolution of the number of matrix debonded elements with the applied fiber stress

In conclusion, good agreement was found between shear-lag model and Finite Element model. However, when neglecting the fiber/matrix debonding in the shear-lag model (Beyerlein et al. [1998]) the results obtained in terms of ultimate tensile strength were not physical and could not represent the behavior of composites.

2.4.2 Creep tests

Creep tests are conducted at a sustained load of 1800 MPa (85% of the ultimate tensile strength). The long term behavior of the specimen under sustained tension load is monitored. The results obtained via Finite Element and shear-lag are superposed. A period of 50 years is considered in this analysis. The simulation parameters are summarized in the Table 2.2.

Figure 2.30 shows a comparison between the Finite Element model and the shear-lag model for the evolution of the apparent modulus (Eq. 2.127) with time while Figure 2.31 shows the same comparison for the evolution of the deformation (Eq. 2.128) with time. Figure 2.32 also shows a comparison for the evolution of the number of fiber breaks with time. A good agreement is observed.

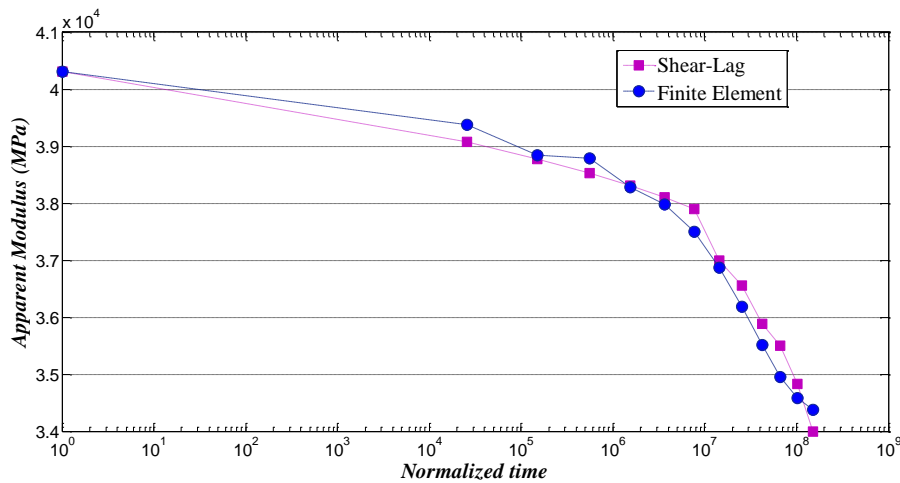


Figure 2.30: Comparison between Finite Element and shear-lag models for the evolution of the apparent modulus with time

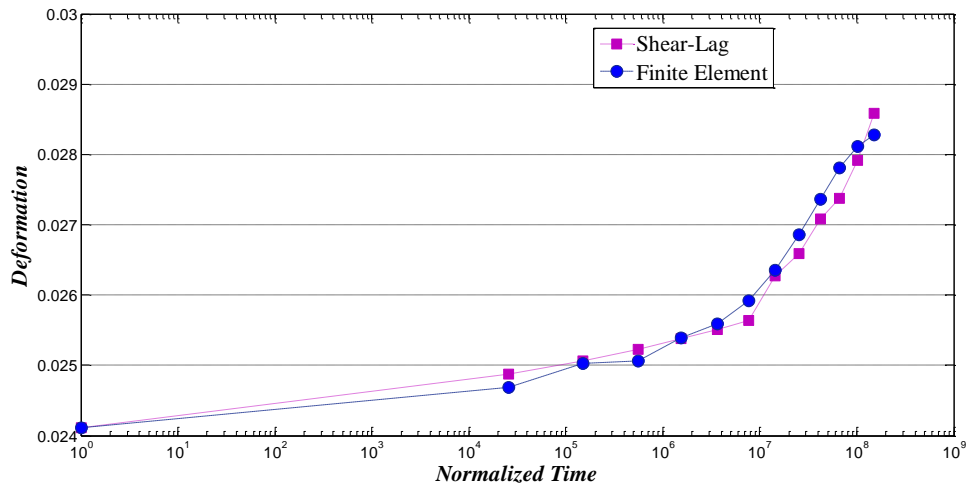


Figure 2.31: Comparison between Finite Element and shear-lag models for the evolution of the deformation with time

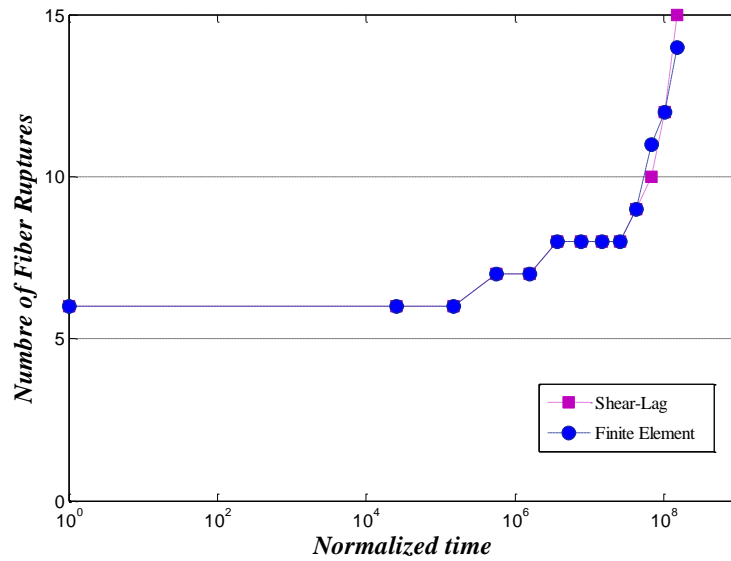


Figure 2.32: Comparison between Finite Element and shear-lag models for the evolution of the number of fiber breaks with time

Another parameter of interest is the position of the fiber rupture at a given time step. Figure 2.33 shows the position of fiber ruptures at the fourth time step calculated using the two modeling techniques (Finite Element and shear-lag).

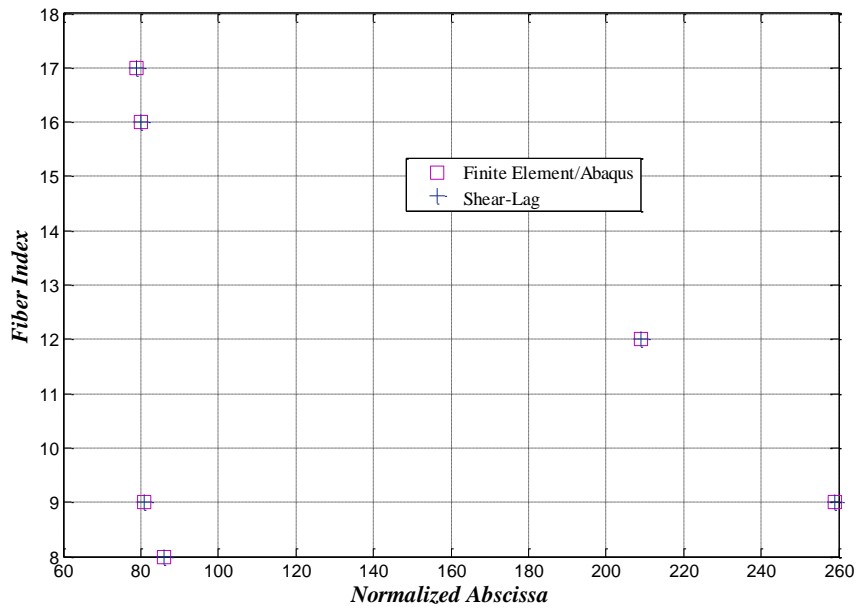


Figure 2.33: Comparison between Finite Element and shear-lag models for the fiber break sites at the fourth time step

The fiber break sites given by the two modeling techniques at the fourth time step coincide.

2.5 Conclusion

In this chapter the classical 2D shear-lag model based on the study of Beyerlein et al. [1998] and Kotelnikova-Weiler[2012] is enhanced and validated. A parametric analysis was performed to the shear-lag model that was previously developed in the work of Kotelnikova-Weiler[2012] in the aim of calibrating its various numerical parameters i.e. the time step, the mesh size, the number of fibers taken into account and the length of the specimen. The model was also extended in order to take periodic boundary conditions that enabled the derivation of the effective properties of the material (such as the apparent modulus). In the aim of validating the several assumptions of the shear-lag model, a Finite Element model was developed using the software Abaqus. In the Finite Element model, the fibers were modeled as rod elements, the matrix was modeled as a 2D membrane element whose properties are such to transfer the shear stresses in the same way as in the shear-lag model. Ultimate tensile strength and creep tests were performed for one generated specimen using both modeling techniques. Stresses, strains and fiber

break sites were compared and good agreement was found. The calculations performed showed that the enhanced shear-lag model does not suffer from numerical errors and that it can capture quite well the mechanical behavior of UD composites in short and long-term. It is to be noted that the effect of the strength and statistical variability of fibers on the mechanical behavior of unidirectional composite materials was not analyzed in this chapter. It will be thoroughly discussed in chapter 3. In order to perform such task, MonteCarlo simulations needs to be undertaken by generating several specimens instead of one. It worth emphasizing that this type of calculations was not performed in the work of Beyerlein et al. [1998] and Kotelnikova-Weiler[2012]. In this current chapter, the simulations were performed on P122 glass fibers, however in the following chapters several types of fibers will be considered (such as PU glass fibers and T300 carbon fibers).

Chapter 3: Statistical variability of fibers strength and its influence on creep rupture of FRPs under tension loads

In this chapter we take benefit of the calibrated models presented in chapter 2 to analyze the effect of changing the reinforcing material on the overall behavior (short- and long-term) of the composite. The influence of the statistical variability of the fiber strength on creep is thoroughly discussed in this chapter using MonteCarlo simulations. A comparative study between the creep curves calculated using the developed models with some of the empirical formulas that exist in the literature is also presented.

Content

3.1 Introduction	88
3.2 Short/Long term behavior of GFRPs/CFRPs	88
3.2.1 Simulation procedure	89
3.2.2 Ultimate tensile strength	90
3.2.3 Creep tests.....	92
3.3 Conclusion.....	101

3.1 Introduction

In the previous chapters, the creep of composites under sustained tension loads was thoroughly discussed. Experimental work and theoretical models that exist in the literature to describe the creep were exposed and detailed. In particular the shear-lag theory was presented, enhanced and validated using a developed micromechanical model that is based on the Finite Element technique. In the previous calculations, the role of the matrix in terms of viscoelasticity and debonding was assessed and explained. Several calculations were performed showed that when fiber/matrix debonding was neglected the response of the shear-lag model was wrong and could not represent the true behavior of the composite. However, no parametric analysis was performed on the reinforcing material (fibers) to assess its influence on the creep rupture. In other words, the analysis was performed on P122 glass fibers only and it was based on one realization (one generated specimen) which is not sufficient to represent the behavior of the composite. MonteCarlo simulations are therefore necessary to take into account the statistical variability of the reinforcing material (fibers). In this current chapter, we take benefit of the calibrated models that were presented in chapter 2 (shear-lag and Finite Element) to perform ultimate tensile strength calculations and also creep tests for three types of fibers (P122 glass fibers, PU glass fibers, T300 carbon fibers). The ultimate tensile strength calculations are performed using the Finite Element model, benefiting from its capability to perform displacement controlled test (instead of stress controlled stress that was considered in the shear-lag models of Beyerlein et al. [1998]/Kotelnikova-Weiler[2012]) which can allow us to model the post peak behavior of the composite. The results obtained for each type of fibers in terms of stresses and strains are average values for 50 generated specimens. The creep tests were performed on the generated specimens at several load levels for a period of 50 years. A comparison between the creep results obtained from the developed models with the Findley [1956] power law is also presented.

3.2 Short/Long term behavior of GFRPs/CFRPs

In this section we analyze the creep behavior of composites reinforced with glass/carbon fibers. Using shear-lag/Finite Element models, we assess the instantaneous response of the composite as well as their creep. First the ultimate tensile strength is estimated for each type of fiber. Then at later stage its long term behavior is calculated at sustained tension loads of 70% and 80% of its ultimate tensile strength for a period of 50 years. In

order to take into account the statistical variation of fiber strength in the specimens, MonteCarlo simulation was performed and 50 specimens were considered in the calculations. The results shown below are average values of stresses and strains obtained from the different specimens considered. Three types of fibers are considered in the analysis. P122, PU glass fiber and T300 Carbone fiber (Zinck[2011]/ Baxevanakis et al. [1998]).

3.2.1 Simulation procedure

The simulation procedure remains as described in sections 2.2.4 and 2.3 when it comes to ultimate tensile strength calculation and creep tests. We assume that the fiber strength obeys the Weibull distribution. Both unimodal and bimodal Weibull distributions have been considered in the calculations of the fibers strength (see section 2.2.4 and particularly Eq. 2.123 and Eq. 2.125 for the cumulative distribution functions for unimodal and bimodal Weibull distribution; see Tables 2.2 and 3.1 for typical values of the distribution parameters). In our case the spatial discretization Δx is a very small quantity and consequently the consideration of a bimodal distribution for the fiber strength is not very important. This is illustrated in Figure 3.1 in which we present the probability density functions for the three types of fibers that are considered in this study (PU glass fiber, P122 glass fiber and T300 carbon fiber).

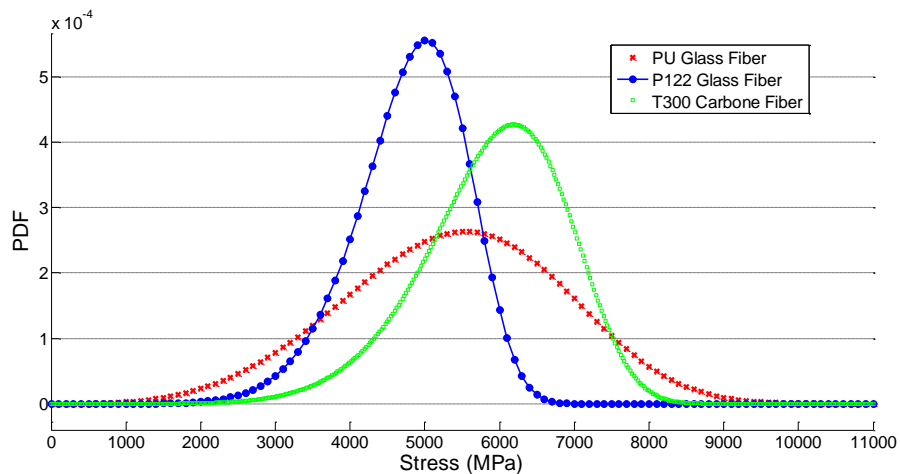


Figure 3.1: Probability density functions for the three types of fibers

Figure 3.2 shows the fibers strength distribution for a given realization that is based on P122 glass fibers Weibull distribution (see Table 2.2 for the characteristics of P122 glass

fibers). We note that the parameters presented in Table 3.1 are thoroughly detailed in section 2.2.4 of chapter 2).

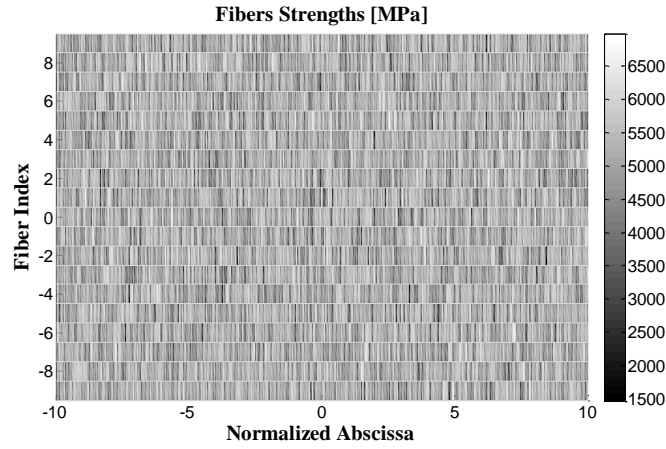


Figure 3.2: Fibers strengths for a given specimen composed by 19 fibers

RVE characteristics		T300 carbon fiber characteristics		PU glass fiber characteristics	
2N + 1 (Total Number of fibers)	19	σ_0 (MPa)=6318		σ_{01} (MPa)	1840
Length of the specimen(mm)	0.37			σ_{02} (MPa)	5930
Δx	0.025	$m=7.26$		m_1	6.3
V_f %	54.5			m_2	4.11
q_0 (PU Glass fiber)	0.27	E_f (MPa)	230000	E_f (MPa)	74000
l_0 (mm) : PU(mm)	50	r_f (μm)	3.5	r_f (μm)	6

Table 3.1: Simulation parameters for T300 carbon fibers and PU glass fibers. Zinck [2011]/ Baxevanakis et al. [1998]

3.2.2 Ultimate tensile strength

In this section the Finite Element method was used. The ultimate tensile strength is estimated for each type of fiber using a displacement-controlled test (see Figure 2.15) that allows us to model the post-peak behavior of the composite. We note that this type of

simulations could not be performed with the shear-lag method (as it is formulated in this thesis) where only stress load could be applied as a load case. Figure 3.3 shows the stress/strain curve obtained for P122 glass fibers. It shows a clear peak at P=2050 MPa for a strain value of 3.1%.

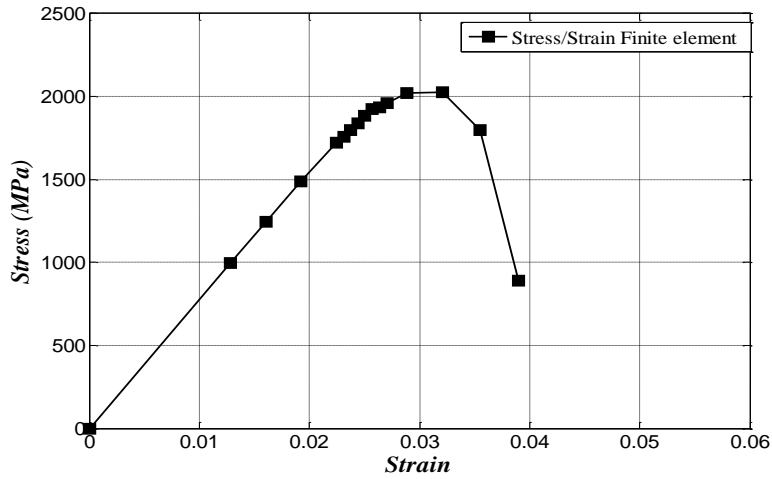


Figure 3.3: Average stress/strain curve: Finite Element method (P122 glass fibers)

Figure 3.4 shows the stress/strain curve obtained for the PU glass fibers. The peak is at P=1150 MPa for a strain value of 1.55 %. Figure 3.5 shows the stress/strain curve obtained for the T300 carbon fibers. It shows a clear peak at P=2450 MPa for a strain value of 1%.

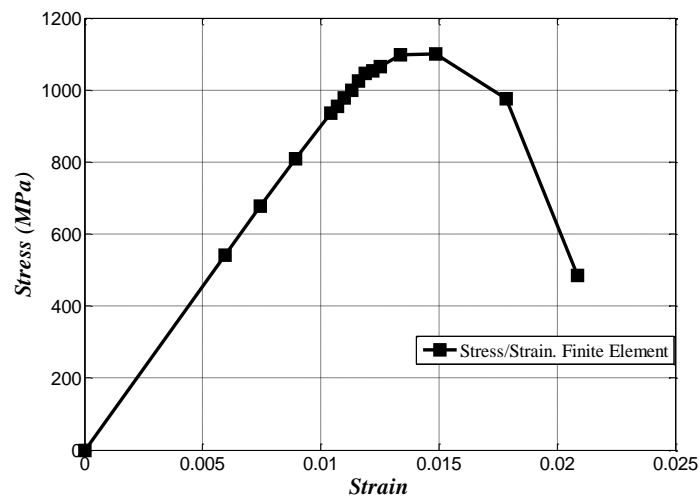


Figure 3.4: Average stress/strain curve: Finite Element method (PU glass fibers)

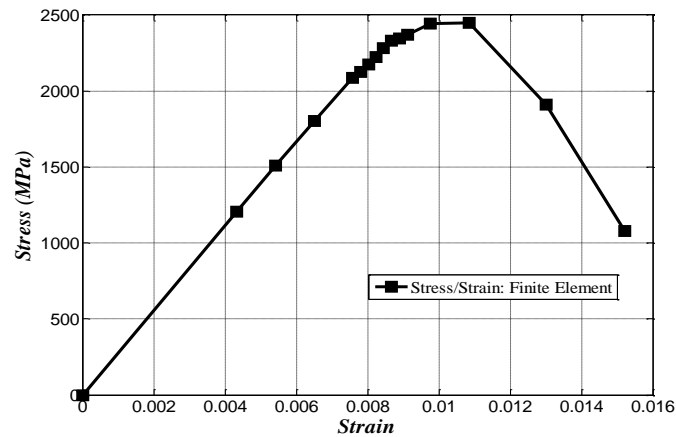


Figure 3.5: Average stress/strain curve: Finite Element method (T300 carbon fibers)

As it is expected, the value of the tensile strength of the specimens made of PU/P122 glass fibers is smaller than the one of the specimens with T300 carbon fibers. Table 3.2 summarizes the obtained ultimate tensile strength for the three different fiber types along with the standard deviation values.

Fiber Type	Calculated tensile strength (MPa)	Standard deviation (MPa)	Tensile strength according to Zinck [2011]/ Baxevanakis et al. [1998] (MPa)
P122 glass fiber	2050	112	2020
PU glass fiber	1150	57	1080
T300 carbon fiber	2500	131	2667

Table 3.2: Ultimate tensile strength for the three fiber types

3.2.3 Creep tests

The monitoring of the creep was conducted at two load levels, 70% and 80% of the ultimate tensile strength for each type of fiber. The average apparent modulus and average deformation (for 50 specimens) evolution with time is calculated. A period of 50 years is considered in the calculations. Figures 3.6 and 3.7 show that the level of creep is higher for $P=0.8 \times P_u$ (80% of the ultimate tensile strength) for P122 glass fibers. Primary, secondary and tertiary creep were also observed for $P=0.8 \times P_u$ (see Figure 3.7).

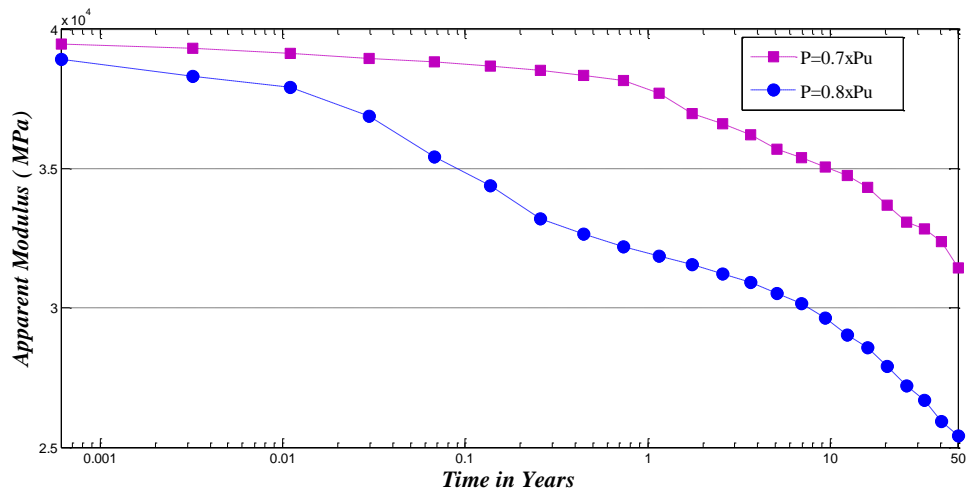


Figure 3.6: Average apparent modulus versus time for $P=0.7xPu$ and $P=0.8xPu$ for P122 glass fibers

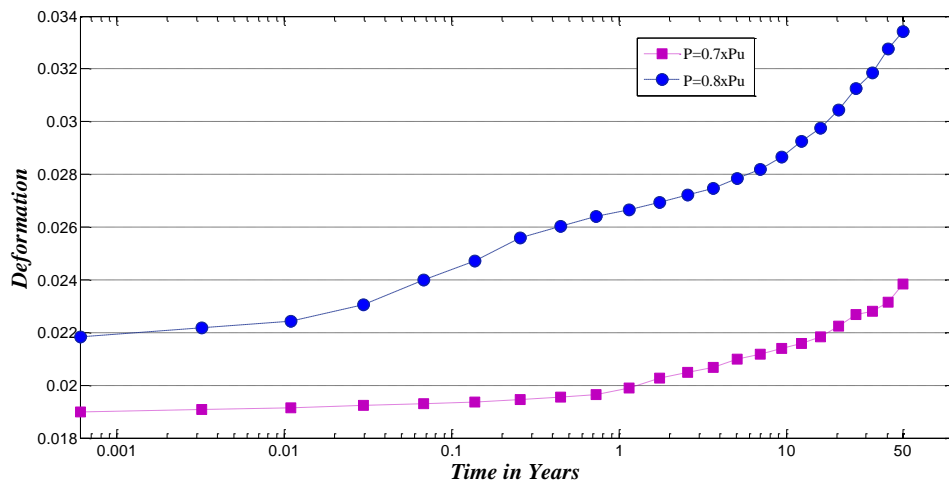


Figure 3.7: Average deformation versus time for $P=0.7xPu$ and $P=0.8xPu$ for P122 glass fibers

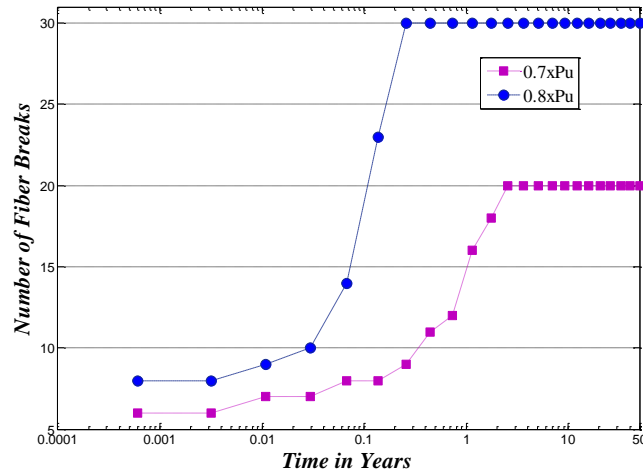


Figure 3.8: Evolution of the number of fiber breaks versus time for $P=0.7xPu$ and $P=0.8xPu$ for P122 glass fibers

Figure 3.8 shows the evolution of the number of fiber breaks with time. Figure 3.8 shows that the number of fiber breaks after 50 years for a sustained load of 80% of the ultimate tensile strength is higher than the one obtained at 70% of the ultimate tensile strength. Figure 3.9 presents the damaged state of one specimen after 50 years at a sustained load of 80% of its ultimate tensile strength. It shows a specimen with multiple fiber breaks that are approximately aligned in a section perpendicular to the applied stress. The alignment of the fiber breaks led to the failure of the specimen (tertiary creep).

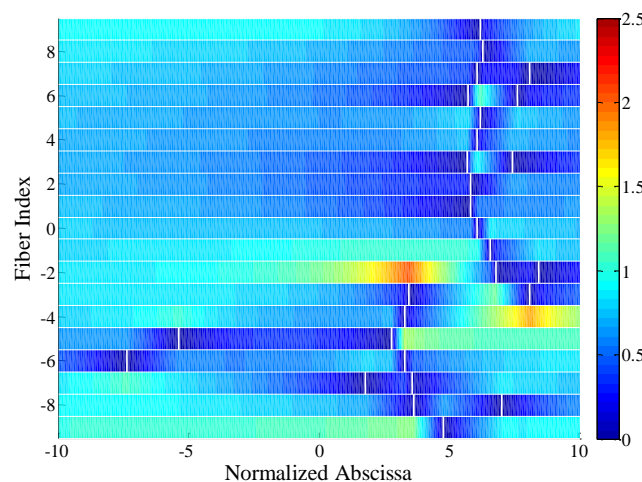


Figure 3.9: Normalized fibers axial stress after 50 years for P122 glass fibers at $P=0.8xPu$

Figures 3.10 and 3.11 also show similar behavior for the PU glass fibers. The level of creep is higher for $P=0.8xPu$. Primary, secondary and tertiary creep were also observed for $P=0.8xPu$ (see Figure 3.11).

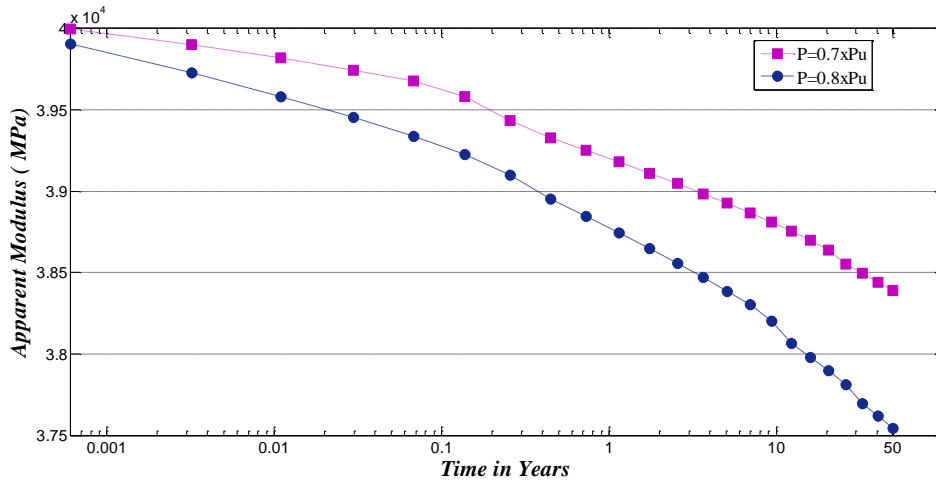


Figure 3.10: Average apparent modulus versus time for $P=0.7xPu$ and $P=0.8xPu$ for PU glass fibers

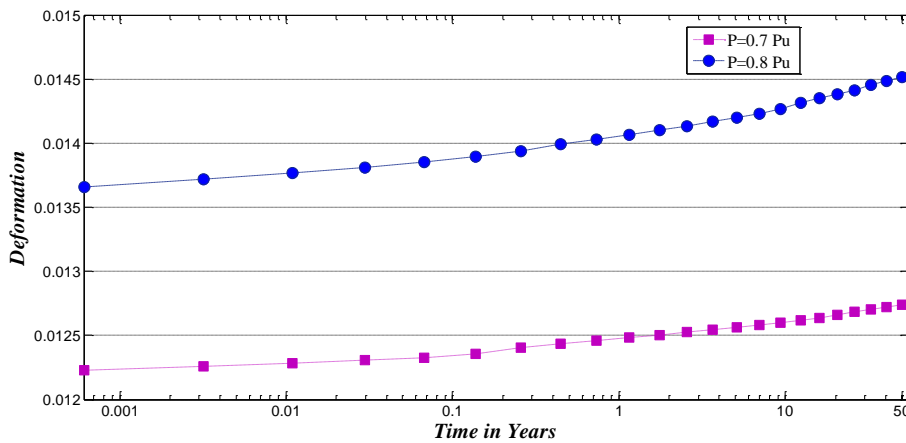


Figure 3.11: Average deformation versus time for $P=0.7xPu$ and $P=0.8xPu$ for PU glass fibers

Figure 3.12 shows the evolution of the number of fiber breaks with time. Figure 3.12 shows that the number of fiber breaks after 50 years for a sustained load of 80% of the ultimate tensile strength is higher than the one obtained at 70% of the ultimate tensile strength.

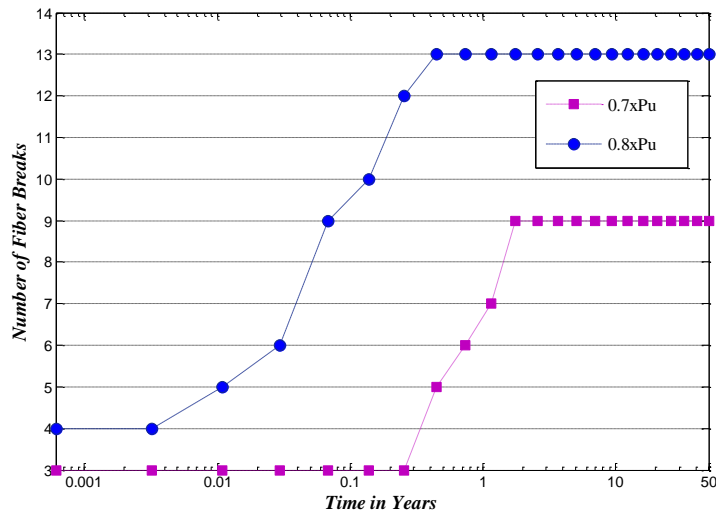


Figure 3.12: Evolution of the number of fiber breaks versus time for $P=0.7xPu$ and $P=0.8xPu$ for PU glass fibers

Figure 3.13 shows also the damaged state of one specimen after 50 years at a sustained load of 80% of its ultimate tensile strength. It shows a specimen with multiple fiber breaks that are approximately aligned in a section perpendicular to the applied stress. The alignment of the fiber breaks led to the failure of the specimen (tertiary creep).

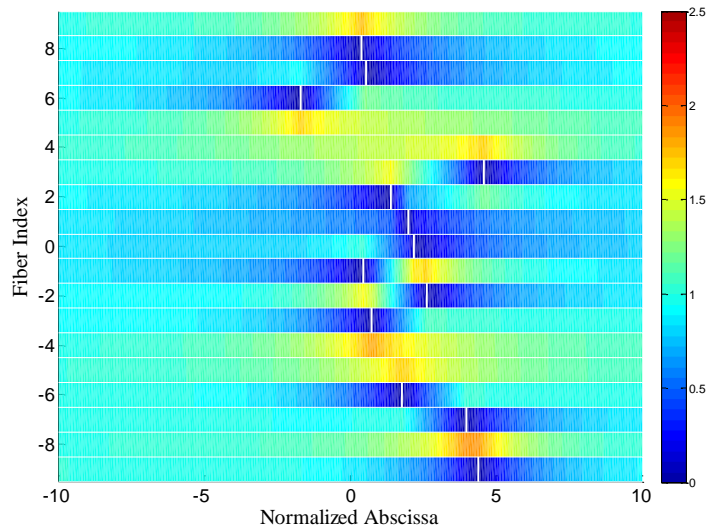


Figure 3.13: Normalized axial stress after 50 years for PU glass fibers at $P=0.8xPu$

Figures 3.14 and 3.15 show lower creep levels for the composite reinforced with carbon fibers. The level of creep for $P=0.8xPu$ is higher than for $P=0.7xPu$, however no tertiary creep is observed at $P=0.8xPu$ (see Figure 3.15).

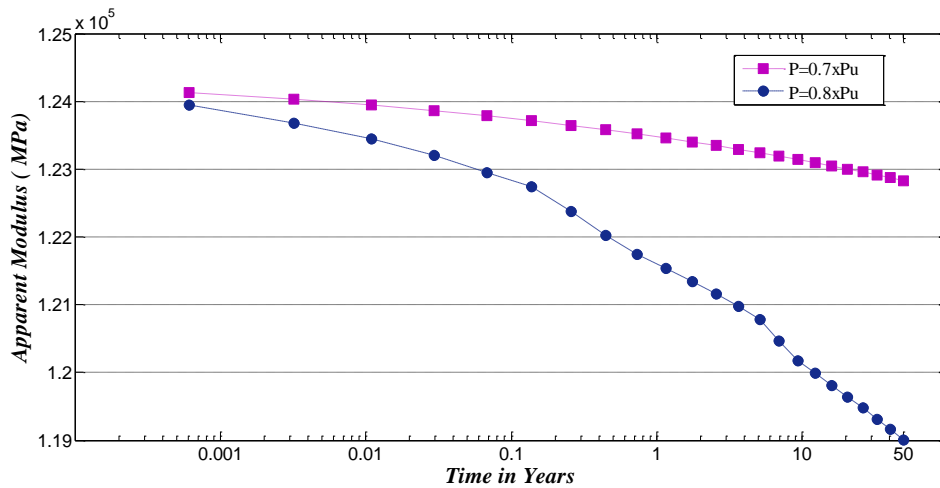


Figure 3.14: Average apparent modulus versus time for $P=0.7xPu$ and $P=0.8xPu$ for T300 carbon fibers

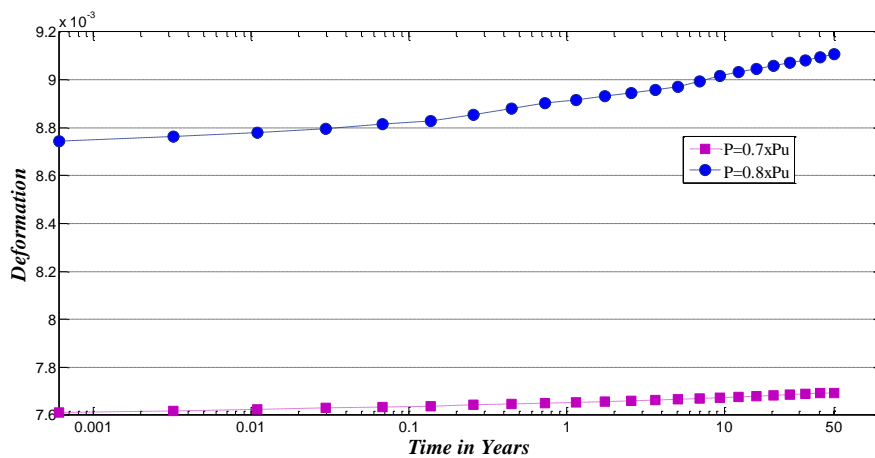


Figure 3.15: Average deformation versus time for $P=0.7xPu$ and $P=0.8xPu$ for T300 carbon fibers

Figure 3.16 shows the evolution of the number of fiber breaks with time. Figure 3.16 shows that the number of fiber breaks after 50 years for a sustained load of 80% of the ultimate tensile strength is slightly higher than the one obtained at 70% of the ultimate tensile strength.

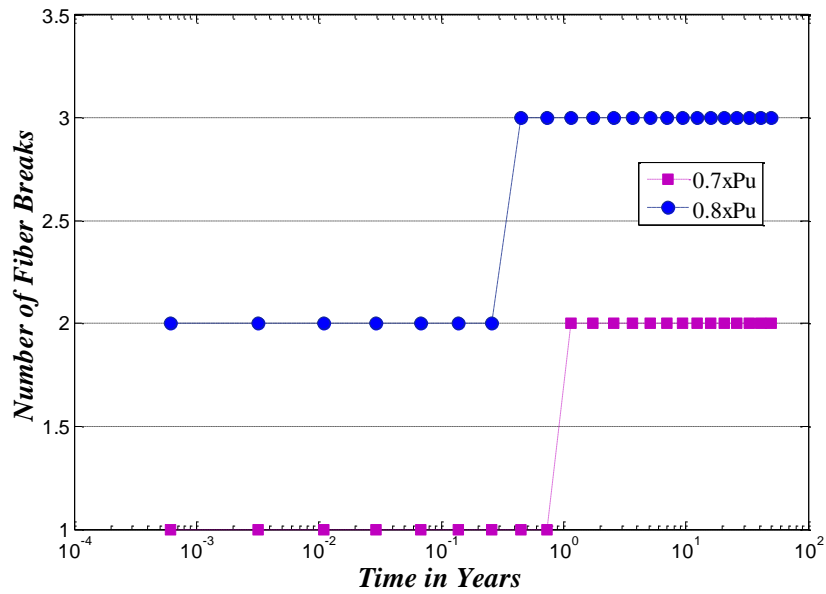


Figure 3.16: Evolution of the number of fiber breaks versus time for $P=0.7xPu$ and $P=0.8xPu$ for T300 carbon fibers

Figure 3.17 shows also the damaged state of one specimen after 50 years at a sustained load of 80% of its ultimate tensile strength. It shows a specimen with only three scattered fiber breaks. Such structure of fiber breaks doesn't lead to the rupture of the specimen.

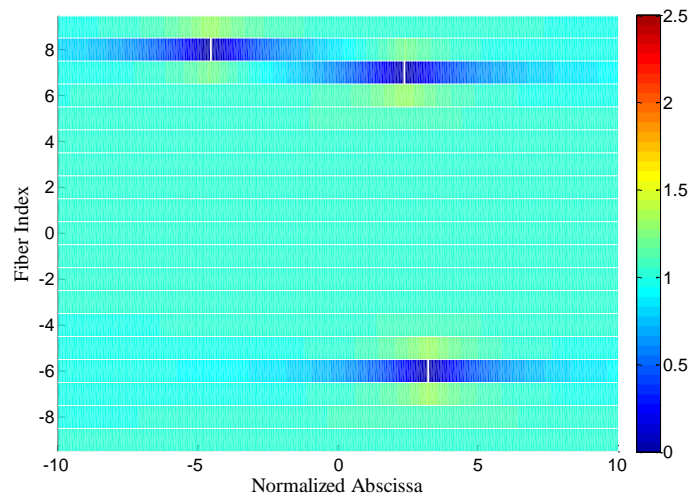


Figure 3.17: Normalized axial stress after 50 years for T300 carbon fibers at $P=0.8xPu$

A comparison of the results obtained on the short/long term behavior of GFRPs/CFRPs with the design codes was performed. According to codes and standards (e.g. ACI

440.2R-02), carbon fibers are the least susceptible to creep rupture; aramid fibers are moderately susceptible, and glass fibers are most susceptible. Good agreement (in terms of tendency of the creep results) was found. At the matter of fact, ACI 440.2R-02 and other design codes recommend a reduction factor that is applied to the ultimate tensile strength of the FRPs in order to avoid creep-rupture and fatigue related failures. It is to be noted that high safety factors are introduced in these reduction factors. As example, we present in Table 3.3 the reduction factors that are found in the ACI codes for glass, aramid and carbon fibers.

The calculations performed in this paragraph showed similar behavior for the composites reinforced with glass fibers at a load level of 80% of the ultimate tensile strength. We note that no tertiary creep was observed for the composites reinforced with carbon fibers at 80% of the ultimate tensile strength. At 70% of the ultimate tensile strength, low creep behavior was observed for composites reinforced with glass/carbon fibers. Moreover, at a stress level lower than 70% of the ultimate tensile strength, no creep behavior is observed when using this type of calculation (shear-lag/Finite element). These calculations showed that the creep exists only when defects are present in the composite, meaning that if the applied load is lower than the smallest value of the fiber strengths no creep is observed. We note that this result is in conformity with the work of Nedjar et al. [2014].

	Glass	Carbon	Aramid
Creep Rupture Stress Limit	0.2xPu	0.55xPu	0.3xPu

Table 3.3: Stress limits of FRPs according to ACI code

Figure 3.18 presents the evolution with time of the average rupture sites position for 50 specimens at $P=0.8xPu$ for the P122 glass fibers as well as for the PU glass fibers.

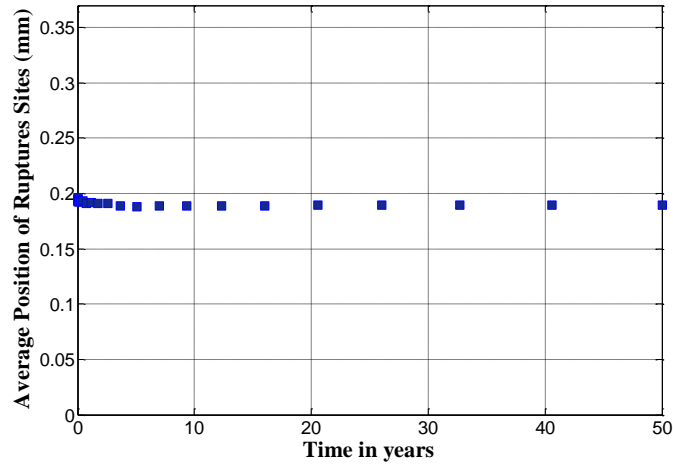


Figure 3.18: Evolution with time of the average position of rupture sites (P122/PU glass fibers)

We note that the average rupture sites abscissa coincides with the middle of the specimen ($X=0.18$ mm) with a standard deviation of 0.063 mm for P122 glass fibers and 0.081 mm for PU glass fibers. Figure 3.19 shows a fitting of the deformation evolution with time $\varepsilon(t)$ given by the shear-lag theory with the Findley [1956] power law (Eq. 3.1)

$$\varepsilon(t) = \varepsilon_0 + mt^n \quad (3.1)$$

where ε_0 is the instantaneous deformation, t is the time, $m = 0.004103$ and $n = 0.297$

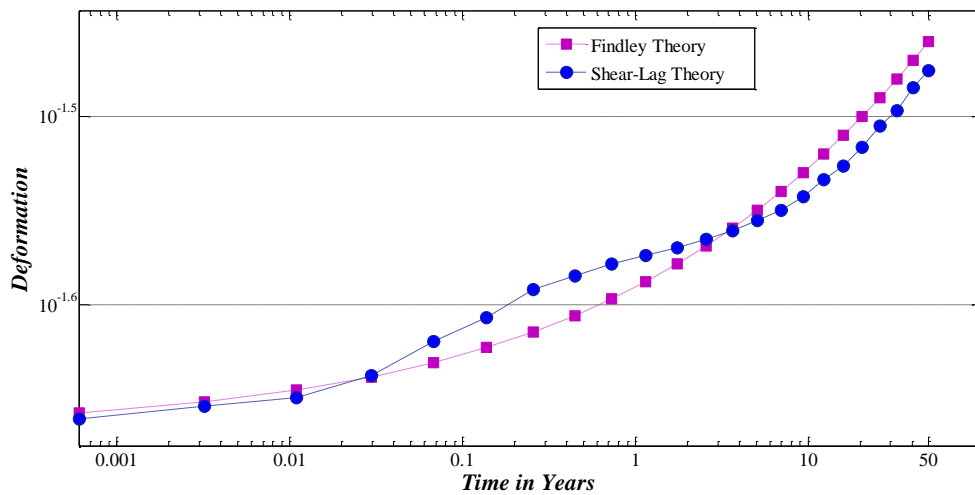


Figure 3.19: Fitting of the deformation evolution given by the shear-lag model with the Findley law for P122 glass fibers

For P122 glass fibers the Findley law fits quite well the data obtained from the shear-lag equations ($m = 0.004103$, $n = 0.297$). The present numerical model could be helpful for calibrating similar empirical laws based on the micromechanical parameters of the fibers and the matrix. Moreover, it can give useful information on tertiary creep and failure, which the equivalent laws do not provide.

3.3 Conclusion

The effect of the strength and statistical variability of fibers was studied in this chapter. In order to accomplish such task, MonteCarlo simulations were performed and the results obtained in terms of creep and ultimate tensile strength were based on 50 realization instead of one (Beyerlein et al. [1998]/Kotelnikova-Weiler[2012]). The effect of changing the reinforcing material on the behavior of the composite was also assessed. Three different kinds of fibers, i.e. glass and carbon, were considered in the calculations and their influence on the long-term behavior of the composite and its ultimate tensile strength was explored. As it is expected, the value of the tensile strength of the specimens made of PU/P122 glass fibers is smaller than the one of the specimens with T300 carbon fibers. The creep behavior of the generated specimens was monitored at two different load levels (70% and 80% of the ultimate tensile strength). Tertiary creep was observed at a load level of 80% of the ultimate tensile strength during a period of 50 years for composites reinforced with glass fibers, however composites reinforced with carbon fiber showed lower creep tendency since for the CFRP specimens no tertiary creep was observed. Results showed that the GFRP specimens attained rupture after certain time under sustained loads lower than their ultimate tensile strength (80% of the ultimate tensile strength). The simulations confirmed that creep rupture can occur even though the applied load is smaller than the composite's ultimate strength.

Chapter 4: Creep rupture of FRPs to bending and shear loads

In previous chapters, the behavior of unidirectional composite materials under sustained tension loads was thoroughly analyzed. In this part of the thesis, additional loading patterns are considered in the analysis, such as compression, bending and shear. In the first part of the chapter, we present the different models that exist in the literature for the estimation of the compressive strength of composites, because unlike tension, there is no clear criterion for the fibers resistance in compression. Simulations under bending loading for different types of fibers are also presented in this chapter. Moreover, the effect of adding an additional shear stress to tension loads on the creep of composites is discussed.

Content

4.1 Introduction	105
4.2 Response of FRPs to bending loads	113
4.3 Combined shear and tension	116
4.4 Conclusion.....	120

4.1 Introduction

In previous chapters the behavior of composite materials under sustained tension load was thoroughly analyzed. However, in most structural elements, especially the beams/slabs elements, tension load may coincide with shear and with compression. Moreover, some of the main structural elements behavior may be controlled by compression load such as columns. Therefore the behavior of composites under different loading patterns needs to be evaluated. Indeed, under bending, part of the composite is subjected to tension while the other part is subjected to compression. Previous chapters discussed thoroughly the behavior of composites under tension loads and the effect of the presence of defects in fibers on the composite behavior. When it comes to compression, the failure of composites is directly related to buckling. Buckling may be at a global (structure) or local level (fibers). In either case it severely limits the structural efficiency of the system and leads to under-utilization of the true material properties. It also makes the structure highly sensitive to imperfections. In order to predict the compressive strength of unidirectional composites, several research works were performed. At the matter of fact, it was Rosen [1965] that triggered the investigation on the compressive behavior of unidirectional (UD) composite materials. In recent years, numerous models for the prediction of compressive behavior of UD composites have been developed by the researchers (Camponeschi [1991], Schultheisz et al.[1996]) . Micro buckling or kinking of fibers have been identified to be the mechanisms by which UD composites fail under compression. Micro buckling is the buckling of fibers embedded in matrix foundation (see Figure 4.1). Kinking, on the other hand, is a highly localized fiber buckling. At the matter of fact, kink bands are formed after attainment of the peak compressive load when the region between the fibre breaks is deformed plastically (see Figure 4.2). Rosen's [1965] analysis on the compressive strength of unidirectional composite materials was based on micro buckling approach. Two failure modes were identified by Rosen [1965]; the extension failure mode where fibers buckle out of phase and the shear failure mode where fibers buckle in phase (see Figure 4.1). Rosen [1965] signaled that the shear failure mode predicted lower compressive strength than the extension mode. Furthermore, when comparing results obtained by shear failure mode to experimental data low correlation was found. The predicted results of compressive strength were found higher than the experimental data.

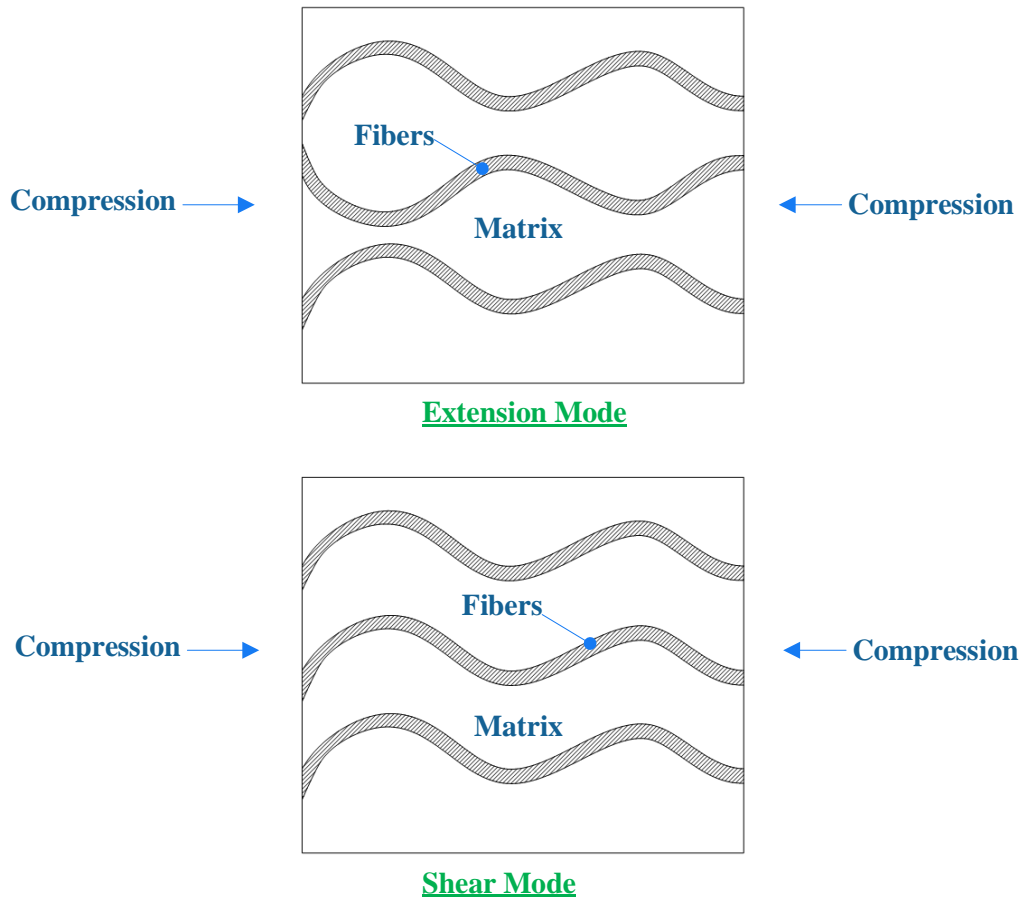


Figure 4.1: Micro buckling failure mode

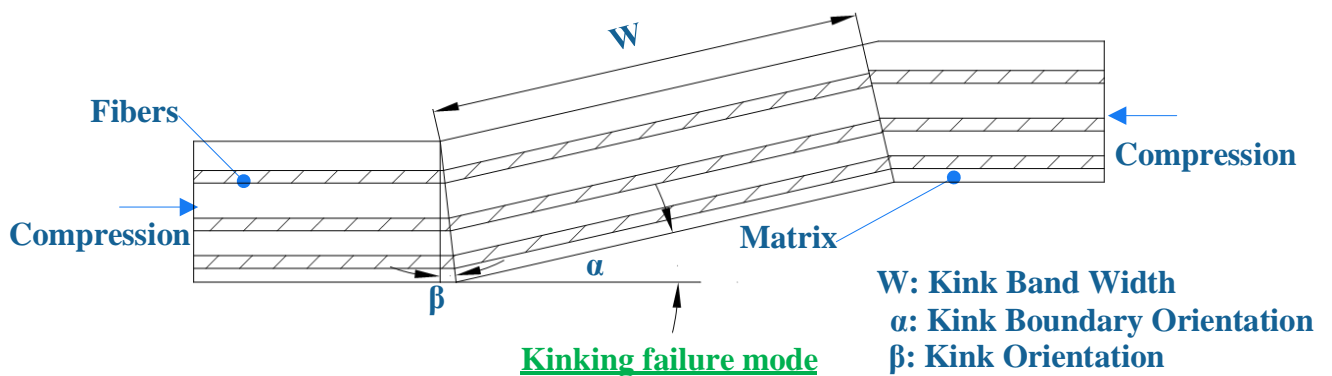


Figure 4.2: Kinking failure mode

It was Greszczuk [1975] that extended Rosen's approach by performing 3D analysis. The results obtained by Greszczuk's model were found in good agreement with his experimental tests on aluminum and steel reinforced epoxy. However, when applied to graphite/epoxy and boron/epoxy composites, it performed poorly. The author reported that his model couldn't

predict adequately the compressive strength of graphite/epoxy and boron/epoxy composites. According to the author, the discrepancies between theoretical calculations and experimental data were caused by initial fiber misalignment, fiber/matrix debonding and non-linear mechanical behavior of the matrix. Yeh et al.[1988] introduced an empirical factor in their model for compressive strength prediction for kevlar/epoxy composites to account for initial misalignment of fibers. Lo and Chim [1992], in their analysis on compression behavior of FRPs, accounted for the unknown boundary conditions of micro buckled region by introducing a semi-empirical factor in their model.

In parallel to the research performed to understand micro buckling, several studies were conducted to analyze the kinking. Budiansky [1983] for instance, addressed the kinking mechanism based on perfect plasticity in pure shear. His model was a combination of Rosen [1965] and Argon's [1972] model. The author neglected the bending resistance of the fibers. However, Slaughter et al. [1994] considered the fiber bending stiffness and random initial fiber waviness in the kinking analysis. In parallel to the elastic and elastoplastic analysis, viscoelastic micro buckling was also examined by Slaughter and Fleck [1993].

It is worth mentioning that the literature shows a considerable amount of work and controversies in the field of compression characterization of composites. Even though analytical studies are available, most of them include empirical factors based on experimental correlation. Consequently, we perform a comparison between the existing theoretical models and the experimental data that exists in the literature in order to obtain adequate values for the compressive strength of unidirectional CFRPs/GFRPs. These values will be considered when a maximum compression stress for the fibers is required in the bending analysis. In the following paragraph, the models/equations for compressive strength prediction of unidirectional composites are briefly presented along with the comparison with the available experimental data.

Literature review to compressive strength of unidirectional composites

As per the work of Naik and Kumar [1999], we present a brief summary on the principle models that exist in the literature for estimating the compressive strength of FRPs at the macroscopic scale.

Rosen model

The Rosen model is based on the elastic buckling of fibers embedded in a matrix using an energetic approach. As previously mentioned, Rosen considered two modes of fiber buckling. The first mode is the extension mode, where fibers buckle out of phase. The second mode is the shear mode, where fibers buckle in phase. The compressive strength (at the macroscopic scale) for each failure mode X_c is given by equations 4.1 and 4.2.

Extension mode:

$$X_c = 2V_f \sqrt{\frac{V_f E_m E_f}{3(1 - V_f)}} \quad (4.1)$$

Shear mode:

$$X_c = \frac{G_m}{(1 - V_f)} \quad (4.2)$$

where E_m is the matrix Young's modulus; E_f is the fibers Young's modulus; G_m is the matrix shear modulus and V_f is the fibers volume fraction.

It was reported that the shear mode predicts lower compressive strength than the extension mode. However, the shear mode compressive strength is found higher than the one given by experimental data. We note that equation 4.2 indicates that the compressive strength of a given composite is independent from the type of the fiber reinforcement. However, experiments made on composites reinforced with different types of fibers have shown different compressive strengths. It is worth mentioning that the Rosen model neglects the effect of the presence of possible imperfections in the composites.

Lo-Chim model

The Lo-chim model is based on local micro buckling. Lo and Chim [1992] extended the Timoshenko buckling load of a simply supported beam to account for the incertitude in the boundary conditions in a buckled region of a UD composite material. The beam properties were replaced by the composite properties (Eq. 4.3).

$$X_c = \frac{G_{12}}{1.5 + 12 \left[\frac{l}{\pi \alpha h} \right]^2 \frac{G_{12}}{E_{11}}} \quad (4.3)$$

After experimental studies on E-glass/epoxy composite materials, the ratio $l/\alpha h$ was estimated as 6. Therefore equation 4.3 is transformed to equation 4.4.

$$X_c = \frac{G_{12}}{1.5 + 12\left[\frac{6}{\pi}\right]^2 \frac{G_{12}}{E_{11}}} \quad (4.4)$$

where

$$G_{12} = G_m \frac{G_{f12}(1 + V_f) + G_m(1 - V_f)}{G_{f12}(1 - V_f) + G_m(1 + V_f)} \quad (4.5)$$

and

$$E_{11} = V_f E_f + (1 - V_f) E_m + \frac{4V_f(1 - V_f)G_m(v_{f12} - v_m)^2}{\frac{(1 - V_f)G_m}{K_{f23}} + \frac{V_f G_m}{K_m} + 1} \quad (4.6)$$

G_{12} is the shear modulus of unidirectional composite; l is the wavelength of fiber buckling; h is the thickness of the representative volume element; α is the factor of kink orientation; E_{11} is the longitudinal Young's modulus of unidirectional composite material; K_{f23} is the fiber plain strain bulk modulus; K_m is the matrix plane strain bulk modulus; v_m is the matrix Poisson's ratio; v_{f12} is the Poisson's ratio of the fibers; G_{f12} is the fibers shear modulus.

Xu-Reifsneider Model

Using a beam on elastic foundation model, Reifsneider [1993] predicted the compressive strength of a representative volume of unidirectional composite materials. Fiber/matrix debonding was considered in the model. The expression of the compressive strength according to Xu and Reifsneider model is shown in equation 4.7.

$$\begin{aligned}
X_c &= G_m \left[V_f E_f + \frac{(1 - V_f) E_m}{E_f} \right] \\
&\times \left\{ 2((1 + \nu_m) \sqrt{\frac{\pi \sqrt{\pi} \eta r_f}{3 \frac{E_m}{E_f} \left(V_f \frac{E_m}{E_f} + 1 - V_f \right) (1 + V_f \nu_f + \nu_m (1 - V_f))}} + 1 - \xi \right. \\
&\left. - \frac{\sin \pi \xi}{2\pi} \right\} \tag{4.7}
\end{aligned}$$

where $\xi = 2s/L$ is the matrix slippage percentage; η is the fiber/matrix bond condition parameter that varies from 1 to 2 in psi units ($\eta = 1$ if the fiber is connected to the matrix on one side and $\eta = 2$ if the fiber is connected to the matrix on both sides; s is the matrix slippage length; L is the length of the compression specimen; r_f is the fibers radius; ν_f is the fibers Poisson's ratio.

Lagoudas-Tadibakhsh-Fares model

The expression of the compressive strength given by Lagoudas et al. [1991] is shown in equation 4.8:

$$X_c = G \frac{1 + \frac{\Delta E}{2\pi E} \sin(\pi V_f) [\cos(\pi V_f) - \sqrt{\cos^2(\pi V_f) + 8}]}{1 + \frac{\Delta E}{2\pi E} \sin(\pi V_f) [2 \cos(\pi V_f) - 4 \frac{\Delta E}{\pi E} \sin(\pi V_f)]} \tag{4.8}$$

where $\Delta E = E_f - E_m$; E is the effective stiffness of the lamina; $G = G_m/(1 - V_f)$ is the effective longitudinal shear modulus.

Lagoudas et al. [1991] considered the composite as a heterogeneous material with spatial variation of Young's modulus to simulate the presence of fiber and matrix elements. We note that his analysis was based on 2D simulations.

Budiansky model

The expression proposed by Budiansky [1983] for compressive strength prediction of composites is an extension to Rosen's work and is given by equation 4.9

$$X_c = \frac{G}{1 + \bar{\phi}/\gamma_y} \quad (4.9)$$

$\bar{\phi}$ is the initial fiber misalignment angle; γ_y is the matrix yield strain

Lagoudas-Saleh model

In their analysis, Saleh et al. [1993] considered that the kink is initiated at the free edge or from some other weak point. The behavior of the matrix in the kinking zone is considered as plastic and shear-lag model was used to determine the strain rate energy of the fully kinked strip. The expression of the compressive strength of the composite is given by equation 4.10.

$$X_c = \frac{2V_f E}{\pi d_f L} (\sigma_{ym} \theta_K l_K^2 + 2\pi d_f g_f) \quad (4.10)$$

where d_f is the fibers diameter; σ_{ym} is the yield stress of the matrix; θ_K is the angle of Kink rotation; l_K is the kink zone length; g_f is the fibers critical energy release rate corresponding to bending.

The compressive strengths predicted by the previously mentioned models were compared to experimental data. Naik and Kumar [1999] performed a comparison between theoretical and experimental values of the compressive strength X_c for E-glass fibers and for T300 carbon fibers. Table 4.1 summarizes the values recommended by the authors for compressive strength at the macroscopic scale for composites reinforced with E-glass fibers for different values of fiber volume fraction V_f . Table 4.2 summarizes the values recommended by the authors for compressive strength at the macroscopic scale for T300 carbon fiber for different values of fiber volume fraction V_f .

Fiber volume fraction V_f	0.3	0.37	0.46	0.55
Corresponding longitudinal compressive strength X_c(MPa)	583	555	673	475

Table 4.1: Compressive strength for UD composites reinforced with E-glass fibers. Naik and Kumar [1999]

Fiber volume fraction V_f	0.55	0.59	0.62	0.65	0.66	0.70
Corresponding longitudinal compressive strength X_c(MPa)	1570	1228	1516	1585	1508	1500

Table 4.2: Compressive strength for UD composites reinforced with T300 carbon fibers. Naik and Kumar [1999]

Moreover, Naik and Kumar [1999] also presented a comparison between all the previously mentioned models and experimental data. Figure 4.3 shows the evolution of the compressive strength of GFRPs with the fiber volume fraction V_f for the models previously cited and using experimental data. Figure 4.4 shows the same type of curves but for CFRPs.

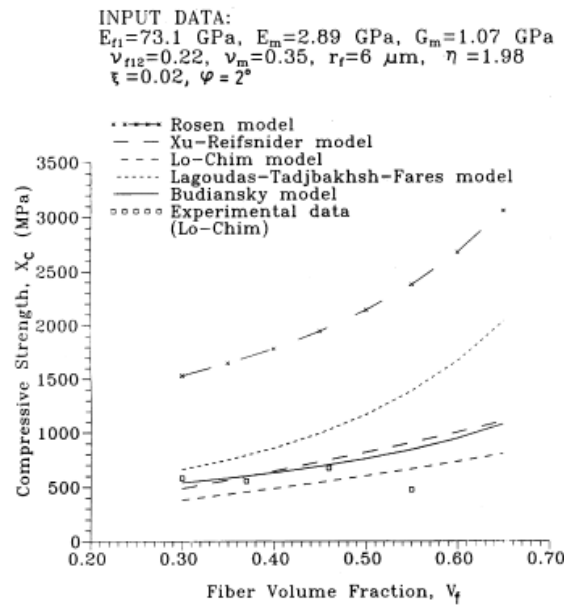


Figure 4.3: Comparison of different models for compressive strength estimation for E-glass fibers. Naik and Kumar [1999]

INPUT DATA:
 $E_f=221$ GPa, $E_m=4$ GPa, $G_m=1.48$ GPa
 $\nu_{f12}=0.20$, $\nu_m=0.35$, $r_f=3.5$ μm , $\eta=1.98$
 $\xi=0.02$, $\varphi=2^\circ$

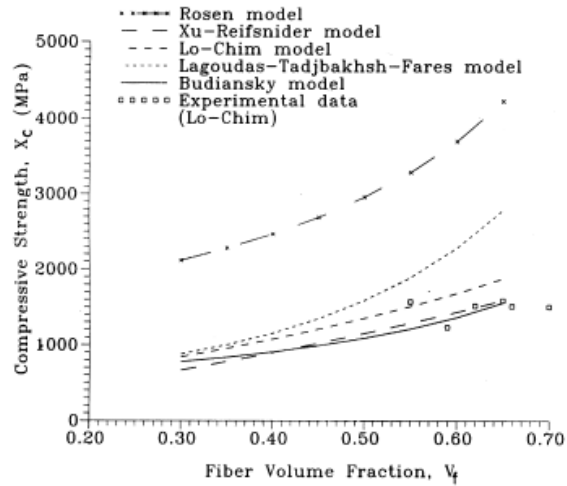


Figure 4.4: Comparison of different models for compressive strength estimation for T300 carbon fibers. Naik and Kumar [1999]

Naik and Kumar [1999] concluded that the Lo and Chim [1992] model for compressive strength predictions of composites is reliable. The compressive strength values predicted by the Lo and Chim [1992] model were found in good agreement with experimental data. Moreover, Naik and Kumar [1999] signaled that the Rosen shear mode over predicts the strength for both types of reinforcement (glass and carbon).

The values computed by Lo and Chim [1992] for the compressive strength of UD composites reinforced with P122 glass fibers and T300 carbon fibers will be considered in this thesis when bending loads are analyzed.

The current chapter has the following structure. In section 4.2, the behavior of FRPs under bending loads is presented. In parallel to bending, the influence of adding a shear stress to tension load on the creep behavior of UD composites is detailed in section 4.3.

4.2 Response of FRPs to bending loads

In previous chapters, the ultimate tensile strength of FRPs was estimated using shear-lag equations and with the Finite Element method. Furthermore, creep tests were performed under different load levels and the long term behavior of the FRPs was monitored. In this part of the work we introduce bending loads and we perform static and creep tests in order to assess the behavior of FRPs to such type of loading. The calibrated micromechanical model based on the

Finite Element method is used for the simulations. We apply tension and compression loads on the right edge of the specimen in order to simulate the presence of a bending moment (see Figure 4.5).

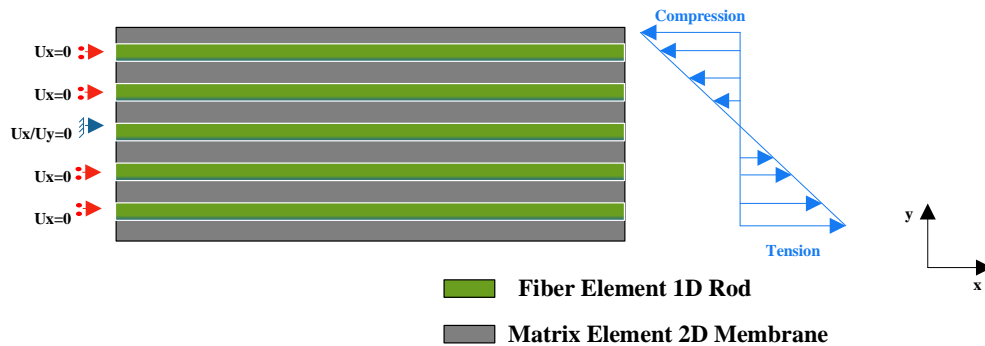


Figure 4.5: Theoretical basis of the model for bending analysis

The behavior of the fibers is linear and elastic and the behaviors considered for the matrix element are linear elastic with fiber matrix debonding for static test and viscoelastic for creep tests. Due to the bending moment, part of the fibers will be subjected to compression load while others will be subjected to tension. The maximum compression load that the fibers may sustain before rupture that was considered in the calculations was based on the literature review on the compressive strength of unidirectional composite materials that was presented in section 4.1. According to Greszczuk [1975], the maximum fiber compression stress (Critical stress) is related to the composite compressive strength (at the macro scale) with equation 4.11:

$$X_c = V_f \times \sigma_{c_f} \quad (4.11)$$

where X_c is the composite compressive strength at the macroscopic scale; σ_{c_f} is the maximum compression stress supported by the fibers.

Therefore, we calculate the maximum compression stress supported by the fibers using equation 4.11 and with reference to Tables 4.1 and 4.2 (Tables 4.1 and 4.2 summarizes the compressive strength values X_c for glass and carbon fibers). The maximum fiber stress in compression considered for P122 glass fiber is 860 MPa and for T300 carbon fiber is 2900 MPa. When it comes to tension resistance of fiber elements, Weibull law was consider in the same manner that was described in chapters 2 and 3 (see Figure 4.6 for the fibers tensile strength distribution for a given specimen).

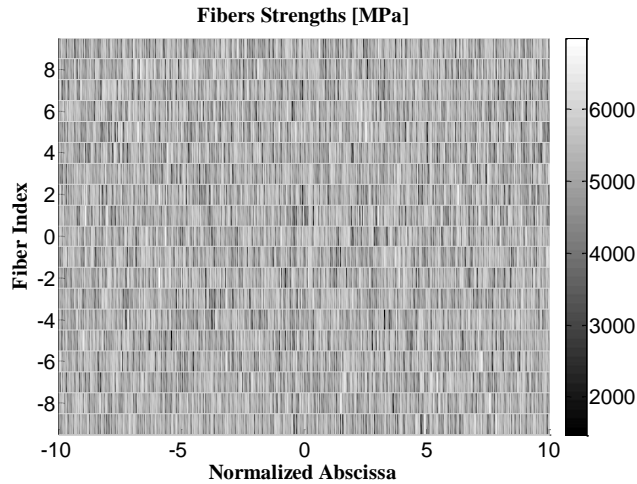


Figure 4.6: Fibers tensile strengths for a given specimen composed of 19 fibers

The parameter of interest in the analysis is the number of fiber breaks. In the first analysis we considered a composite reinforced with P122 glass fibers subjected to the triangular load distribution on its right edge (see Figure 4.5). Figure 4.7 shows the evolution of the number of fiber breaks versus the maximum applied stress at the upper or lower edge (as tension or compression since its equal but with a sign difference) for P122 glass fibers.

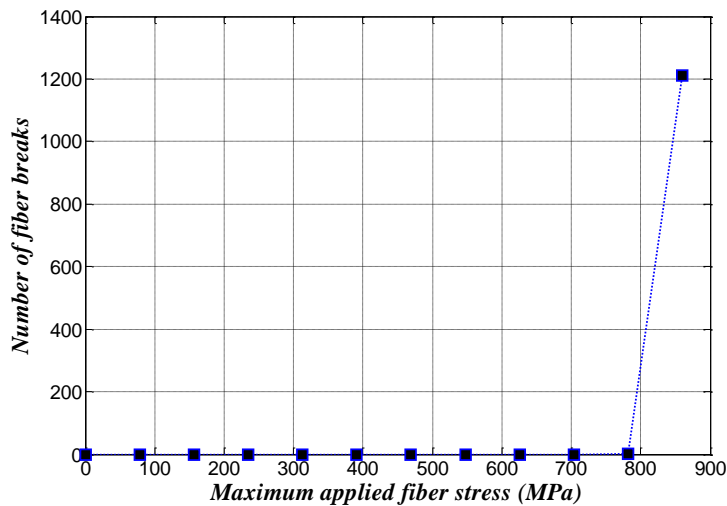


Figure 4.7: Number of fiber breaks versus maximum applied fiber stress for P122 glass fibers

Figure 4.7 shows that the maximum fiber stress supported by the composite is 860 MPa. When the fiber stress reaches 860 Mpa, the compression stress in the fibers at the upper edge of the specimen reaches the maximum/critical compression stress that fibers can support. This fact led to the high increase in the number of fiber ruptures which induced the rupture of the specimen. Therefore, the maximum stress supported by the composite is controlled by the compression

strength of P122 glass fibers, which is 860 MPa. Figure 4.8 shows the evolution of the number of fiber breaks versus the maximum applied stress at the upper or lower edge (as tension or compression since its equal but with a sign difference) for T300 carbon fibers.

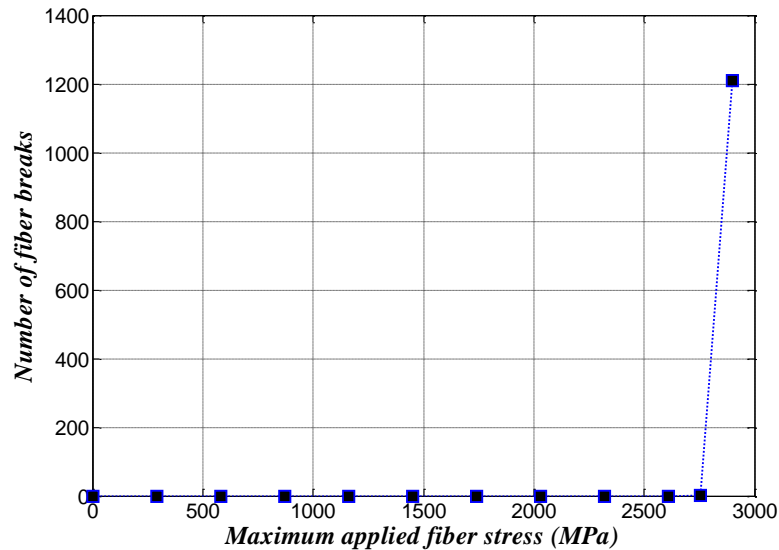


Figure 4.8: Number of fiber breaks versus maximum applied fiber stress for T300 carbon fibers

The evolution of the number of fiber breaks with the maximum applied fiber stress shows also the rupture of the specimen at a stress level of 2900 MPa. Therefore the maximum stress supported by the composite is controlled by the compression strength of T300 carbon fibers which is 2900 MPa.

Creep tests were also performed at load levels of 70% and 80% of the ultimate bending strength for both types of fiber reinforcement (glass and carbon). No creep was observed at the considered load levels.

4.3 Combined shear and tension

In this section we study the behavior of the unidirectional composites under combined tension and shear loading. The aim of the calculation performed herein is to verify the role of the matrix element in the creep of composites. As a matter of fact, adding an additional shear stress to tension loads stimulates directly the matrix elements. Kotelnikova-Weiler[2012], performed creep tests on unidirectional composites under pure tension loads and under combined tension and torsion loads. Kotelnikova-Weiler[2012] reported that creep was accelerated when torsion was combined with the tension load. The aim of these calculations is to verify the tendency obtained by experimental results with the theoretical models. In the current simulations, the

tension load/imposed displacement will be applied at the right edge of the specimen and will be combined to constant shear stress (see Figure 4.9). The influence of the applied shear stress on the ultimate tensile strength and on the long term behavior will be investigated.

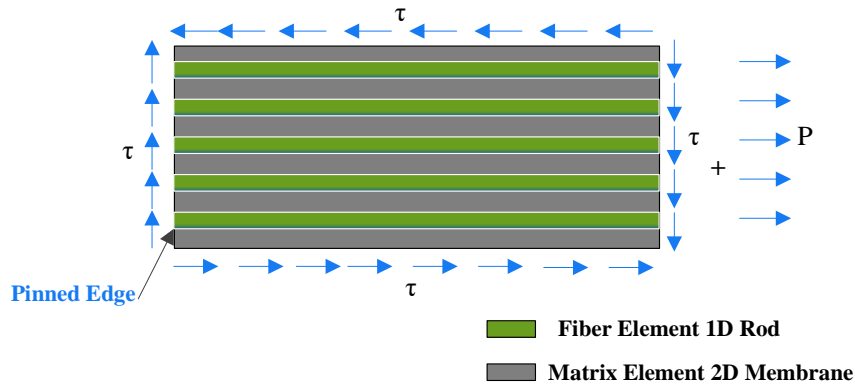


Figure 4.9: Combining tension and shear

The simulations performed are for P122 glass fibers. The simulation parameters are previously summarized in Table 2.2. Several load levels are considered for the shear stress, 20%, 50%, 60% and 70% of the maximum value of shear stress at fiber/matrix debonding. We note that for ultimate tensile strength estimation tests, the simulations are performed with imposed displacement at the right edge instead of imposed fiber load P. However, for creep tests, a constant load P is imposed on the right edge of the specimen and the long term behavior of the composite is monitored. Figure 4.10 shows the stress/strain curve for the P122 glass fibers when the 20% of shear stress was combined with imposed displacements.

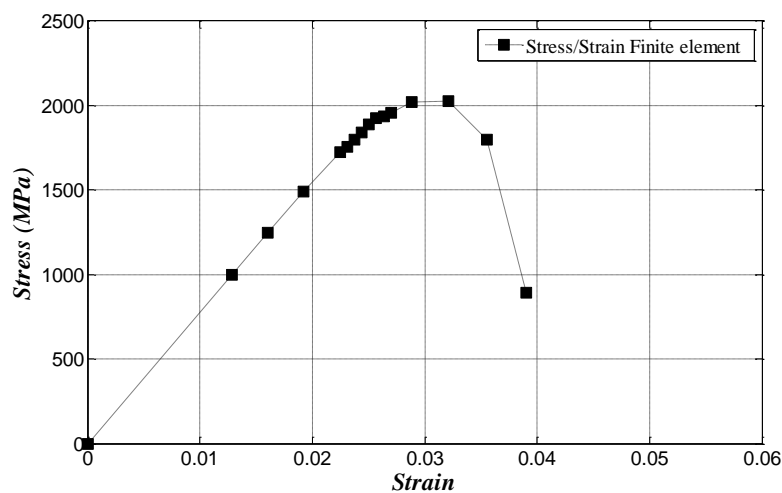


Figure 4.10: Stress/Strain curve for combined tension and 20% of shear stress (P122 glass fibers)

Figure 4.10 shows that the maximum tension load supported by the specimen is 2020 MPa. The additional shear stress induced a slight reduction to the ultimate tensile stress of the specimen (the value with pure tension was 2050 MPa). Figure 4.11 shows the stress/strain curve for the P122 glass fibers when 50% of shear stress was considered in the analysis.

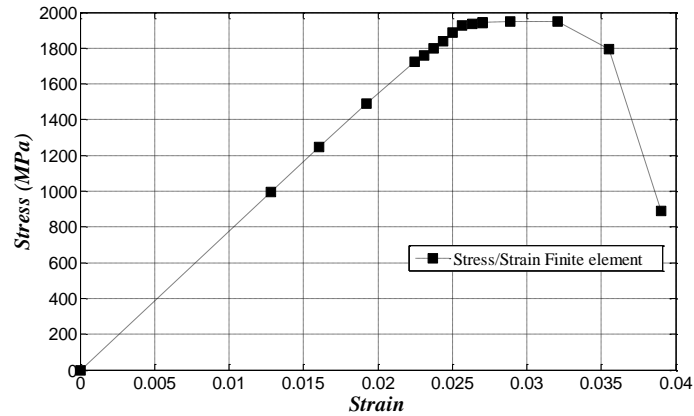


Figure 4.11: Stress/Strain curve for combined tension and 50% of shear stress (P122 glass fibers)

Figure 4.11 shows that the ultimate tensile strength (1950 MPa) when 50% of shear stress is combined to tension is slightly lower than the one calculated when pure tension was applied (2050MPa). We note that when 60% of shear stress was considered, the stress strain curve practically coincided with the one of 50% shear. Figure 4.12 shows the stress/strain curve for the P122 glass fibers when 70% of shear stress was considered in the analysis.

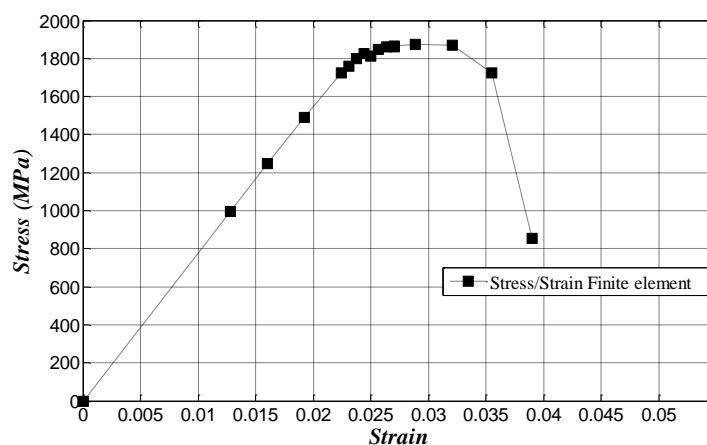


Figure 4.12: Stress/Strain curve for combined tension and 70% of shear stress (P122 glass fibers)

Figure 4.12 shows that the ultimate tensile strength (1870 MPa), when 70% of shear stress is combined to the tension load, is lower than the one calculated when pure tension was applied (2050MPa).

Creep tests are performed at a load level of 70% of the ultimate tensile strength for the four levels of shear stress (20%, 50%, 60% and 70%). Figure 4.13 and Figure 4.14 show the curves of the evolution of the deformation and the apparent modulus with time for the four load cases considered (pure tension, tension+20% shear, tension+50% shear, tension+60% shear, tension+70% shear). The curves of pure tension and tension+20% shear practically coincide. Therefore these two load cases show similar behavior since the applied shear stress is at a low level (20%). The creep is slightly accelerated when considering the 50%/60% additional shear stress while it is considerably accelerated when a value of 70% of shear is considered in the calculations.

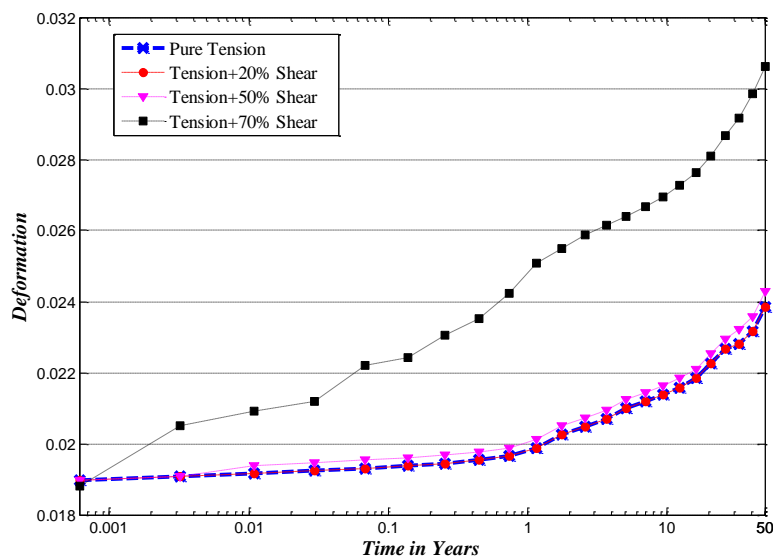


Figure 4.13: Deformation evolution with time, with and without shear stress

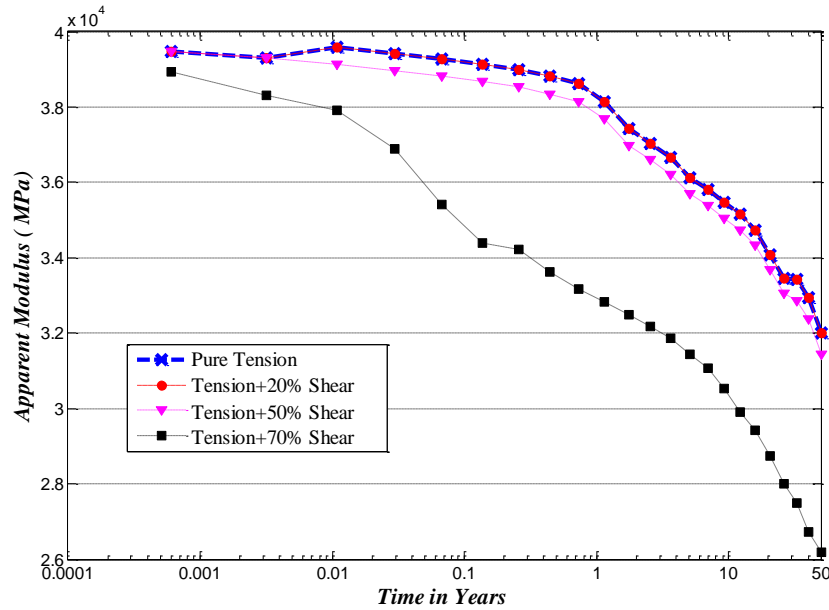


Figure 4.14: Apparent modulus evolution with time, with and without shear stress

4.4 Conclusion

The mechanical behavior of unidirectional composite materials under several load patterns (compression, bending, shear and tension) was analyzed in this chapter. Shear-lag and Finite Element based micromechanical models were used for this purpose. Short- and long-term tests were performed on unidirectional composite that are subjected to bending loads for several types of reinforcing materials. The simulations performed showed that the maximum compressive stress that fibers can support highly controls the behavior of the overall composite under bending loads. At the matter of fact, the resistance of fibers to compression is much smaller than their tensile strength. This fact led to the high increase in the calculated number of fiber breaks when the applied load reached the fiber's compressive strength at the compressed part of the section subjected to bending. We note that no creep was observed at 70% and 80% of the bending strength for GFRPs and CFRPs when using this type of micro mechanical approach. The influence of an additional shear stress on the creep of composites subjected to tension loads was also investigated. The creep of the tested specimens was accelerated when a considerable value of shear stress was applied. The simulations performed were found in good agreement with the experimental work of Kotelnikova-Weiler[2012] on the creep test of composites that are subjected to tension and shear loads.

Conclusion

Summary on the achieved objectives

Advantages of composite materials need no more presentation. Their ability to combine light weight, anisotropy and high performances are well known and their scope of applications is currently covering a wide range of fields from highly specialized aeronautical to widely spread civil engineering and construction. However, in the civil engineering domain, composite materials are usually combined with more traditional materials such as steel or concrete. Their use as main load bearing elements in structural applications remains strongly dependent on the durability studies and construction of valid models capable of predicting with a sufficiently high level of confidence the lifespan of a given structure built with composites. It is worth emphasizing that experimental studies that help in the comprehension of the mechanical behavior of such materials are extremely expensive and time consuming. Numerical simulations and modeling are therefore essential in understanding the composites short- and long-term response to any given load.

In this research work we developed and enhanced numerical tools that allow simulating the creep of composite materials under any given load. In order to simulate tension loads, a numerical tool that was established during the thesis of Kotelnikova-Weiler [2012] was developed, enhanced and validated. Proper boundary conditions were introduced to the existing model, such as periodic boundary conditions. At the matter of fact, periodic boundary conditions are essential to eliminate the boundary layer effects due to the long range interaction of fibers after breakage. A parametric analysis was also conducted on the shear-lag model which helped on verifying all the assumptions that were considered by Beyerlein et al.[1998] and Kotelnikova-Weiler [2012]. The performed analysis led to the proper evaluation of the size of the representative volume element (RVE) of the composite (mesh size, number of fibers, length of the specimen, etc...). Furthermore, the results obtained from the shear lag-model were validated with a comparative study to the Finite Element technique. On the contrary to the enhanced shear-lag model, the Finite Element model is capable of analyzing several types of loading patterns such as tension, compression, bending and shear. In addition, the Finite Element model can simulate the progressive evolution of fiber breakage and fiber/matrix debonding which was not modeled in previous research works (Blassiau et al. [2007]). It is worth mentioning that on the contrary to the work of Kotelnikova-Weiler [2012], MonteCarlo simulations were performed in this research work. The importance of such types of simulations relies in the fact that one generated specimen (one realization) could not represent the behavior

of the composite. Having calibrated the two micromechanical models, creep tests were conducted on composites reinforced with glass fibers (GFRPs) and with carbon fibers (CFRPs). The ultimate tensile strength was also assessed using both modeling techniques (shear-lag and Finite Element). Composites reinforced with carbon fibers presented a higher tensile strength than the ones reinforced with glass fibers. And as far as it concerns long term considerations, CFRPs presented better creep behavior than GFRPs. For the composites reinforced with glass fibers, creep rupture was observed at a load level of 80% of the ultimate tensile strength. However, for both types of composites (GFRPs/CFRPs) no creep was observed at load levels lower than 70% of the ultimate tensile strength. Bending loads were also analyzed. When a bending moment is applied on the unidirectional composite, parts of the fibers are subjected to tension while others are subjected to compression. Since the resistance of fibers to compression is much lower than the one in tension, it highly controlled the bending behavior of the composite. The simulations showed that when the compression loads in the fibers located at the upper part of the specimens reached the ultimate compressive strength at the fiber scale, the number of the fiber breaks increased rapidly leading to the rupture of the specimen. The influence of combining a shear stress to tension load on creep was also assessed. The simulations showed that when a considerable shear stress is combined with tension load, the creep of the composite is accelerated and its tensile strength decreases.

Perspectives

This thesis contributed to the development of two robust micro mechanical models that help in evaluating the creep of unidirectional composites subjected to different loading patterns. The first model is based on shear-lag considerations while the second is developed using the Finite Element software Abaqus. An upgrade of the existing 2D models to 3D configuration is possible in the future. An additional calibration to the developed models could be performed by comparing their results to experimental studies. The existing models can be developed to simulate kink band rupture modes for composites subjected to compression loads. Moreover, the creep of composites under compression loads can be also implemented in the models.

Appendix A

Comparative study between the developed numerical models and the work of Beyerlein et al.[2001]

We perform simulations on 2D unidirectional composites subjected to compression load using the enhanced shear lag model. The overstress factors due to a single fiber break at the center of the composite are assessed. In order to perform such task, the equations of the shear-lag model used for tension calculation presented in chapter 2 are to be changed in order to take into account the variation in the load direction. Beyerlein et al.[2001], in their study on unidirectional composites subjected to compression load highlighted the necessary modifications to be applied on the equations used for tension calculation. The description of the model for compression calculation is presented below.

The discretization of the representative volume remains the same as shown in Figure 2.1 of chapter 2. The only difference is that the load considered in the current analysis is a compression load instead of tension (see Figure A.1)

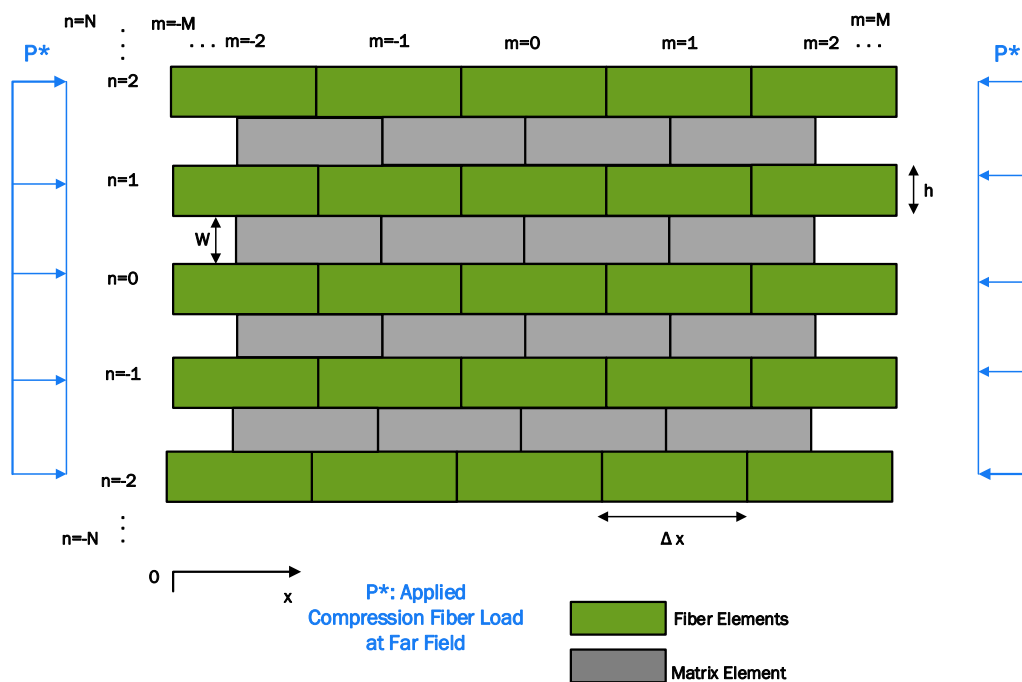


Figure A.1: Model discretization for compression analysis (shear-lag method)

Remaining in the same conditions of the previous chapters, the axial stiffness of the matrix is neglected and the fiber elements are considered as the load bearing members. Therefore, the

fibers will sustain the entire load and will not deform in shear. Also transverse displacements are neglected.

The following modification needs to be performed to the shear-lag equations showed in chapter 2:

The normalized coordinate ξ can be written with the following expression:

$$\xi = \frac{x}{\sqrt{\frac{wE_f A}{Gt_l}}} \quad (\text{A. 1})$$

where x is the longitudinal coordinate; E_f is the fibers Young's modulus; w is the matrix band width; G is the matrix shear modulus; t_l is the lamina thickness; A is the fibers cross section.

The normalized fiber displacement U_n can be written with equation A.2:

$$U_n(\xi) = \frac{u_n(x)}{p^* \sqrt{\frac{w}{E_f A G t_l}}} \quad (\text{A. 2})$$

where u_n is the fibers axial displacement; p^* is the compression load.

As per the work of Beyerlein et al.[2001], the solution of the problem of a unidirectional composite subjected to compression load at the far field with a unique fiber break at its center can be written as a superposition of the solutions of a unloaded composite subjected to a tension load at its center (auxiliary problem A1, see Figure A.3) with the one of an intact composite subjected to a compression load at the far field (see Figure A.2).

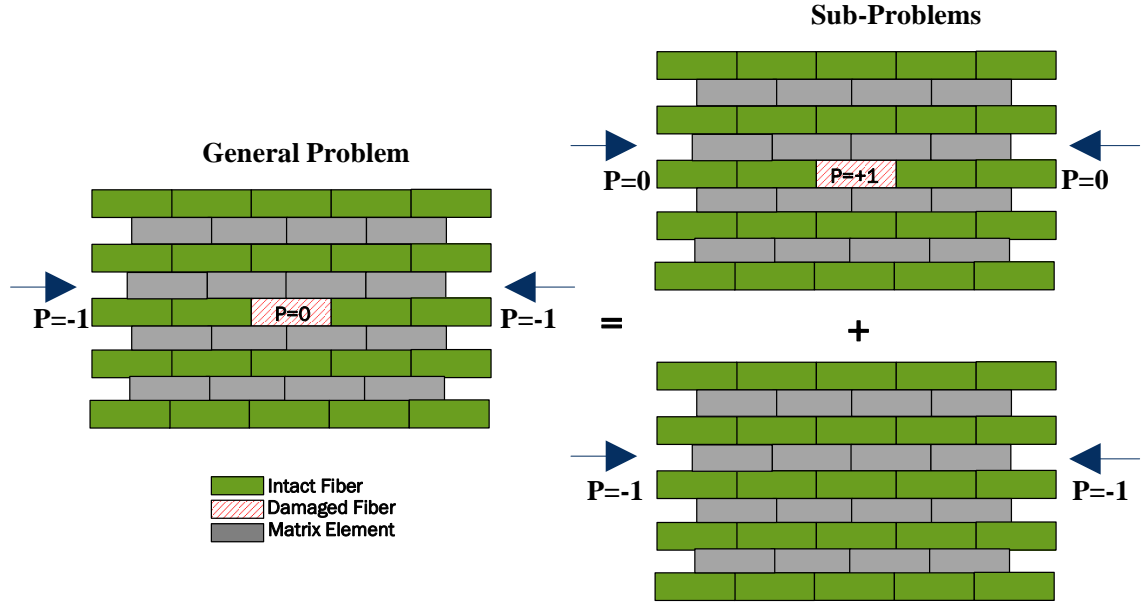


Figure A.2: Superposition principle

The stress/strain fields due to a unit tensile load applied to the break site in an unloaded composite need to be calculated. Under the auxiliary boundary conditions, the expressions of the fiber axial loads and displacements, $L_n^{u,s}$ and $V_n^{u,s}$ are:

$$L_n^{u,s}(\xi) = \frac{1}{2} \times \int_0^\pi \cos(n\theta) C_\theta \exp(-2C_\theta |\xi|) d\theta \quad (\text{A. 3})$$

$$V_n^{u,s}(\xi) = -\frac{\text{sgn}(\xi)}{4} \int_0^\pi \cos(n\theta) \exp(-2C_\theta |\xi|) d\theta \quad (\text{A. 4})$$

Where $\text{sgn}(\xi) := \begin{cases} -1 & \text{if } \xi < 0 \\ 0 & \text{if } \xi = 0 \text{ and } C_\theta = \sin(\frac{\theta}{2}) \\ 1 & \text{if } \xi > 0 \end{cases}$

The normalized matrix shear stress can be written with the following equation:

$$\begin{aligned} T_n^{u,s}(\xi) &= V_{n+1}^{u,s}(\xi) - V_n^{u,s}(\xi) \\ &= -\frac{\text{sgn}(\xi)}{4} \times \int_0^\pi (\cos((n+1)\theta) - \cos(n\theta)) \exp(-2C_\theta |\xi|) d\theta \end{aligned} \quad (\text{A. 5})$$

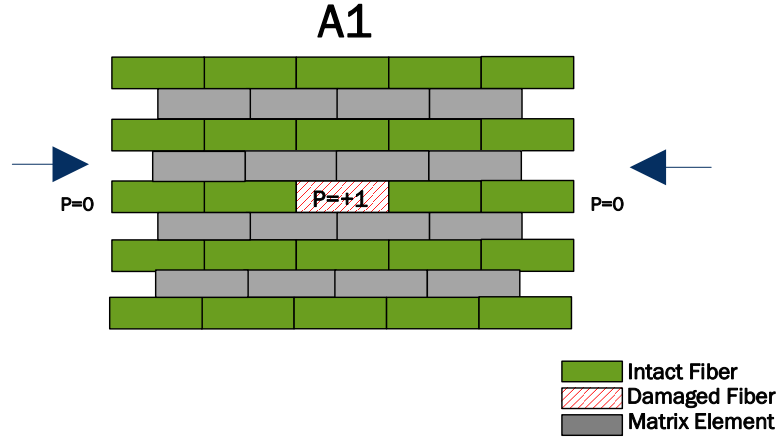


Figure A.3: Auxiliary problem A1 of a central fiber break under tension load

Therefore the solution of the general problem can be written:

$$P_n(\xi) = L_n^{u,s}(\xi) - 1 \quad \text{The fiber's axial stress} \quad (\text{A. 6})$$

$$U_n(\xi, t) = V_n^{u,s}(\xi) - \xi \quad \text{The fiber's axial displacement} \quad (\text{A. 7})$$

We note that the matrix shear stress expression remains unchanged.

In comparison to the work of Beyerlein et al.[2001], we calculated the overstress factors due to a fiber break in the central part of the composite using the calibrated shear lag model and also with the developed micromechanical Finite Element model. Figure A.4 shows the evolution of the normalized compressive axial stress in the neighboring intact fibers to the break site calculated by solving equation A.6. When comparing Figure A.4 (curve in red $n=1$ for the first intact fiber) with the results presented by Beyerlein et al.[2001], (Figure A.5) good agreement was found. Moreover, we report that good agreement was found between the shear-lag model and the Finite Element model. Table A.1 presents the overstress factors calculated with shear-lag equations and with Finite Element method.

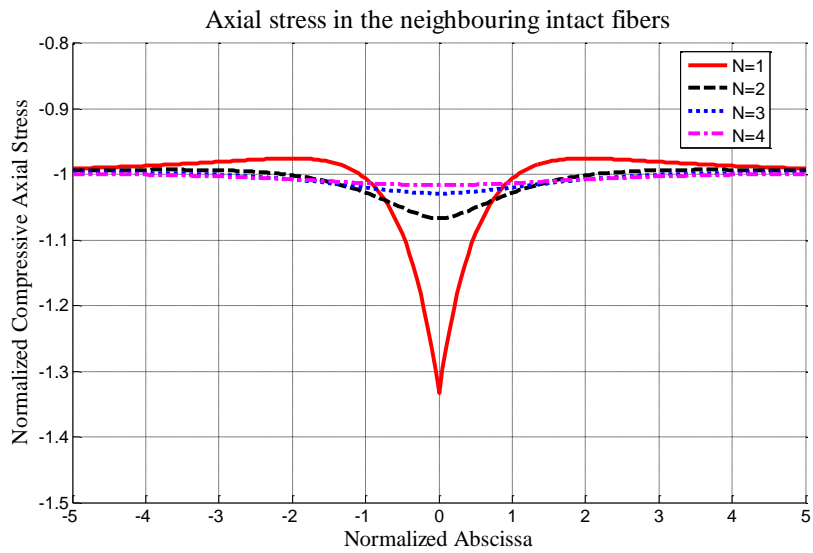


Figure A.4: Normalized compressive fiber axial stress calculated with the shear-lag model

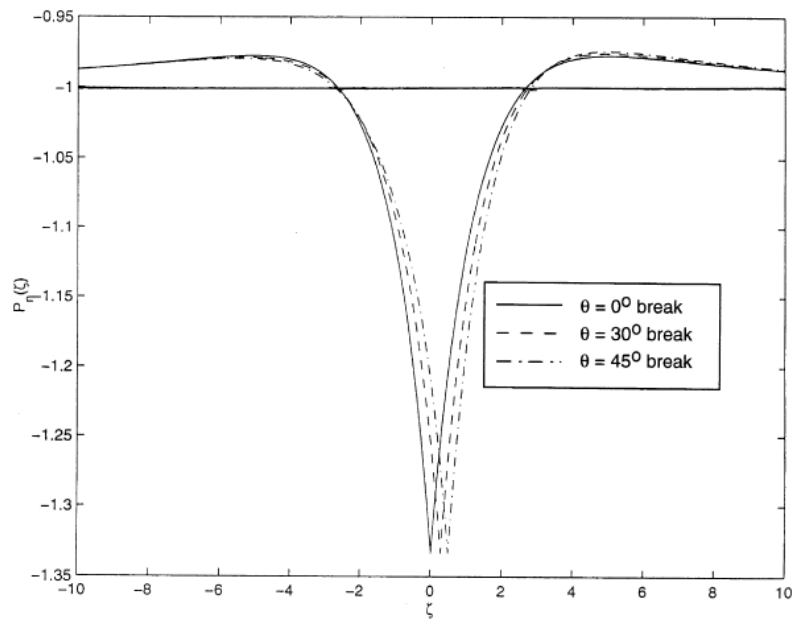


Figure A.5: Normalized fibers compressive axial stress in the first intact fiber. Beyerlein et al.[2001]

Intact fiber's number	1	2	3	4
Overstress factor (Shear-lag)	1.33	1.067	1.029	1.016
Overstress factor (Finite Element)	1.36	1.062	1.031	1.02

Table A.1: Overstress factors (in compression) shear-lag vs. Finite Element

Bibliography

- H.L.Cox. 1952. The Elasticity and Strength of Paper and Other Fibrous Materials. *British Journal of Applied Physics*. 3(3):72–79.
- I.J Beyerlein, S.L. Phoenix, and Rishi Raj. 1998. Time Evolution of Stress Redistribution around Multiple Fiber Breaks in a Composite with Viscous and Viscoelastic Matrices. *International Journal of Solids and Structures*. 35(24):3177–3211.
- Natalia Kotelnikova-Weiler. 2012. Optimisation mécanique et énergétique d'enveloppes en matériaux composites pour les bâtiments. PhD Thesis. Université Paris-Est.
- M. R. Nedele and M. R. Wisnom. 1994. Stress Concentration Factors around a Broken Fibre in a Unidirectional Carbon Fibre-Reinforced Epoxy. *Composites Science and Technology* 25(7):549–57.
- S. Blassiau, A.R. Bunsell and A. Thionnet. 2007. Damage Accumulation Processes and Life Prediction in Unidirectional Composites. *Proceedings of the Royal Society*. 463(2080):1135–52.
- L. Du Peloux, F. Tayeb, J.F. Caron and O. Baverel. 2015. The Ephemeral Cathedral of Creteil: a 350m² lightweight gridshell structure made of 2 kilometers of GFRP tubes. CIGOS 2015: Innovations in Construction, Cachan, France.
- V.M. Karbhari et al. 2003. Durability Gap Analysis for Fiber-Reinforced Polymer Composites in Civil Infrastructure. *Journal of Composites for Construction*. 7(3):238.
- Chi-Hung Shen; George S. Springer. 1977. Environmental Effects on the Elastic Moduli of Composite Materials. *Journal of Composite Materials*. 11(3): 250-264.
- T. S Grant and W. L. Bradley. 1995. In-Situ Observations in SEM of Degradation of Graphite Epoxy Composite Material. *Journal of Composite Materials*. 29 (7) 852-867.
- C.H. Shen, and G.S. Springer 1976. Moisture absorption and desorption of composite materials. *Journal Of Composite Materials*, 10: 2–20.12.
- G.Marom. 1989. Environmental Effects on Fracture Mechanical Properties of Polymer Composites. *Elsevier Science Publishers*. P.397-423

- Stony Brook. 2002. Degradation of Carbon Fiber-Reinforced. *Journal of Composite Materials*. 36(24):2713–33.
- M. Rakin, B. Medjo and M. Stamenovic. 2011. Effect of Alkaline and Acidic Solutions on the Tensile Properties of Glass – Polyester Pipes. *Materials and Design*. 32:2456–61.
- Hiroyuki Kawada and V. K. Srivastava. 2001. The Effect of an Acidic Stress Environment on the Stress-Intensity Factor for GRP Laminates. *Composite Science and Technology*. 61:1109–14.
- Tim Osswald. 2010. Understanding Polymer Processing.
- D.Ferry. 1955. The Temperature Dependence of Relaxation Mechanisms in Amorphous Polymers and Other Glass-forming Liquids. *Journal of the American chemical society*. 77 (14): 3701–3707.
- K. G. N. C. Alwis and C. J. Burgoyne. 2006. Time-Temperature Superposition to Determine the Stress-Rupture of Aramid Fibres. *Applied Composite Materials*. 13(4):249–64.
- Y Miyano, M. Nakada and H. Cai. 2008. Formulation of Long-Term Creep and Fatigue Strengths of Polymer Composites Based on Accelerated Testing Methodology. *Journal of Composite Materials*. 42(18):1897–1919.
- W.N. Findley, and G. Khosla. 1956. An equation for tension creep of three unfilled thermoplastics. *SPE Journal*, Vol. 12, No. 12, pp. 20-25.
- W.N. Findley, D.E. Peterson. 1958. Prediction of long time creep with ten year creep data on four plastic laminates. *Proceeding, ASTM*. Vol 58. P841.
- K.H. Boller. 1965. EFFECT OF LONG-TERM LOADING ON GLASS-REINFORCED PLASTIC LAMINATES . *Forest Products Laboratory*. (2039).
- D. A. DILLARD, M. R. STRAIGHT and H. F. BRINSON. 1987. The Nonlinear Viscoelastic Characterization of Graphite/Epoxy Composites. *Polymer Engineering and Science*. 27(2) 116-123
- Shing-Chung Yen and Fay L. Williamson. 1990. Accelerated Characterization of Creep Response of an off-Axis Composite Material. *Composites Science and Technology* 38(2):103–18.

- L.C Bank and A. S. Mosallam. 1992. Creep and Failure of a Full-Size Fiber-Reinforced Plastic Pultruded Frame. *Composites Engineering*. 2(3):213–27.
- R.A. Schapery. 1969. On the Characterization of Nonlinear Viscoelastic Materials. *Polymer Engineering and Science*. 9(4):295–310.
- Y.C. Lou, and R. A. Schapery. 1971. Viscoelastic Characterization of a Nonlinear Fiber Reinforced Plastic. *Journal of Composite Materials*. 5:208-234.
- B. Abdel-Magid, R.Lopez-Anido, G. Smith and S.Trofka. 2003. Flexure creep properties of E-glass reinforced polymers. *Composite Structures*. 62(3-4):247-253.
- N. Lissart and J. Lamon. Statistical Analysis of Failure of SiC Fibres in the Presence of Bimodal Flaw Populations. *J Mater Sci*. 1997;32:6107-17
- W. Weibull. A statistical distribution function of wide applicability. *Journal of Applied Mechanics*. 1951;18:253.
- A.Kouadri-boudjelthia , A. Imad, A. Bouabdallah, and M. Elmeguenni. 2009. Analysis of the Effect of Temperature on the Creep Parameters of Composite Material. *Materials and Design*. 30(5):1569–74.
- J.M. Hedgepeth. 1961. Stress concentrations in filamentary structures. Report, NASA TN D-882, Langley Research Center.
- John M. Hedgepeth and, Peter Van Dyke. 1967. Local Stress Concentrations in Imperfect Filamentary Composite Materials. *Journal of Composite Materials*. 1(3):294–309.
- D.C. Lagoudas, Chung-Yuen Hui and S. Leig. Phoenix. 1989. Time Evolution of Overstress Profiles near Broken Fibers in a Composite with a Viscoelastic Matrix. *International Journal of Solids and Structures*. 25(1):45–66.
- Shojiro Ochiai, Karl Schulte, Piet W.M. Peters. 1991. Strain concentration factors for fibers and matrix in unidirectional composites. *Composites Science and Technology*. 41(1991): 237-256.
- A. M. Sastry and S. L. Phoenix. 1993. Load Redistribution near Non-Aligned Fibre Breaks in a Two-Dimensional Unidirectional Composite Using Break-Influence Superposition. *Journal of Materials Science Letters*. 12(20):1596–99.

- A. Thionnet and J. Renard. 1998. Multiscale analysis to determine fiber/matrix debonding criteria in SiC/titanium composites with and without consideration of the manufacturing residual stresses. *Composites Science and Technology*. 58(6):945–955.
- Xia, Zihui, Yu Chen, and Fernand Ellyin. 2000. A Meso/micro-Mechanical Model for Damage Progression in Glass-Fiber/epoxy Cross-Ply Laminates by Finite-Element Analysis. *Composites Science and Technology*. 60(8):1171–79.
- I. J. Beyerlein, S. L. Phoenix, and Ann Marie Sastry. 1996. Comparison of Shear-Lag Theory and Continuum Fracture Mechanics for Modeling Fiber and Matrix Stresses in an Elastic Cracked Composite Lamina. *International Journal of Solids and Structures*. 33(18):2543–74.
- B. Fiedler, M. Hojo, S. Ochiai, K. Schulte, and M. Ando. 2001. Failure Behavior of an Epoxy Matrix under Different Kinds of Static Loading. *Composite Science and technology*. 61:1615– 24.
- J. Koyanagi, H. Hatta, F. Ogawa, and H. Kawada. Time dependent reduction of tensile strength caused by interfacial degradation under constant strain duration in ud-cfrp. *Journal of Composite Materials*. 41(25) : 3007 3026, 2007.
- John E.Ullmann. A Review of: ‘ STATISTICS OF EXTREMES ’. Columbia University Press New York , 1958-375.
- N. Bonora. 2000. On the Dependence of the Weibull Exponent on Geometry and Loading Conditions and Its Implications on the Fracture Toughness Probability Curve Using a Local Approach Criterion. *International Journal of Fracture*. 104:71-87
- S. Gerguri, L.J. Fellows, J.F. Durodola, N.A. Fellows, A.R. Hutchinson, T. Dickerson. Prediction of Brittle Failure of Notched Graphite and Silicon Nitride Bars. *Applied Mechanics and Materials*. (1-2):113-120, 2004
- R. Danzer and P. Supancic. 2007. Fracture Statistics of Ceramics – Weibull Statistics and Deviations from Weibull Statistics. *Engineering Fracture Mechanics*. 74:2919–32.
- M. T. Todinov,.2009. Is Weibull Distribution the Correct Model for Predicting Probability of Failure Initiated by Non-Interacting Flaws? *International Journal of Solids and Structures* 46(3-4):887–901.
- H.Peterlik and D. Loidl. 2001. Bimodal Strength Distributions and flaw Populations of

- Ceramics and Fibres. *Engineering Fracture Mechanics*. 68:253–61.
- Dieter Loidl, Oskar Paris, H. Rennhofer, Martin Mu and Herwig Peterlik. 2007. Skin-Core Structure and Bimodal Weibull Distribution of the Strength of Carbon Fibers. *Carbon* 45:2801–5.
- Cédric Thomas, Fabien Nony and Stéphane Villalonga. 2011. Endommagement de Structures Composites à Matrice Thermoplastique : Application Au Stockage D'Hydrogène Gazeux Sous Haute Pression Damages. *JNC 17*.
- P. Zinck. 2011. Sample Size Dependence of Flaw Distributions for the Prediction of Brittle Solids Strength Using Additive Weibull Bimodal Distributions. *Engineering Fracture Mechanics* 78(6):1323–27.
- C. Baxevanakis, D. Jeulein, B. Lebon and J. Renard. Fracture statistics modeling of laminate composites. *International Journal of Solids and Structures*. 1998;35(19):2505-2521.
- B. Nedjar, N. Kotelnikova-Weiler and I. Stefanou. 2014. Modeling of Unidirectional Fibre-Reinforced Composites under Fibre Damage. *Mechanics Research Communications* 56:115–22.
- B.W. Rosen. Mechanics of Composite Strengthening in Fiber Composite. *Materials American Society for Metals, Metals Park, Ohio*, 1965.
- E.T. Camponeschi. 1991. Lamina waviness levels in thick composites and Its Effect on Their Compression Strength. *Composites, Design, Manufacture, and Applications*. pp.30E1-30E13
- C.R. Schultheisz, A.M. Waas. Compressive failure of composites part I: testing and micromechanical theories. *Progress in Aerospace Sciences* 1996; 32:1_42.
- L.B. Greszczuk. 1975. Microbuckling Failure of Circular Fiber-Reinforced Composites. *AIAA*. 13(10):1311–18.
- J. R. Yeh, J. L. Teply and Alcoa Laboratories. 1988. Compressive Response of Kevlar / Epoxy Composites. *Journal of Composite Materials*. 245–57.
- K. H. Lo and E. S. Chim. 1992. Compressive Strength of Unidirectional Composites. *J Reinforced Plastics Composites*. 11: 838–96.

- B. Budiansky. Micromechanics. *Computers and Structures*. 1983; 16:3_12.
- A.S. Argon. Fracture of Composites. *Treatise on Materials Science and Technology*. 1972; 1:79_114.
- W.S. Slaughter, N.A. Fleck. Micro buckling of fiber composites with random initial fiber waviness. *J Mech Phys Solids* 1994; 42:1743-66.
- W.S. Slaughter, N.A. Fleck, B. Budiansky. Compressive failure of fiber composites: the roles of multi-axial loading and creep. *J Eng. Mater. Technol.* 1993; 115:308_13.
- N. K. Naik and Rajesh S. Kumar. 1999. Compressive Strength of Unidirectional Composites : Evaluation and Comparison of Prediction Models. *Composite Structures*. 46:299–308.
- Kenneth L.Reifsnider. 1993. Modeling of Composite Compressive Strength. *Journal of Composite Materials*. 27(6):572–88.
- D.C. Lagoudas, I. Tadjbakhsh, N. Fares. A new approach to micro buckling of fibrous composites. *J Appl Mech*. 1991; 58:473_79.
- Ahmed M. Saleh.1993. Compressive Failure due to Kinking of Fibrous Composites. *Journal of Composite Materials*. 27(1):83–106.
- Brian D. Garland, Irene J. Beyerlein and Linda S. Schadler. 2001. The Development of Compression Damage Zones in Fibrous Composites. *Composite Science and Technology*. 61:2461–80.